Developing New Laser-based Instruments to Characterise Optical Properties of Aerosol Particles

Seraphine Catherine Arthur-Hastie

PhD

University of York

Department of Chemistry

September 2024

Abstract

This thesis describes the development and testing of a novel Multi-angle Particle Sizer (MPS) consisting of multiple high sensitivity sensors collecting scattered 445 nm laser light within different large angle ranges, enabling more information to be collected from each aerosol particle, compared to standard optical particle sizer (OPS) instruments. The MPS has been designed to support multiple detectors without sacrificing a low detection limit, along with maintaining a robust, compact and modular design. This report details the full design and testing processes of the instrument, from the earliest conceptual stages to laboratory-based particle analysis. To test the capabilities of the MPS, nebulised polystyrene latex (PSL) spheres of different diameters (200-3000 nm) and colours were analysed and their scattering data compared to instrument output simulations. These simulations used Mie theory to calculate the relative scattering expected to be intercepted by each PMT, and thus predict the instrument's output based on particle parameters. This is a common operating principle of OPS but leaves them vulnerable to misinterpretations caused by unexpected particle properties (e.g. non-spherical), but the more nuanced data collected by the MPS reduces this vulnerability by giving more information to compare with theoretical simulations. Using three scattering intensities results in signal pattern fingerprints for each particle class, allowing for verification versus theoretical data and superior differentiation of the components of mixed particle samples. The MPS was determined to have high dynamic signal range and to be capable of real-time data collection for fast-flowing aerosols, although its minimum resolution could not be definitively verified. Integration with an optical tweezers instrument was also performed, by modifying central structural components without changing the optical array formation (laser, lenses and PMTs). This demonstrates the versatility of the instrument to be altered for use in different contexts to explore different avenues of aerosol analysis.

Declaration

I declare that this thesis is a presentation of original work and I am the sole author. This work has not previously been presented for a degree or other qualification at this University or elsewhere. All sources are acknowledged as references.

Acknowledgements

This project could not have been completed without the support of a great many people who deserve recognition. Katherine Manfred, my original supervisor and to whom the original idea for the MPS owes its existence, your expertise, dedication and enthusiasm have been of great help and inspiration throughout. Thank you for continuing to provide support me long after your obligation to do so.

Pete Edwards, for stepping up to get me through the final year of the project, I am immensely grateful. David Carslaw, your advice and kindness did not go unnoticed, and I am only sorry we did not work together more. Andy Ward, I found the work with the optical tweezers incredibly enjoyable and informative, it's just a shame I only had two weeks of lab time. The unsung heroes of the Wolfson Atmospheric Chemistry Laboratory; particularly Jenny, Martin and Chris, without whom my time at WACL would not have been so straightforward. Mark, Stuart M and Stuart Y deserve full recognition for making sure the CAD and electrical aspects of the project were not a complete shambles, so thank you for answering my endless questions. My friends and fellow students; Maggie, Loren, Lucy, Charlotte, Athina, Jake, Sam and many more, thank you for enduring PhD life with me. Katya, for your invaluable advice and friendship, I thank you, and I hope you take the time to be selfish for once. The NERC PANORAMA DTP, for both making the project possible at all, and getting me through to the end.

And finally, to my wonderful wife, there are not enough pages in this thesis to fully express how valuable your endless and unparalleled support has been. You celebrated me, endured me, and got me through the darkest times. You are my rock, my advocate, my cheerleader, my partner in crime, and the love of my life. Without you, absolutely none of this would have been possible.

Contents

Chapter 1

Theoretical Background

1.1 The Impact of Aerosols

Aerosols are everywhere, their presence in Earth's atmosphere has profound effects on global climate and human health.[1–5] In order for these effects to be understood, analysis of their abundance, emission sources and physical and chemical processes is vitally important. The pursuit of this goal has led to the development of a vast array of analytical instrumentation and theoretical modelling. This forms a well-established and constantly evolving area of scientific advancement, but still there are significant uncertainties and limitations in what is possible.

1.1.1 Introduction to Aerosols

An aerosol is a suspension of small solid or liquid drops in a gas medium, although often the word aerosol is used to refer simply to the particulates themselves. The limits of what is considered an aerosol particle are broad, including particles with sizes covering six orders of

magnitude; from 1 nm to 100 µm.[1,6] Within this range, particles are often further classified into the ultrafine, fine and coarse ranges. Ultrafine particles have diameters between 1 and 100 nm, and include polyaromatic hydrocarbons (PAH), sulphates and smaller soot molecules.[1,2,7,8] Fine particulate matter is 0.1 to 2.5 µm in diameter and is often referred to as $PM_{2.5}$. It encompasses, along others, varieties of mineral dust and bio-particles.[1,2] Within the coarse mode, the classification of PM_{10} (particulates with a diameter between 2.5 and 10 µm) is often used when discussing air quality and PM analysis. The terms $PM_{2.5}$ and PM_{10} are most often used when considering aerosols as atmospheric pollutants, such as when their concentrations, emission sources and harmful effects are being evaluated and regulated. Particles larger than 100 µm do not exist in the atmosphere for long because they are lost via sedimentation much faster due to their increased mass, and thus not typically considered aerosols.[9]

The effects of an aerosol derive from its properties, including shape, size and composition.[10] Therefore, to gain insight into a specific aerosol type's effects on the atmosphere and human respiratory health, it is important to accurately determine its properties.[9] An aerosol's physical properties are determined foremost by its emission source, so having a full understanding of the broad array of global emission sources is an important factor in understanding the field of aerosol analysis.

1.1.2 Aerosol Emissions

Aerosol is an extraordinarily broad category of particle, but it can be divided into subcategories, based on the emission source. These sources are either primary or secondary: Primary aerosol particles enter the atmosphere directly, while secondary aerosols are created via

chemical mechanisms occurring in the atmosphere from precursor components.[11] Primary aerosol particles are emitted from a large variety of natural and anthropogenic sources, including wildfires, volcanic activity, sea spray, fossil fuel combustion, transportation emissions and industrial processes.[1,7,8] Secondary aerosols include sulfates formed by SO_2, released from volcanic activity and industrial processes, as well and nitrates formed by precursor species ammonia and nitric acid.[12] These particles are therefore enormously varied in terms of composition (organic salts, soot, dust, bio-particles, etc.) as well as in size and shape.

The relative abundance of different aerosol types within the total aerosol population is incredibly varied, changing dramatically based on a number of factors including location, degree of urban development, the season and even time of day. A 2010 study by Yin et al. reported the composition of the aerosol population at a Birmingham, UK urban background site, wherein secondary (both organic and inorganic) aerosols made up 58 % of all aerosols, with the remaining primary aerosols originating largely from traffic (exhaust and non-exhaust) (13 %), sea salt (10 %) and so-called off-road/smoking engines such as a lawnmowers (10 %).[13]

Aerosols have a short lifespan in the atmosphere - days or weeks instead of years.[14] They also exist heterogeneously in the atmosphere, often remaining comparatively local to their emission sources. These factors result in aerosol concentrations and compositions that vary significantly based on location, complicating overall quantitative measurement estimates of their overall effects.[15]

Natural Emission Sources

Wind over the ocean causes disturbance to the water's surface which in turn causes significant quantities of salt water droplets to become suspended in the air. The water in these droplets evaporates leaving a solid salt particles suspended as aerosols. Predictably, sea salt aerosol concentration lowers rapidly further inland. Wind also disturbs soil and drags mineral soil aerosol into the air. Forest fires produce large concentrations of combustion products such as black carbon (BC) and brown carbon (BrC). BC is also called elemental or graphitic carbon, or simply soot, and is notable for the broad range of light wavelengths it absorbs; well beyond the visible spectrum, into both the infrared (IR) and ultraviolet (UV) ranges.[16] Brown carbon is a related but distinct category of carbonaceous PM, produced primarily through biomass burning, its absorptivity increases significantly from the visible to the UV range. These emissions are seasonal, unpredictable and occur in rapid bursts rather than gradually as with many of these other sources.

Pollen and spores are examples of biological organic aerosols that are also seasonal, but more predicable in their expected emission patterns. Volcanoes kick vast quantities of ash and chemicals (HCl, SO_2, H_2S) into the atmosphere during eruptions - another largely unpredictable source. This additionally goes on to be a source of secondary aerosols as these chemicals contribute to the production of organic sulphate aerosols.

Anthropogenic Emission Sources

Since humanity's industrialisation, anthropogenic sources have become extremely prevalent, varied and of increasing concern for both human health as well as the state of the global environment. Anthropogenic aerosols make up between 10 and 20 % of total global atmospheric

aerosol emissions, so are of significant concern.[17] They are also, intuitively, more often emitted in close proximity to human activity, so present a more immediate hazard to human health in these localised areas. These processes are also avoidable, at least in principle, so are justifiably often the focus in discussions of aerosol emissions. Combustion products from both vehicles and energy generation, industrial processes and agricultural activity make up the bulk of anthropogenic emission sources. As with forest fires, anthropogenic combustion activity produces both BC and BrC particulates, as well as PAHs and volatile organic carbons (VOCs), all of which are worthy of note due to their various atmospheric and respiratory effects. These respiratory effects include cardiovascular diseases and the aggravation of existing allergies.[18] VOCs, as well as other non-aerosol emissions such as SO_2 and H_2S are responsible for the formation of secondary organic aerosol (SOA) such as sulphate molecules.[15,19] Aerosols are also produced domestically, from a range of human activity such as cooking, using household cleaning products, aerosolised toiletries and cosmetics.

Non-Exhaust Aerosol Emissions from Traffic

Non-exhaust emissions make up a significant total of total traffic emissions, and are composed mainly of brake- and tire-wear, road-wear and road dust re-suspension.[18,20] A study of traffic emissions in northern and central Europe found that non-exhaust aerosols accounted for a significant minority of total $PM_{2.5}$ emissions and even exceeded exhaust emissions for PM_{10} (50-85 % non-exhaust PM_{10}).[19] Contributions of each of these can vary with season and region, for example in Nordic regions where strong seasonal variation adds factors such as anti-slip measures (e.g. grit/salt) and studded/winter tires.[21] Non-exhaust emissions can also be exacerbated by economic factors, since in less affluent countries vehicle components as well as road surface quality are likely reduced, increasing degradation and therefore

increasing emissions.[19]

Tire-wear particles show a significant degree of variability in terms of size, shape, and composition. They exist as both $PM_{2.5}$ and PM_{10}, and are found to have a variety of round, elongated or irregular shapes.[22,23] Brake-wear particles have been found to be composed largely of fine and ultrafine particles.[8,23,24] They also show shape-variation, although they do not exhibit the same elongated/prolate shape as some tire-wear particles, but do appear to be oblate/disc-like in shape.[24]

Although non-exhaust traffic emissions make up a significant proportion of total traffic emissions, their effect is still poorly understood in comparison to exhaust emissions. This can possibly be attributed to the variety of sources for these emissions (tire-wear, brake-wear, road-dust resuspension), the external factors which alter these emissions, and the irregular properties which make measurements and estimations less reliable. This is set to become an increasingly important issue since much of the focus in reducing traffic emissions is focused on tailpipe/exhaust emissions.

Policies and innovations like ceasing the addition of lead to petrol, the move away from diesel for personal vehicles, catalytic converters, low emission zones, a focus on fuel efficiency, and even the move to encourage widespread adoption of electric vehicles do not address non-exhaust emissions. Non-exhaust emissions will indirectly become a bigger proportion of total traffic emissions as exhaust emissions are reduced. The increased prevalence of electric vehicles will even increase non-exhaust emissions, since the increased weight of electric

vehicles compared to traditional combustion engine vehicles of the same size will increase road dust resuspension and cause increased brake-wear.

1.1.3 Atmospheric Effects of Aerosols

The effects of aerosols on the atmosphere and climate are diverse and powerful, ranging from providing sites for heterogeneous chemical reactions and facilitating acid rain to visibility reduction and radiative forcing.[1,2,4] This means that discussions of climate are incomplete without including the direct and indirect effects of aerosols.

The diversity of atmospheric aerosols means that their different atmospheric effects are also varied. Radiative forcing refers to the effect atmospheric particles (gas and aerosol) have upon incoming solar radiation upon contact, and the resulting change on the atmosphere's overall temperature. This interaction is composed of some combination of scattering and absorption, and can be represented by the particle's single scattering albedo (SSA). A high SSA (SSA $\rightarrow$ 1) means this interaction is mostly scattering, thus the particle contributes to negative radiative forcing, resulting in lower temperatures. Conversely a low SSA (SSA $\rightarrow$ 0) means that radiation absorption is the dominant interaction, resulting in positive radiative forcing and therefore a heating effect.

Aerosols differ from other pollutants such as greenhouse gases like CO_2 and methane in that their net forcing is negative. This is both in terms of direct radiative forcing as well as indirectly through facilitating cloud formation. The primary outlier of this trend of negative radiative forcing is BC, which predictably has a major absorbing component and therefore contributes to significant atmospheric heating (SSA = approx. 0.38).[14,25] Aerosols affect

cloud formation through acting as cloud condensation nuclei (CCN) - a seed particle which allows condensation of water from a supersaturated environment - as well as affecting overall cloud distribution and brightness. This alters the effect these clouds have on the atmosphere, including overall temperature as well as rainfall.[25]

Anthropogenic aerosols also contribute to poor visibility, especially in urban areas since these will often have heavy traffic and local industrial emission sources.[15]

1.1.4 Health Effects of Aerosols

The effects of aerosols on health are just as significant as those on the atmosphere, and potentially more important to the individual. Higher aerosol concentrations are found in dense urban population zones, owing to increased anthropogenic emission sources (e.g. traffic) in these regions.[4,26] Many airborne particles are hazardous to human health, owing to their toxicity or carcinogenic properties.[2,27] Exposure to hazardous aerosols primarily takes the form of inhalation, where particulates enter the respiratory system. Aerosols that are hazardous via skin contact are far less common. Depth of penetration into the lungs is often proportional to the harm caused, and inversely proportional to particle size, making fine and ultrafine particles particularly hazardous.[26] Correlations have been found between the presence of $PM_{2.5}$ and serious cardiovascular and respiratory diseases as well as inflammation and cell damage.[4,28]

Atmospheric particulates and other pollutants are becoming an ever-greater contributor to global deaths each year. In 2011, the World Health Organization (WHO) attributed the cause of $\sim$ 2 million yearly deaths to PM exposure.[26] Only 2 years later, $PM_{2.5}$ was estimated

to be the cause of 2.9 million deaths.[29] More contemporary estimates place annual mortality at as much as 8.43 million.[30] The 2021 WHO global air quality guidelines publication states "...more than 90 % of the global population in 2019 lived in areas where concentrations exceeded the 2005 WHO air quality guideline of 10 $\mu g/m^3$".[31]

Since aerosol concentration is often highly localised around the emission sources, the acute effects of particular aerosols may only be evidenced on individuals living in close proximity to specific emission sources, such as a factories, airports and fossil fuel power stations.[32,33]

One of the most significant aerosol-induced health impacts on humans comes in the form of oxidative stress, defined by Pizzino et. al (2017) as "a phenomenon caused by an imbalance between production and accumulation of reactive oxygen species (ROS) in cells and tissues and the ability of a biological system to detoxify these reactive products".[34] The stress caused by PM has a multitude of effects on the body, including DNA damage (which can lead to cancer), cardiovascular, neurological and respiratory diseases, rheumatoid arthritis, renal system disruption and even a delay to puberty and sexual maturation.[15,19,34]

It is clear that the combined atmospheric and health impacts of atmospheric aerosol make improving the understanding of these airborne particles vitally important.

1.2 Physical Properties of Aerosols

Just as the sources of aerosol particles are hugely varied, so are their physical properties. These physical properties, arising from their composition and formation, go on to dictate

their effects on both the atmosphere and human health. They are thus vital to understand in order to predict and manage their effects, and to perform accurate identification.

The physical properties most important for characterising aerosol particles include size (more precisely diameter, at least for spherical particles), shape, homogeneity and optical behaviour. Size is often treated as chief among these; PM are characterised by size (ultrafine, fine, coarse), and indeed size strongly affects the magnitude and nature of the impact of the aerosol. It is for this reason that sizing aerosol particles is the purpose of a vast range of commercial analytical instruments. In spite of this, size determination as well as determining abundance of size-classifications in an environment is often based either on assuming other physical properties, or using mass measurements.

A common assumption made when simulating or analysing aerosol particles is that they are uniform spheres. While an undoubtedly useful assumption since it simplifies calculations and predicting interactions massively, many of these particles are far from spherical or homogeneous. Common non-spherical morphologies include fractals and spheroids (discs and rods). Other factors may alter the behaviour of spherical particles, such as non-uniform composition. Particles may have a core and a shell, both made of different material, which affects light interactions. This can also be caused by incomplete permeation of a dye or other liquid into a particle, a phenomenon which becomes more common with increasing diameter.

1.3 Analysing Aerosols

Due to the impact, variety and ubiquitous nature of aerosols in virtually all environments, their detection, quantification and characterisation is an important area of instrumentation.

It is important to understand ambient aerosol concentrations within different regions, to this end organisations such as the WHO maintain a database of global $PM_{2.5}$ and PM_{10} concentrations. As an example of the scale of the issue according to the WHO 2021 Global Air Quality Guidelines, over 90 % of people live in areas where $PM_{2.5}$ concentrations were above the WHO's guideline concentration of 10 μgm^{-3}.[31] From the perspective of aerosol analysis, it is notable that this and most PM concentration guideline figures are based on mass concentration, rather than number concentration. The classifications of $PM_{2.5}$ and PM_{10} are also determined via mass measurements. Mass concentration is used because the techniques have been generally more available.

This is sub-optimal because larger PM will dominate these measurements disproportionately from their actual abundance, and the physical properties such as size are (as discussed above) vitally important for a full understanding of their impact, atmospheric presence and the risks of exposure. This makes the development of new and improved techniques, which can accurately size particles, of key interest.

1.3.1 Detection and Quantification

The most basic techniques for aerosol analysis seek simply to detect the presence of aerosols and calculate their concentration. Aerosol concentration methods include gravimetric methods of determining mass concentration by collecting particles on a filter (e.g impactors) and oscillatory microbalance methods which measure the change in resonance frequency.[35] A common type of impactor known as a cascade impactor separates particles based on their inertia (and therefore size), by forcing a flow of aerosols through multiple, progressively finer slits or nozzles.[2] These techniques are referred to offline technique, since samples are

collected and analysed later - they cannot provide live/real-time data. Condensation particle counters (CPCs) can provide real-time number concentration data from a flowing air sample. They facilitate condensation of a liquid such as butane onto particles to increase their size and make detection of otherwise too-small particles reliable. CPCs represent an online analytical technique, since they can provide live and continuously updating information from the air being sampled.

1.3.2 Microscopy

Transmission electron microscopy (TEM) can be used to image individual deposited particles and determine their size and shape. This method can be very precise, but due to the long duration between collection of a sample and the observation, it can offer limited insight into aerosols that may be volatile or otherwise change over a short time span.

1.3.3 Optical

Optical methods differ from microscopic methods since they can be performed in situ and able to provide real-time measurements. These methods measure the light extinction, scattering or absorbing properties of aerosol particles. Optical particle counters (OPC) count particles by detecting the scattering of a light source they induce. Cavity ringdown ringdown spectrometers (CRDS) measure the extinction of light caused by repeated passes of a laser through a sample medium.[36,37] Photoacoustic spectroscopy (PAS) instruments excite particles with radiation and acoustically measure their vibration and hence determine their absorption.[38]

Size-distribution methods are a broad category of methods which measure physical, optical,

aerodynamic diameter or mobility diameter to determine size.[35] There is also overlap in instrumentation with concentration measurements. Optical particle sizers (OPS) detected light scattered by an individual particle, and use calibration with a test particle and property-specific theoretical scattering estimates to determine the size of a particle based off the magnitude of scattering.[39–42]

OPS instruments can provide accurate, real-time, in situ, high time- and size-resolution measurements of aerosol samples in the fine and coarse ranges.[43] It is a robust and well-established facet of PM size and concentration analysis and sees frequent use in aerosol studies with many different commercial options available. However, this performance is based on assumptions about the particles sampled, particularly refractive index (RI). In an ideal case this is not an issue, but for sampling mixed and unknown samples, particularly particles without well-established refractive indices in the literature, OPS can be prone to inaccuracy.

1.3.4 Measurement Locations

Since aerosols are virtually ubiquitous, aerosol analysis takes place in many forms and locations. This ranges from lab-based analysis in controlled conditions, to stationary sampling sizes in areas of interest, to mobile particulate collection using an instrument installed in a vehicle, such as a van or a ship. Remote sensing is a bulk phase analysis technique via long range detection of scattered radiation - usually using a satellite. Another technique is to use measurement networks; a series of instruments collecting live data simultaneously, distributed over a large ares, in order to gain better insight as to localised trends and aerosol spread.[44]

These different sampling techniques will require different considerations when designing an instrument, as properties such as size, weight, power consumption, data storage may be limited based on desired operational environment.

1.4 Aerosol and Light Interactions - Mie theory

Key to characterising aerosols is understanding how electromagnetic waves interact with small particles. When an incident beam intercepts a particle some of the radiation is converted to thermal energy on the particle's surface (absorption) and some is redirected in directions that differ from the incident direction (scattering). This scattering can either be elastic or inelastic; the same or different wavelength as the incident beam respectively. The summation of these two effects is known as extinction.[2] Since both the scattering and absorption are dependent on the properties (such as diameter and refractive index) of the particle, analysing the scattering caused by a particle under examination can shed light on its properties. This principle is the foundation upon which many analytical instruments for characterising aerosols are built. Aerosols can have a vast variety of shapes, making exact scattering and absorbing behaviour difficult to predict. To overcome this, assumptions can be made regarding morphology to simplify calculations while still achieving good predictions of scattering and absorption. Mie (Mie-Debye-Lorenz) theory assumes a particle is a uniform sphere, allowing its morphology to be defined by a singular value; its diameter (D_p). Since the scattering and absorbing by a particle is also dependant on the wavelength of the incident beam (λ), the relationship between the diameter and wavelength is expressed using a size

parameter (α), as shown in equation (1.1).

$$\alpha = \frac{\pi D_p}{\lambda} \tag{1.1}$$

Another determinant parameter is the complex refractive index (often represented as N, CRI, or simply RI) of the particle. RI as a physical property of a material describes its effect on the redirection of light when moving though, refracting off, being absorbed by or otherwise interacting with a material. Equation (1.2) shows that N is comprised of both a real component n and imaginary component k, where $i = \sqrt{-1}$.

$$N = n + ik \tag{1.2}$$

A particle exhibits absorption at a particular wavelength when k has a non-zero value. RI is wavelength-dependant, rather than being a static value for every wavelength. The RI of the particle (N) is also commonly normalised by the RI of the surrounding medium (N_0), N/N_0, to give m. However since N_0 is essentially 1 + 0i in air, N and m are equivalent.

Mie theory is able to predict the scattering and absorption of a spherical particle using only m and α as inputs. It can also be used to produce a scattering phase function - an angular distribution of scattered light intensity relative to the incident beam direction. The approximate form of a particle's phase function (i.e. the relationship between forward and back-scattering) is dependant on the ratio of the particle diameter to the wavelength, and so has a direct relationship with the size parameter α. Scattering behaviour can be broken down into three broad categories based on the value of α, as follows: Known as Rayleigh scattering when $\alpha << 1$, geometric/non-selective scattering when $\alpha >> 1$ and Mie scattering when

the particle diameter is approximately the same as the wavelength ($\alpha \approx 1$). For Rayleigh scattering, the phase function is symmetrical in the forwards ($0^\circ \leq \theta \leq 90^\circ$) and backwards ($90^\circ \leq \theta \leq 180^\circ$) directions. In contrast, for geometric scattering forward-scattering is heavily dominant, and back-scattering is greatly diminished. Mie scattering can be seen as the transition period between these two configurations, where forward-scattering is still greater than back-scattering, but the disparity is diminished.

Scattering is also affected by light polarisation, with the scattering of parallel-polarised light differing significantly from that of perpendicular-polarised (both relative to the plane of detection) light. While these can be separately determined, all computations presented in this chapter assume unpolarised light.

Since Mie theory can predict angular scattering of a spherical particle given only its diameter (and thus size parameter for a given wavelength) and RI, it is possible to produce a simulated phase function for a particle with those properties. One such method for doing this was published in 1983.[45] Using a size parameter and complex refractive index as inputs, the Mie calculation is able to predict the scattering intensity at any angle or angle range between 0° and 180° (or -180°; the arcs are equivalent), allowing creation of a predicted phase function. The code is also capable of simulating a coated particle, with a spherical, central core and shell of a defined, uniform thickness, with both parts having potentially different RIs. When electromagnetic radiation is scattered by a particle, the energy scattered ($\widetilde{F}_{scat}$) is proportional to the incident intensity (F_0, units Wm^{-2}),

$$\widetilde{F}_{scat} = C_{scat} F_0 \tag{1.3}$$

where C_{scat} (m^2) is the single-particle scattering cross section or effective scattering cross section. An equivalent relationship exists between the energy absorbed by a particle and its effective absorbing cross section:

$$\widetilde{F}_{abs} = C_{abs} F_0 \tag{1.4}$$

The relationship between a particle's scattering or absorbing cross section and its physical, cross-sectional area (C_{phys}) is expressed as the ratio C_{scat}/C_{phys} (or C_{abs}/C_{phys}), known as its scattering or absorbing efficiency (Q_{scat} or Q_{abs}) respectively. The extinction efficiency (Q_{ext}) can be derived as shown:

$$Q_{ext} = Q_{scat} + Q_{abs} \tag{1.5}$$

The Mie code can also derive these dimensionless efficiencies for a spherical particle given α and m. This can be useful for predicting the optical behaviour of particles.

1.4.1 The History and Legacy of Mie Theory

Mie scattering as a theory to model the scattering of light by a spherical particle, based on its size parameter and complex refractive index (CRI), has existed for over a century.[11] The ease with which the angular distribution of scattered light can be calculated has resulted in Mie theory becoming near-ubiquitous when performing optical measurements of particles with sizes in the Mie regime. As explored above, Mie theory is the underpinning theory of OPS instruments, allowing scattering signals to yield particle size estimations. OPS instruments use Mie theory to generate predicted scattering intensity values (based on assumed properties such as sphericity and CRI), and use that data along with the experimentally determined

distribution of scattering values to return a distribution of particle size from a sample of particles.

1.4.2 Mie theory simulations

The use of Mie theory is incredibly pervasive in the fields of aerosol and atmospheric conditions. In spite of its assumptions in regards to particle sphericity, the results obtained with Mie theory are often sufficiently close to experimental data to be used as the theoretical basis for optical scattering instrument calibration. Mie theory is capable of producing more than just a phase function; scattering (as well as absorption and extinction) efficiencies can also be calculated from a particle's properties. These efficiencies can be used to determine properties such as scattering (absorption and extinction) coefficients, which indicate their effect on light when in the bulk phase - such as in the atmosphere.

In order to assess the effectiveness of the the Mie theory instrument simulations, the model was assessed for accuracy using existing publicly available data from a 2019 flight campaign. The model was used to calculate scattering coefficients at different points and compare the results with the scattering coefficients determined using other onboard instruments.

The Fire Influence on Regional to Global Environment and Air Quality (FIREX-AQ) campaign was a 2019 US inter-agency initiative conducted by NASA (National Aeronautics and Space Administration) and NOAA (National Oceanic and Atmospheric Administration).[46,47] Its goal was to analyse and evaluate the effect of wildfire emissions on tropospheric composition and chemistry using satellite, ground and air-based data. One of the research aircraft used was NASA's DC-8, which housed a multitude of instruments for data collection during

flight.[48] The instrument array of focus here is the AOP (in situ measurements of Aerosol Optical Properties), which provides rapid aerosol extinction and absorption measurements at different wavelengths (405, 532 and 664 nm). The AOP comprises two instruments; a cavity ringdown spectrometer (CRDS), a photoacoustic absorption spectrometer (PAS).

The data collected for FIREX-AQ are publicly available. Due to the simultaneous collection of both extinction and absorption coefficients from the bulk as well as single particle aerosol size distribution data, this provides an appropriate base from which to evaluate the use of the Mie code to calculate aerosol scattering and extinction coefficients.

The 8-channel CRDS used as part of the AOP was designed in 2011 for use aboard an aircraft.[37] The CRDS measures optical extinction and its dependence on relative humidity. It was originally set up to do this at 405, 532 and 662 (now 664 for the AOP) nm, since aerosol properties like single scattering albedo (SSA) (ω) - the ratio of scattering efficiency to total extinction efficiency, (Q_{scat}/Q_{ext}) - are wavelength-dependant.[2] The key components of this CRDS are as follows: An optical cavity containing two highly reflective concave mirrors, a pulsed laser source which can inject a laser pulse into the cavity, and a photodetector (a photomultiplier tube in this case).[36] The intensity of this pulse decreases exponentially over time once the laser is turned off. This is due not only to transmission losses though the mirrors, but also scattering and/or absorption interactions with the medium within the cavity, if present. The decay of the light intensity is measured using the photodetector, and is characterised by ringdown time (τ). This is the timescale for the intensity to decrease to $\frac{1}{e}$ of its original or previous value; known as its $\frac{1}{e}$ folding time. To isolate the effect of the air sample on the decay rate, ringdown time is recorded both with the sample air present (τ) and

without (τ_0). Operated with repetition rates of 1 kHz, the lasers allows the PMTs to register 1000 decay traces per second. These traces are averaged over one second.

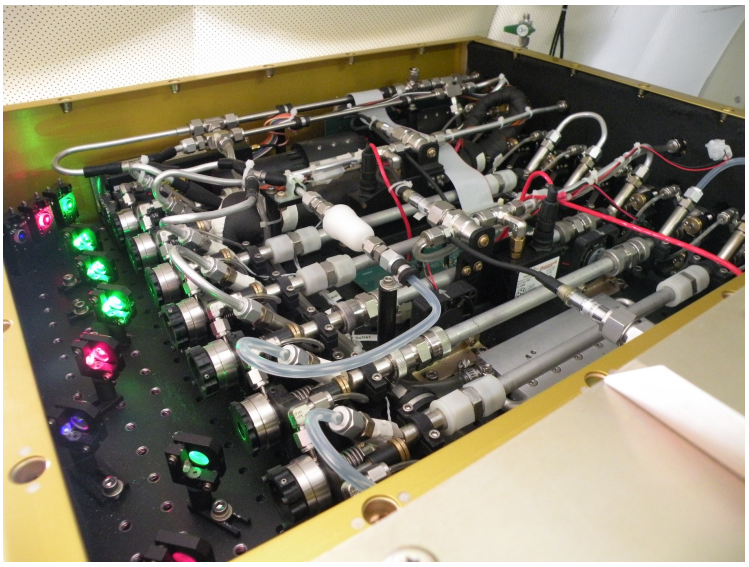

Figure 1.1: Photograph of CRDS instrument.[49] The 405, 532 and 664 nm laser optics are visible in blue, blue and red respectively. The 8 cavities run along the instrument, the sample inlets can be seen at either end of the cavities, aligned at 45° angles

Since rate of decay is dependant of the distance travelled, the length of chamber is of vital importance. The 8-channel CRDS described here has a mirror to mirror distance of 48 cm, however the air sample inlet is only 39.7 cm from the outlet. This can be seen in the picture of the CRDS in figure 1.1. For this reason extinction coefficient calculated from τ is adjusted using a length correction factor R_L of 1.21; the ratio of the cavity length to the length within the cavity containing the sample. This is seen in equation (1.6) (with c being the speed of light), which shows the method by which the extinction coefficient (μ_{ext}) is calculated. The units for μ_{ext} are inverse length.

Although the beam will dip in intensity during a single pass through the cavity, it won't be by a detectable margin. Extinction from the medium is only detectable over a long distance, hence why μ_{ext} is reported in Mm^{-1}. The concave mirrors cause the beam pulse to continue

to pass back and forth through the chamber after the laser has turned off, allowing the measurement of reduction in intensity over a much longer effective distance.

$$\mu_{\text{ext}} = \frac{R_L}{c}\left(\frac{1}{\tau} - \frac{1}{\tau_0}\right) \tag{1.6}$$

From the external air intake, the CRDS accepts a flow of 3 litres per minute (LPM) , which is selectively passed through a aerosol filter (to achieve τ_0 measurements, approximately every 300 s) or not, before being dried and split evenly between three channels, which each take a flow of 1 LPM. The first of these is used to collect extinction data at high (95 % and 70 %) humidities. The second channel measures dry aerosol extinction. The third channel is fitted with an aerosol filter ahead of the three cavities, allowing it to serve as the 'gas reference channel'. The relative humidity (RH), temperature and pressure of the air exiting each channel is measured to correct for changing environmental conditions. While the CRDS is able to acquire accurate in situ extinction coefficients of atmospheric aerosols, it is unable to differentiate between the scattering and absorbing components of this extinction. To mitigate this inherit limitation, the CRDS is paired with another instrument.

Built to work in tandem with the CRDS, the PAS analyses atmospheric aerosols alongside the CRDS, but measures bulk phase absorption rather than extinction.[38] The PAS utilises a cavity-system and pulsed lasers, but rather than using a photodetector, it uses a microphone to detect a resonator-amplified pressure wave induced by absorption of energy from the laser by present aerosol. This particular PAS has five acoustic cavities; three for dried air flow with laser wavelengths of 404, 532 and 659 nm, and two for thermo-denuded (TD) air flow at 404 and 532 nm. Since detection is acoustic rather than light-dependant, the

instrument is effectively blind to scattering of the beam.

Some considerations that effect the design and setup of the instrument are as follows: The sensitivity of the instrument is proportional to laser power, however if the energy transferred to the aerosol is too great, it will affect the particles' properties (e.g. evaporation or incandescence). Additionally, cavities were physically isolated to reduce noise.

From the microphone data (corrected for gas phase absorption using both data collected during filter periods as well as gas phase extinction data from the CRDS), the absorption coefficient μ_{ext} for the aerosol is presented at 1 Hz. With both instruments in tandem, particle properties like μ_{scat} and SSA can be calculated from the extinction and absorption.

Both the CRDS and PAS collect no data on the aerosol concentration or aerosol size distribution, merely measurements of the extinction and absorption respectively from the bulk phase. The UHSAS is a commercial instrument (Droplet Measurement Technologies, Longmont, CO, USA) capable of counting aerosol particles in up to 100 user-specified bins, between 0.06 and 1 μm in diameter, with user-specified time resolution.[41,42,50] In this instance, 99 bins were set to be logarithmically spaced between 65.5 and 1372 nm.

The UHSAS uses a high-intensity infrared laser and two photodiodes; an avalanche photodiode (APD) and a PIN photodiode, which detect smaller and larger (within the instrument's detection limits of approximately 0.06 - 1 μm) particles respectively. The photodiodes are positioned on opposite sides of the intersection of the beam and a sheathed sample flow. Scattered light from beam-particle interactions is reflected by two pairs of Mangin mirrors,

which cover solid angles of 33-147°, although the centre of this region (72.5-104.8°) is not sampled due to the shape of the optics. The resulting collection angles are 33-75.2° and104.8-147°.

Data were collected using a UHSAS device. It was fitted with a flow controller to maintain constant volumetric sheath flow, important in aerial use with unsteady air pressure since this could cause a change in velocity through the instrument. Additionally, it was fitted with a 250 °C thermodenuder. For the purpose of aerosol sizing from the collected data, the RI of ammonium sulphate (n = 1.52) is assumed.[51] Scattering intensity is proportional to particle size, so with an assumed RI, the UHSAS can relate an amount of light scattered to a particle size.

Two 1 Hz data sets from the FIREX-AQ campaign are of interest here; optical data from the CRDS and PAS, in which extinction and absorption coefficients μ_{ext} and μ_{abs} are given at 405, 532 and 664 nm, both before and after a thermodenuder (thermodenuded particles only analysed at 405 and 664 nm), and UHSAS data which reports number size distribution of a thermodenuded flow of air particles.[52] Q_{scat} can be calculated for each UHSAS size bin. This can in turn be used, along with the UHSAS distribution data to estimate the total μ_{scat} for the particles every second. This should be in agreement with μ_{scat} values taken from the CRDS and PAS data sets (μ_{scat} can be calculated from μ_{ext} and μ_{abs} in the same fashion as efficiencies in equation (1.5)).

Q_{scat} was calculated for each of the UHSAS' size bins at 405 and 664 nm. To achieve this an input of α for every bin size at 405 and 664 nm was required. For example (in

place of a comprehensive list of every α value at both wavelengths), bin 1 and bin 99 centre diameters are 65.5 and 1372 nm, so (at 405 nm wavelength) α is 0.508 and 10.6 respectively (equation (1.1)). RI is assumed (as with the UHSAS data computations) to be 1.52 + 0i. Presented values for Q_{scat} for each bin are multiplied by the geometric cross section (C_{geom}) calculated from bin diameters to give the effective scattering cross section C_{scat} (equation (1.7)). Multiplying this by the presented density values (N) for each bin and summing them gives scattering coefficient μ_{scat} for each distribution (equation (1.8)).

$$C = QA_{geom} \tag{1.7}$$

$$\mu = CN \tag{1.8}$$

Figure 1.2 shows comparison of the results of this method for calculating μ_{scat} compared to μ_{scat} calculated from subtracting the published PAS-derived μ_{abs} from the CRDS-derived μ_{ext}. It shows general agreement between the values from each method, lending legitimacy to the above-detailed method. However, discrepancy in some areas demonstrates that the method is not perfect. Notably, the assumed RI of 1.52 + 0i was used both for producing the size distribution data from the UHSAS and the calculation of Q_{scat} using the Mie code. A consequence of this is that the code produces a value for Q_{abs} of 0 (expected as no absorption would be taking place when $k = 0$). However, results from the PAS show absorption does take place, even when correcting for the absorption of the air medium. This μ_{abs} from the PAS has been subtracted from μ_{ext} (from the CRDS) to give a value for μ_{scat}. This means that the aerosols are not totally non-absorbing, and the assumed RI does not exactly reflect the true value. A non-zero value for k often increases the calculated value of Q_{scat} (and

thus μ_{scat}), meaning this assumed m may be leading to a consistent under-estimation. This mismatch between the assumed m and the true m being may be due to the air being sampled; fire plumes. Soot present in fire plumes is highly light absorbing, meaning a non-absorbing m is likely not ideal for producing accurate results.

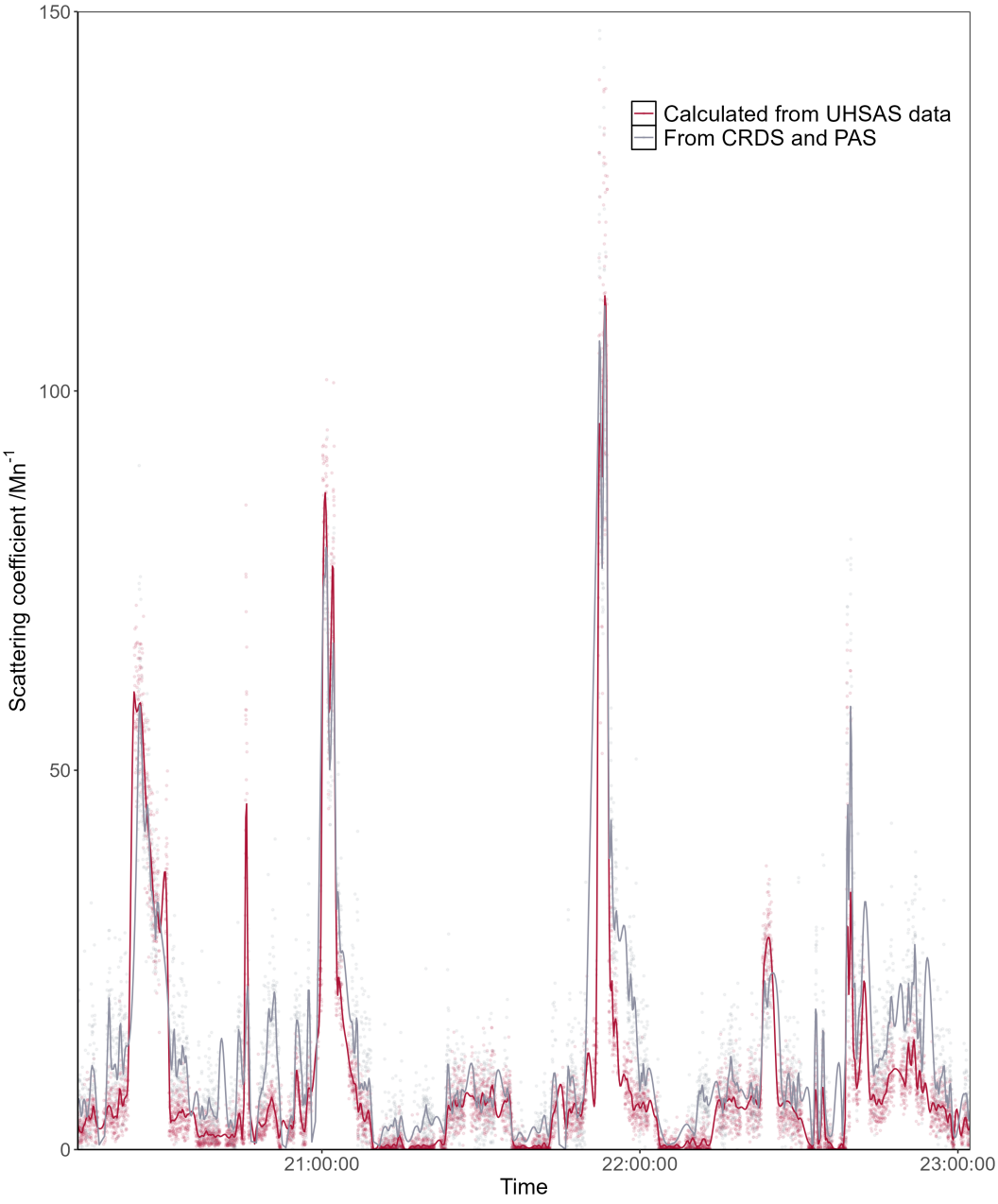

Figure 1.2: Comparison between scattering coefficient calculated from extinction coefficient and absorbing coefficient obtained from CRDS and PAS respectively (grey), and scattering coefficient calculated from UHSAS size distribution (red). Refractive index assumed as 1.52 + 0.0i. Data collected using 405 nm laser, on the 5th September 2019[52]

1.4.3 Limitations

Mie theory provides a robust and proven way of calculating scattering for ideal particles. Unfortunately particulate matter in real-world environments is often far from ideal. BC shows this plainly, due to its light absorbing properties, an OPS' size data being calculated on the assumption of pure scattering ($k = 0$) will not return reliable sizing data when sampling BC. Since this absorption necessarily reduces scattering, an OPS instrument may be prone to underestimating the size of absorbing particles.

BC, in addition to absorbing much of the light it interacts with, does not necessarily form ideal spheres. BC particulates exist as spheres, highly branching fractals, and morphologies between these two extremes.[53] This variation in morphology means that not only will an assumption of uniform sphericity be wrong, but the extent of variation is also unknown, unless the sample is separately collected and analysed (e.g. using a TEM).

BC is not alone in presenting such difficulties for optical measurement techniques, countless other PM found in the atmosphere deviate from the model of an ideal, purely scattering sphere. This includes particles mentioned above; dust from a variety of sources, as well as biological particulates such as pollen and spores.

1.4.4 Non-spherical particles

Mie Theory is comfortably the most widely used theory for modelling light/particle interactions, but other models for non-spherical particles do exist and have been implemented to evaluate the properties which do not conform to Mie theory's necessary shape assumptions.

SMARTIES (T-matrix)

SMARTIES (Spheroids Modelled Accurately with a Robust T-matrix Implementation for Electromagnetic Scattering) is a suite of tools for modelling electromagnetic scattering spheroidal particles using the T-matrix modelling.[54] Similar to the Mie theory code used previously, from a set of particle parameters and an electromagnetic wavelength, angle-dependant scattering can be estimated. Unlike for Mie theory, the particle's aspect ratio (for height and diameter) can be input, allowing for the simulation of prolate (height > diameter) and oblate (height < diameter) spheroids.

A consequence of this is that a sphere (aspect ratio = 1) can be simulated, allowing direct comparison of the output from T-matrix and Mie theory for spheres with the same properties. Figures 1.3 and 1.4 show the potential for an OPS detecting scattering within multiple angle ranges to distinguish between spheroidal $PM_{2.5}$ with different morphologies, by quantifying the discrepancy in the ratio between the observed scattering and the simulated scattering of the spherical morphology.

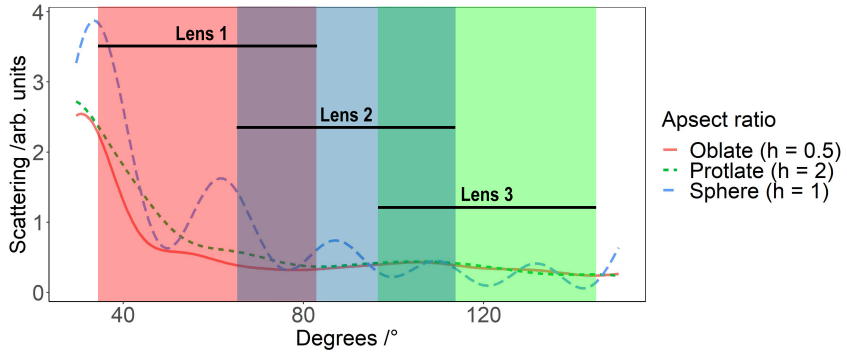

Figure 1.3: Illustration of simulated phase functions produced using the T-matrix algorithm for spheroids with different aspect ratios. Potential angle ranges to be used for project instrument are shown as 'lens' 1-3. Spheroids are volume-equivalent to a 1 μm sphere with a α of 7.06 at λ = 445 nm. Random orientation of particles is assumed

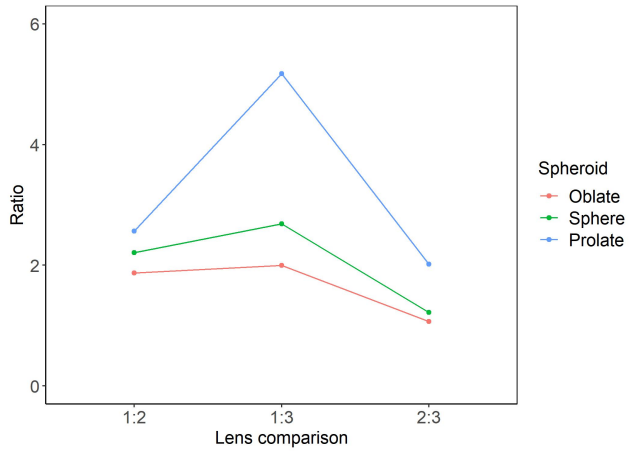

Figure 1.4: Comparison of ratios between captured signals of simulated volume-equivalent-spheroids with different aspect ratios, using phase functions displayed in figure 1.3.

Rayleigh-Debye-Gans Theory

Rayleigh-Debye-Gans (RDG) theory is used to simulate scattering of fractal aggregates. These fractal particles are modelled as an aggregate of monodisperse spheres. In addition to these assumptions, a single RI is also assumed for the whole particle. This is a suitable modeling theory for particles such as soot aggregates, which are well established to form in

this way.[55,56] The geometry of the particle is described by the equation,

$$Np = k_f \left(\frac{R_g}{a} \right)^{D_f} \tag{1.9}$$

wherein N_p is the number of primary particles (monomers) within the aggregate, a is the monomer radius and R_g is the radius of gyration (determined by the mean distance of each primary particle form the centre of mass of the aggregate).[57] Additionally, k_f is the fractal prefactor and D_f is the fractal dimension. k_f can be considered an indication of monomer overlap and D_f increases with increasing branching and packing, so both are needed to determine the compactness morphology of the aggregate.[58] Figure 1.5 shows that, based on

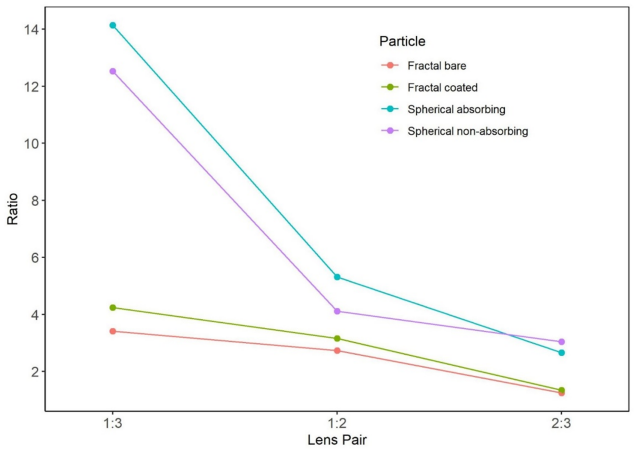

Figure 1.5: Comparison of ratios between lens signals of simulated particles with 300 nm sphere-equivalent mobility diameter.

simulated data, the MPS is capable of distinguishing between spherical and fractal particles of equivalent size. The scattering effects of particle features such as light absorbance and coatings are also visible.

1.5 Contemporary OPS Instruments and Mie Theory Dependence

In the field of single particle PM analysis, instruments that detect a single larger portion of particle-scattered light ('single angle') are used most commonly. These techniques come with distinct advantages such as high sensitivity and a smaller minimum-detectable-particle size due to capturing light over a large angle. However, an inherit limitation of this type of device is that no details of the phase function are retained, and an RI must be assumed in order to calculate particle sizes.[41] This is not an issue when the RI of the analysed particle is well established via experimentation, but for particles with less well known or less consistent RI the uncertainty of any sizing or analysis increases. Increasing angular resolution can alleviate these drawbacks since more information is collected, removing the need to assume as much information.

One method for obtaining scattering data with a higher angular resolution involves moving a photodetector through an angle range.[59,60] This captures a far more comprehensive scattering profile, however this instrumentation has significant drawbacks: The time required to move the detector necessarily precludes analysis of single, moving particles. It is unsuited to analysing polydisperse or mixed samples, since the scattering profile will not be consistent for the time the detector is moving. It also significantly increases the mechanical complexity and weight of the instrument, which otherwise would have very few moving parts, making operation and construction more challenging. These limitations have prevented instruments of this kind from being used commonly to analyse atmospheric aerosol.

Another method for capturing multiple discrete sets of scattering data involves using more than one detector, each positioned to capture a different range of scattering. This method is able to analyse individual particles, but the necessarily-reduced angle range limits instruments' lower detection range, since smaller particles scatter less total light than larger particles.[7] Consequently this principle has been predominantly used for detection of larger aerosol.[61–63] Most of the rare multi-angle particle sizers in recent literature use between two and four photodetectors, which allows for the use of focusing lenses to capture larger angle ranges while still detecting scattering over multiple ranges.[61–65]

Beyond this, being able to analyse different scattering angles simultaneously is useful, since scattering at different angles may be affected by certain particle properties. For example, there is an understanding that low angle scattering (less than approximately 20 °) is largely insensitive to RI, unlike mid-scattering angles which are strongly affected.[62] Detecting scattering at multiple angles also allows for analysis of scattering ratios between different angle ranges and the creation of lookup tables based off simulated data.[64]

1.5.1 Ultra-high Sensitivity Aerosol Spectrometer

The Ultra-high sensitivity aerosol spectrometer (UHSAS) has been described above. Due to its high sensitivity and wide range of detectable particle sizes, the UHSAS is a highly effective and reliable instrument for aerosol sampling, both for ground and aerial measurements.

Although the UHSAS uses multiple detectors, the purpose of this is to expand its detection limits, since both detectors collect data from within the same scattering range.

1.5.2 Portable Optical Particle Spectrometer

The recently developed portable optical particle spectrometer (POPS) is an OPS designed to have minimal weight (600 g), power consumption ($\sim$ 5 W) and physical dimensions (16.51 $\times$ 17.5 $\times$ 7.6 cm) while maintaining good time and size resolution.[39,40] It detects scattering within a 104° angle range using a photomultiplier tube (PMT). The sample flow is sheathed in clean air to maintain laminar flow and keep particles in the centre of the sampling volume. The POPS is also capable of measuring particles as low as 140 nm. It is a small, lightweight, sensitive OPS instrument, well suited to aerial use.

1.5.3 Twin Angle Optical Particle Counter

Eidhammer et al. demonstrated that their twin angle optical particle counter (TAOPC) could be used to estimate the complex RI by using a detector at 40 $^\circ$ and another at 74 $^\circ$.[61] However there were significant uncertainties in these estimated RIs and the small detection angles limited detection to larger aerosol particles (1.5 µm). A successor to the TAOPC, the LOAC (Light Optical Aerosol Counter), was able to characterise smaller particles, though still with significant uncertainty. The LOAC used a low-angle detector (12 $^\circ$) to detect forward scattering, which is less effected by a particle's RI than higher-angle side scattering.[43,62,63]

1.5.4 Single Particle Polar Nephelometer

Attempts have been made to use this same multi-detector setup to analyse smaller particles. For example the single particle polar nephelometer (SPPN) (developed in 2016 by Nakagawa et al.) uses an array of two arcs of 21 silicon photodetectors.[66] This unconventional approach of using so many detectors results in gaining a lot of angle-resolved scattering information from each particle. However, each detector covering a small range and the apertures used to prevent sensor flooding result in a very narrow detection range of 300 to 900 nm. Overall, the instrument demonstrates the potential of using multiple detectors, but its limitations prevent it from broad particle analysis applications.

1.5.5 Fast Exhaust Nephelometer

The fast exhaust nephelometer (FEN) (published by Kheirkhah in 2016) was designed to measure and characterise the soot emissions from a combustion engine, with which it was integrated.[64,67] It uses three biconvex lenses positioned at 45 °, 90 ° and 135 ° relative to the incident beam, and three silicon photodetectors. Each lens covers a 30 ° range. The FEN was designed specifically to analyse fractal soot aggregates, but the use of three photodetectors to capture forward, side, and back scattering, each capturing a larger angle range via use of a dedicated biconvex lens has potential to overcome many of the limitations currently seen in multi-detector OPS instruments.

To achieve this, the novel multi-angle particle sizer (MPS) has been developed.

1.5.6 The Multi-angle Particle Sizer

The MPS has been designed to perform characterisation of $PM_{2.5}$ with non-ideal properties by detecting scattered laser light within multiple different angle ranges. There is a compromise between detection limit and angular resolution, given that large collection angles are required to reliably detect smaller particles. However, using additional detectors and increasing the information collected form each particle, the reliance of standard OPS instruments on Mie theory can be reduced. The following chapters detail the design process behind the MPS, and an evaluation of its analytical capabilities.

Chapter 2

Creating the MPS

The goal in designing the multi-angle particle sizer (MPS) was to create an optical particle sizer capable of detecting three distinct regions of light scattered from a particle. This chapter contains the details of all aspects of the design process; hardware and software. In addition to the final (for the purposes of this project) iteration of the MPS, prototypes and unused designs are included, both for completeness, and to give a full picture of the design process. Functionality testing such as for laser power chamber pressure are also included in this chapter.

2.1 Optical

Since the fundamental principle of the MPS is the scattering and collection of light, the design of the optical components was considered first, with other components including the structural and aerosol components being designed to support their function. A full optical diagram is presented in figure 2.1.

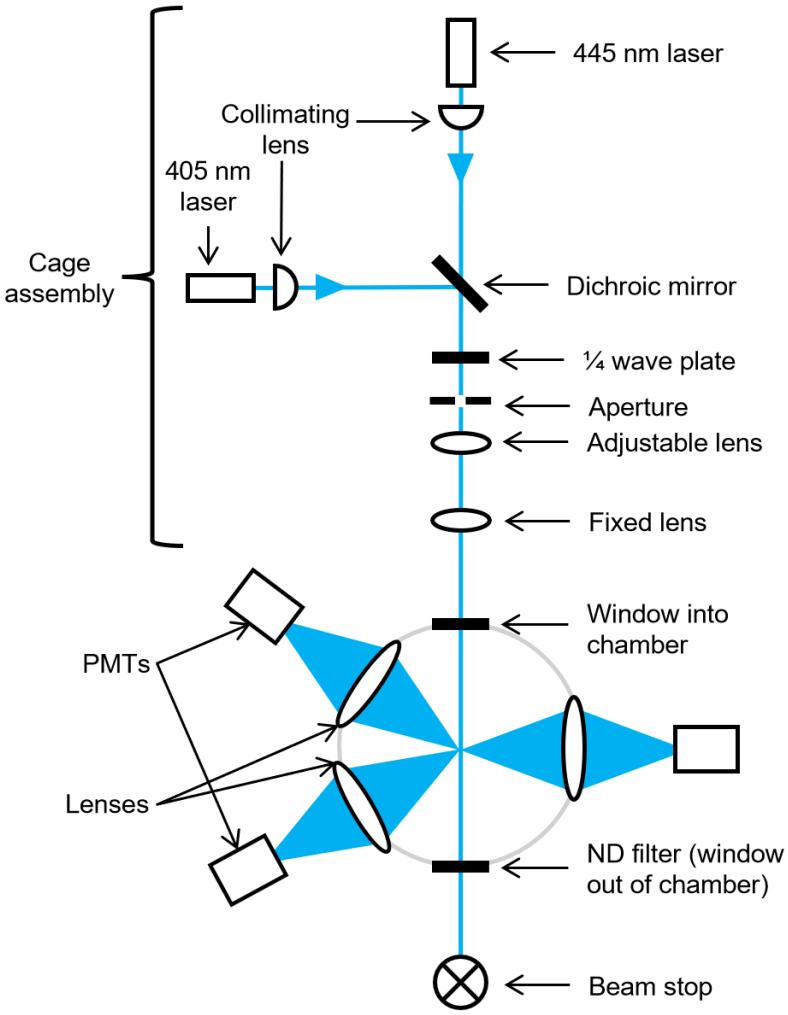

Figure 2.1: Diagram showing the path of the beam into the MPS chamber, where it either exits and terminates in a beam stop, or is scattered and detected by the PMTs. 405 and 445 nm lasers were positioned to allow convenient switching between beams; lasers were not used simultaneously.

2.1.1 Laser

Two lasers were used in the course of instrument development; two continuous wave, linearly polarised, polarisation-maintaining fibre-coupled diode laser (MatchBox, Integrated Optics), with two different wavelengths, 405 and 445 nm. These wavelengths, within the blue range of visible light were chosen since the scattering behaviour is based on the relative sizes of the wavelength and particle size, and 400 nm is sufficiently close to the diameter of most $PM_{2.5}$ particles. 405 nm in particular is a commonly chosen wavelength for optical particle

sizer instruments.[37,39,40,52] This is also beneficial since RI is often wavelength-dependent, so using a standard wavelength of light makes finding RI values in the literature easier.

2.1.2 Beam Collimating Lens

The variable, aspheric collimating lens (Thorlabs) functioned both to either collimate or focus the beam, as well as the attachment point for each Matchbox laser's fibre optic cables. Two different collimating lenses were used in the course of laboratory experimentation of the MPS: a CFC8-A and CFC8X-A (Thorlabs, Newton, New Jersey, USA). Initially the beam was collimated to a diameter of approximately 1 mm, but this resulted in poor scattering signals (where particle scattering could not be distinguished from signal background) so in later experiments the beam was focused (to a diameter of apporximatly 100 μm) at the point of refraction, which yielded better results. The linearly polarised beam is subsequently circularly polarised using a quarter-wave plate, such that the total scattering reaching the detectors is effectively unpolarised. This is beneficial since the effect of polarisation on scattering (which can be significant) does not need to be considered during scattering simulations.

2.1.3 Scattering Collection Regions

While it would be possible to detect scattering from several different regions, this not only adds complexity, but would likely incur diminishing returns with regard to the additional data collected for each new detector added. These would present more and more physical constraints, only able to be alleviated by increasing the size (and cost) of the instrument, which was not desirable. For these reasons, it was decided to use three detectors positioned to detect different, equally-sized regions. These regions were defined by biconvex lenses

directing light to detectors, as such the regions were circular with their size determined both by the diameter of the lens and its distance from the point of refraction. An important factor to consider was using the as much of the full 360 $^{\circ}$ angle around the point of scattering as possible, since this allows better detection of smaller particles which scatter less light. This has two unavailable areas, one where the beam enters the chamber and the other where the beam either exits the chamber or terminates via an internal beam dump.

Since, for unpolarised and circularly-polarised light, the scattering will be equivalent at any point which is a given number of degrees away from the incident beam on the azimuthal plane, there is no requirement for all collection areas to be placed in the same plane and on the same side of the chamber. By taking advantage of this, two of the collecting lenses were placed on one side of the chamber, and a third on the opposite side - all on a single plane (figure 2.3). This allowed for the collection regions to be larger (thus making the instrument more sensitive and increasing its ability to detect smaller particles), although this means the collection angles may overlap. This overlap presents an issue since the greater the overlap between the regions, the less of a distinction there will be between the scattering collected by each, but by minimising this overlap, the validity of the comparisons can be maintained and allow for greater sensitivity. While it would be possible to alter the positions further such that the lenses would not sit on the same plane, and thus potentially allow for more lenses in the same area, it was decided that the added complexity of both potentially simulation calculations and manufacturing outweighed the possible benefits.

The lenses used were 1 inch in diameter, positioned 23 mm away from the point of refraction, such that at their diameter 48 $^{\circ}$ of the scattering arc would be collected. These

lenses were positioned, all on the same plane, centred at 58.5 °, 90.0 ° and 121.5 ° from the direction of the beam.

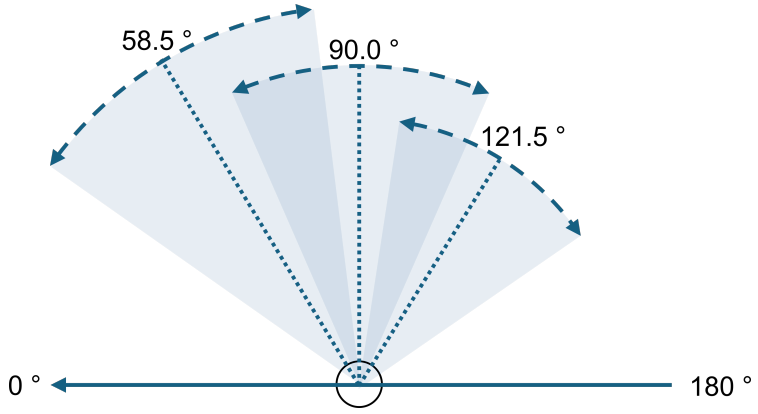

Figure 2.2: Diagram showing the 48 ° regions of scattered light which will be collected and measured by the MPS, relative to the direction of the incident light.

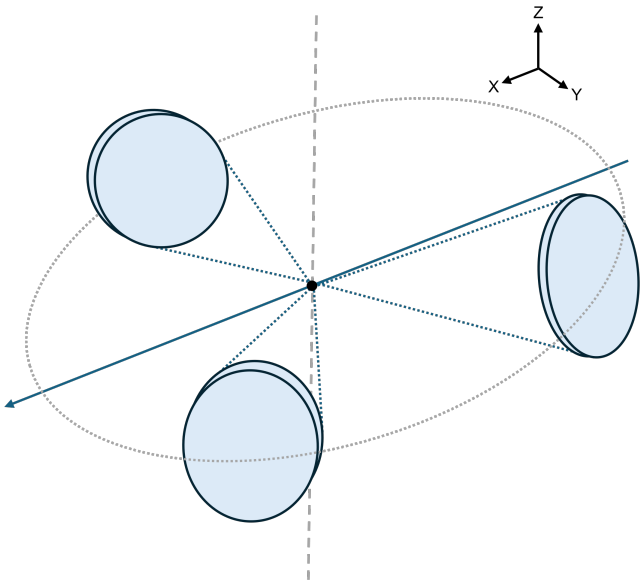

Figure 2.3: Diagram showing The approximate 3D positions of the lenses relative to the incident beam. The blue arrow represents the path of the laser beam, the vertical dashed grey line shows the axis along which the aerosol will travel. The black dot signifying the intersection point is surrounded (all on the same plane, donated by the dotted circle) by the three circles which represent the approximate position of the collection lenses, covering the angle ranges shown in figure 2.2. Lenses positioned 23 mm from the scattering point.

Each region comprises 4 % of the total 360 ° area within which light will be scattered, at a distance of 23 mm from the scattering point.

2.1.4 Photomultiplier Tubes

The photo-detector that was used initially in was a silicon switchable gain detector (PDA36A2, Thorlabs, Newton, New Jersey, USA). This detector did not prove sufficiently sensitive for effective particle detection. Based on these results, it was decided to use photomultiplier tubes (PMTs) instead, since they would provide increased sensitivity. The PMTs (H10721-20, Hamamatsu) used were compact ($55 \times 20 \times 20$ mm) while still providing high sensitivity, variable gain and a high data collection rate. They have a spectral response of 230 to 920 nm, so are suitable for the lasers used for the MPS. Hamamatsu manufacture a PMT with increased sensitivity in the 400 to 450 nm range, but it was unavailable at the time of equipment requisition. The sensitivity of the H10721-20 was sufficient for the work presented. These PMTs also had their threaded holes for using screws to attach to other components on the same face as the photo-sensitive surface, which was the most convenient configuration for the instrument.

A PMT is able to achieve high sensitivities by amplifying/multiplying weak photon signals via the following method. When a photon makes contact with the PMT's photocathode, it emits an electron which is focused by electrodes before interacting with a dynode (an electrode held within a vacuum chamber), which in turn releases more electrons. This amplification effect repeats several times using several dynodes, increasing the number of electrons produced each time. Finally these electrons produce a signal at an anode, thus relatively weak light signals can be detected. Figure 2.4 shows a diagram of the interior of a PMT.

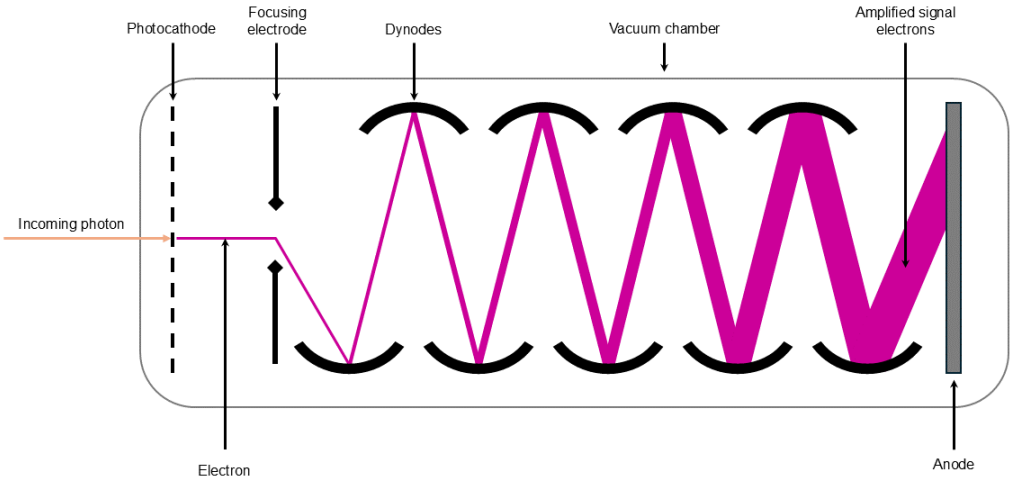

Figure 2.4: Diagram of a generic photomultiplier tube, showing the method by which weak light signals are amplified by a series of dynodes. Incoming light direction is shown in orange the induced electron amplification is shown in purple.

2.2 Aerosol

For the instrument to function, particles must travel through a single point of the laser beam, one at a time and with minimal deviation. This requires both a way of delivering a stream of particles as well as removing them from the chamber once they have passed through the beam. To maximise airflow through the chamber, the inlet and outlet for aerosols were positioned on opposite sides of the intersection point on an axis perpendicular to both the laser path and collection lens plane (figure 2.5b).

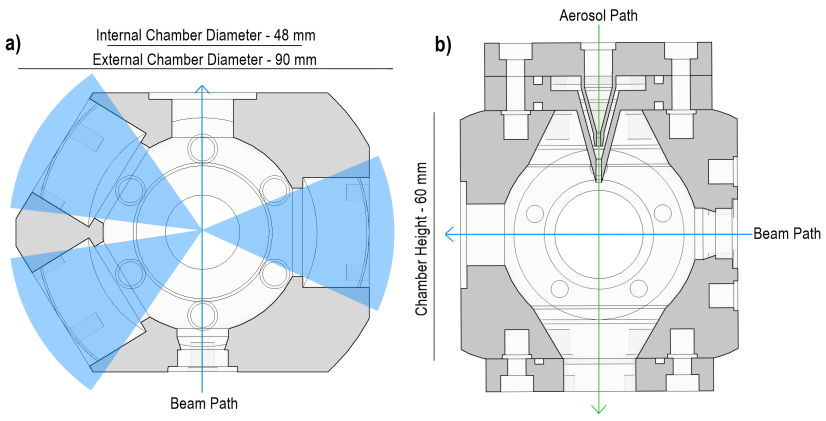

Figure 2.5: cross-section of the initial optical and aerosol setup, in (a) and (b) respectively.

2.2.1 Inlet

The aerosol nozzle input serves the vital function of ensuring that the aerosol flows in a narrow jet through the centre of the chamber, and intersects with the laser beam in a specific location. To achieve this the structure of the nozzle (shown in figure 2.6) follows the design of one published by Pan et al.[68] The design features an inner nozzle for the aerosol, which is enveloped by a larger outer nozzle. This creates a conical cavity through which flows filtered air, which forms a sheath around the aerosol.

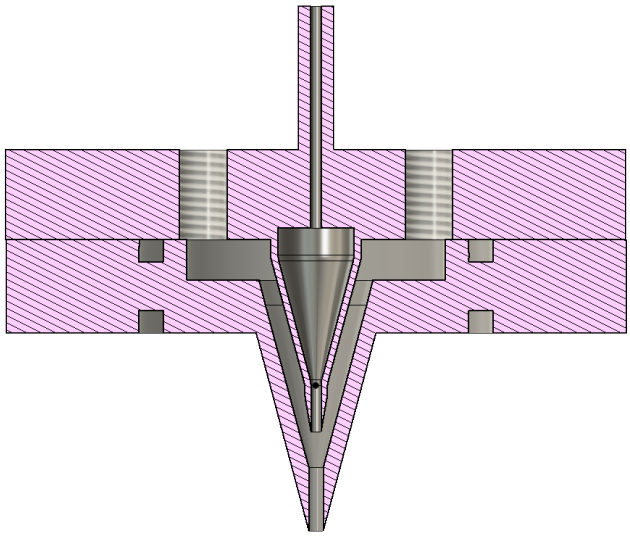

Figure 2.6: cross-section of the nozzle component, showing the captivity for the sheath flow, the o-ring grooves and the cavity created by the positions of the inner and outer nozzle.Inner nozzle diameter is 0.90 mm, outer nozzle diameter is 1.30 mm.

The purpose of this sheath flow is to minimise spread of the aerosol jet as it travels in free space, with the additional benefit of reducing any build-up of particles on the interior of the chamber, especially the lenses. The nozzle also protrudes into the chamber such that the tip is 12.5 mm away from the beam. This is important as the aerosol stream will only be kept narrow by the sheath flow for a short distance, so moving the nozzle closer reduces the chance that particles will not intersect with the beam.

The aerosol airflow is delivered to the nozzle using a $\frac{1}{4}$ inch stub, designed for attachment into a tube system by a Swaglok fitting. This is a standard diameter fitting, so that the surrounding tube system could be constructed using easily available components. The sheath flow is delivered via two 4 mm push-fit to M5 elbow connectors positioned on opposite sides to ensure the flow of sheath air within the nozzle is not biased to one side, which could compromise the sheathing effect. The nozzle is constructed of two separate pieces, as seen in figures 2.7 and 2.8. The outer nozzle, which contacts the central chamber, and the inner nozzle. The outer nozzle component incorporates an O-ring groove on both faces. The nozzle components were machined from aluminium using a 5-axis CNC machine to prevent particle loss from static buildup. Aluminium is a preferable material to plastic since fewer particles will be lost by sticking to the walls of the component due to static build-up. While heavier than plastic alternatives, the aluminium nozzle is still relatively lightweight.

It was not possible to definitely test the exact performance of the nozzle, so the design and operation were kept similar to the literature source. To induce better air flow, air was simultaneously evacuated from the chamber from the outlet to remove aerosols that have passed through the beam, to ensure there is not build-up in the chamber. The MPS was operated using low internal pressure, approximately 200 mBar.

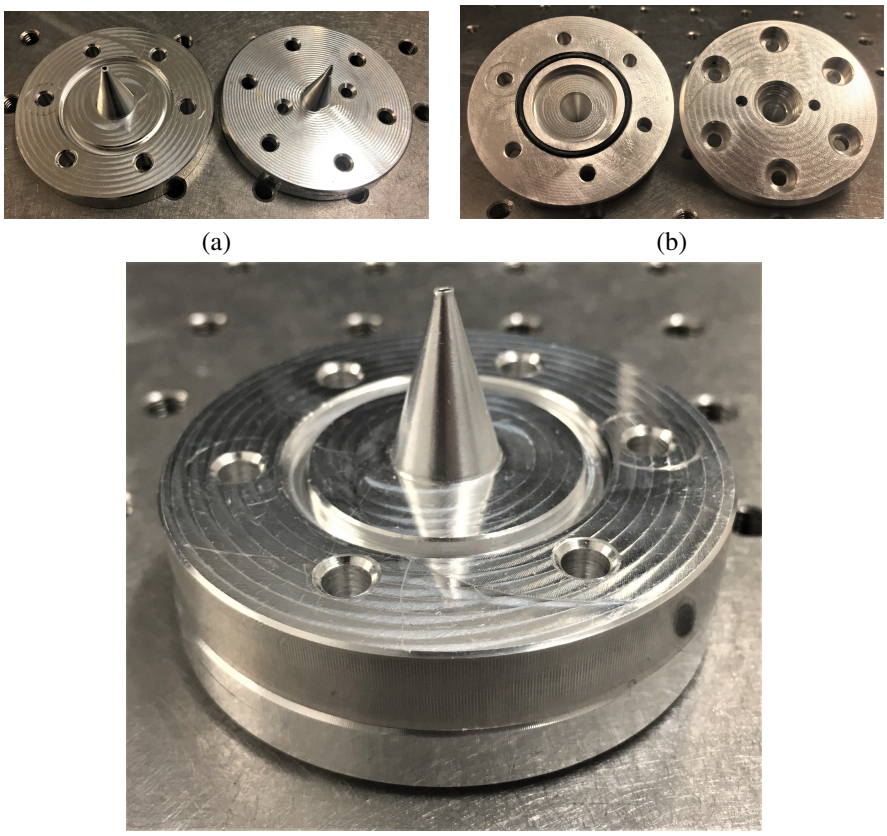

(a) (b)

(c)

Figure 2.7: Photographs of the two-part input nozzle. (a) and (b) show the two parts separated, face up and face down respectively. (c) shows the two pieces sitting together, as is the case during operation. The diameter of the component is 55.00 mm, the thickness of the two combined discs is 16.30 mm, with the outer nozzle extending a further 17.50 mm.

2.2.2 Outlet

The aerosol outlet is a simple component that acts as a mounting point for a standard $\frac{1}{4}$ inch Swagelok tube system. This is the same design used for the Swagelok attachment to the inlet. To maintain the strength of the $\frac{1}{4}$ inch stub, the internal diameter of the initial design was only 2 mm. However, this narrow internal diameter restricted airflow too much, disrupting the predictable trajectory and leading to inconsistent aerosol detection, due to the particles not travelling through the beam. This hole was expanded to a diameter of 3.5 mm, which improved flow without compromising structural integrity.

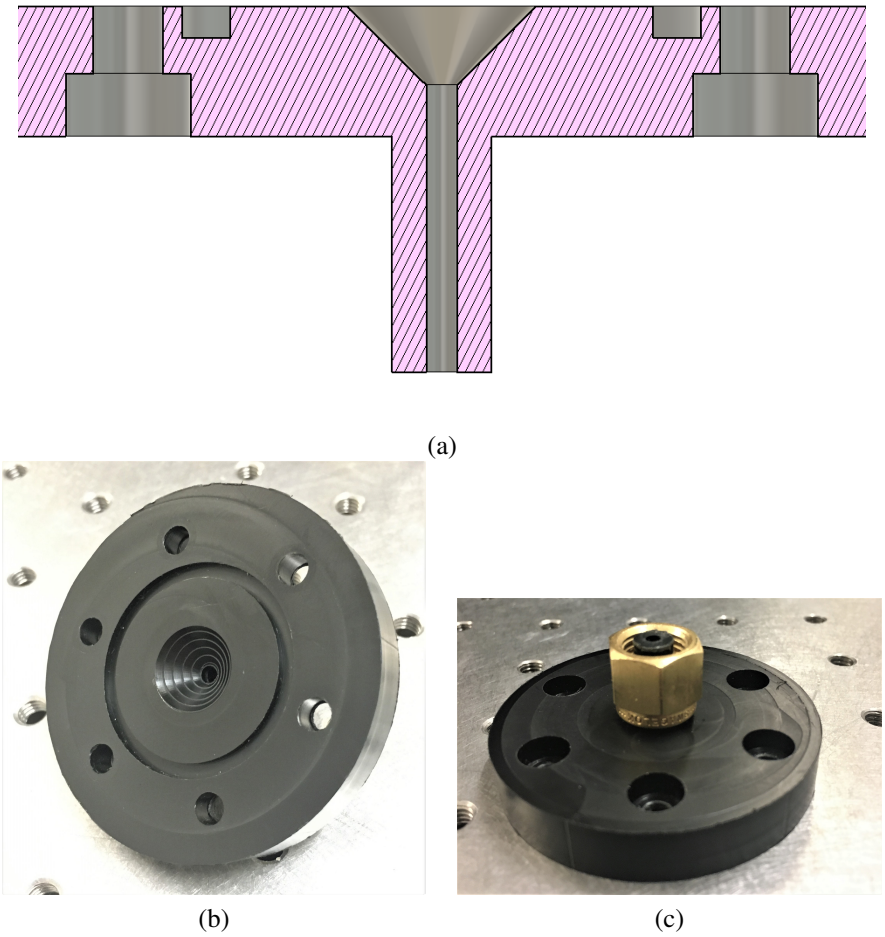

(a)

(b) (c)

Figure 2.8: (a) Outlet cross-section showing o-ring groove, counter-bored screw holes, and filleted (2.00 mm to 12.00 mm diamater) hole for air to leave the chamber. Stub was originally designed with a 6.35 outer diameter and 2.00 mm inner diameter. Inner diameter was increased to 3.50 mm to increase air-flow (b) shows the top of the outlet, (c) shows the bottom, with the stub and Swagelok attachment.

2.3 Structural

Once the desired spacial positions for the optical and aerosol components were determined, structural components were required. While it would be possible to fulfil the spacial requirements for the optics using commercially available components, custom-designed components were used to best fulfil other requirements for the instrument's functionality. All custom components were designed using *Autodesk Fusion360* CAD modelling software, and manufactured by the University of York Chemistry Department's mechanical workshop.

Some components' initial design was successful and sufficient to support proper MPS function over the course of experimentation, while others (primarily the central chamber) underwent significant redesign in order to improve functionality. Over the course these redesigns, the baseline function of the chamber - to connect other components and provide an air-tight light/aerosol integration environment - remained largely unaltered, and the changes were intended to fix issues or improve usability. Chapter four demonstrates a use-case where the chamber underwent far more drastic changes, to facilitate a modified function with increased compatibility with another instrument.

2.3.1 Chamber

Since the design of the instrument requires various components surrounding a single central point - the beam/aerosol intersection point - and would need to be positioned along different principle axes, the instrument has been based around a central, approximately spherical chamber. This chamber acts both as a mounting point for all other components, as well as helping to form an airtight environment which can maintain low pressure, and thus minimise unwanted contaminant particles from interacting with the beam. It also provides an environment with reduced internal reflection and no contamination from external light sources. The final chamber was machined from a single piece of Delrin (Dupont, Wilmington, Delaware, USA) acetal homopolymer (polyoxymethylene) plastic, which is commonly used for technical applications where high strength and rigidity is required. The initial chamber prototype (figure 2.9) was manufactured from a softer black plastic, which was not capable of maintaining screw hole threads, and was quickly worn down by the brass threaded inserts, leading to reduced structural and low-pressure integrity.

A total of five chamber designs were considered over the course of experimentation, exploring changes to collection angles, number of PMT slots, the style of mounting points for both external components and for stabilising the chamber itself. Ultimately only the first and fifth chamber were manufactured, due to long requisition timelines.

Chamber Design One

Chamber one, shown in figure 2.9, was used for much of earliest experimentation, and for the development of other components as well as during software and hardware testing. Based around an oblate spheroid, flat planes were added for each of the seven mounting points. All of the mounting faces except for the exit for the laser beam (visible in figure 2.9.b, left blank as the method of attaching the beam dump had not been determined) have holes reserved for threaded inserts for M3 or M4 screws, since the softer plastic from which it was machined would not be able to retain integrity with direct threading. Figure 2.9.c shows a side-view cross-section of the chamber, demonstrating the negative space within the chamber, which required more sophisticated 5-axis machining, but would theoretically provide a less obstructed path for flowing air and and reduce internal reflections. The lowest angle captured by a detector in this configuration is 35.5 $^{\circ}$ (detector centred at 58.5 $^{\circ}$).

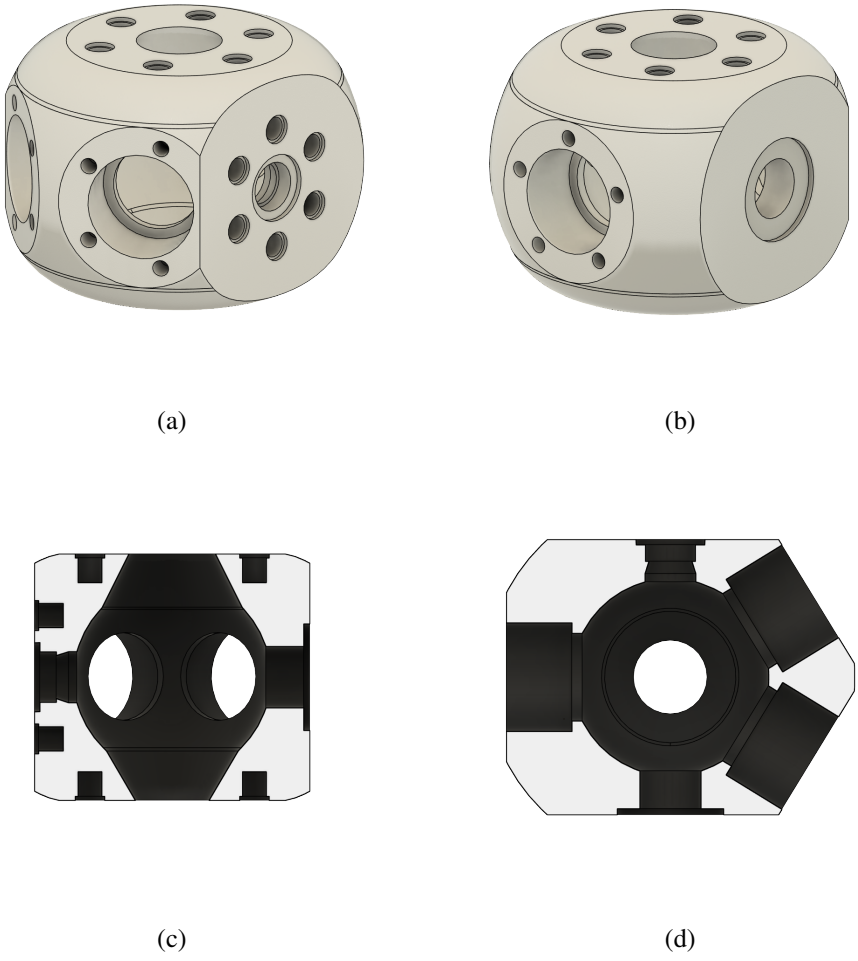

(a) (b)

(c) (d)

Figure 2.9: Model of the first chamber design, which was manufactured and used for laboratory tests. (a) shows aerosol and beam ports, as well as two PMT ports, (b) shows beam exit port and third PMT port. (c) shows a cross-section aligned the profile of the beam and aerosol paths, (d) shows a cross-section aligned with the PMT ports.

Chamber Design Two

Chamber two (figure 2.10) was the first proposed redesign. Based on a sphere, the mounting face designs were all unaltered from the first chamber design, although some of their positions were shifted. The port positions for PMT060 and PMT120 remained in their original position (figure 2.10.b). While the port for PMT090 was still positioned on the opposite side at 90 °, but it was rotated upwards about the axis of the indecent laser beam. This was done to allow for the addition of two additional ports, either to add two more PMT and lens arrays,

or so that the existing 3 could be moved around and the unused ports blocked. This was done to allow for detection of lower scattering angles, since the new ports are centred 36 ° from the beam. To accommodate this, the aerosol outlet, laser inlet and outlet ports were extended out from the central spherical body. The extra high- and low-angle detection ports were angled downwards towards the outlet since the inlet port was required to be in a specific position such that the nozzle is close enough to the intersection point with the laser beam.

The motivation behind this design was both to be able to detect lower angle scattering, which would likely improve detection of small particles due to the relative dominance of low-angle, forward scattering (confirmed via simulation), as well as providing more than three PMT ports. This would allow either for moving the PMTs based on the desired measurement angles, or to add more PMTs to the MPS' core system.

(a) (b) (c) (d)

Figure 2.10: Model of the second chamber design. (a) shows aerosol and beam ports, as well as PMT ports, (b) shows beam exit port and remaining PMT ports. (c) shows a cross-section along the aerosol path, (d) shows a cross-section aligned with two of the PMT ports.

Chamber Design Three

Chamber three (figure 2.11) follows the same principle as chamber two: Add more ports to the design to give additional analytical capability and flexibility. Chamber three has a total of six ports, two positioned at 90 ° (figure 2.11.a,b), as well as ports at the original high and low angles (figure 2.11.a,c). Additionally, two more ports at lower angles of 45 ° were added

(figure 2.11.b,c). Two extensions were added to the bottom of the chamber (best visible in figure 2.11.b,c) to make space for threaded holes, so that the chamber can be directly mounted securely to an optical stand or similar component. The holes were spaced 75 mm apart. This distance was kept to increments of 25 mm to allow easy integration with common optical table thread spacing, including the Thorlabs (USA) used during all laboratory work.

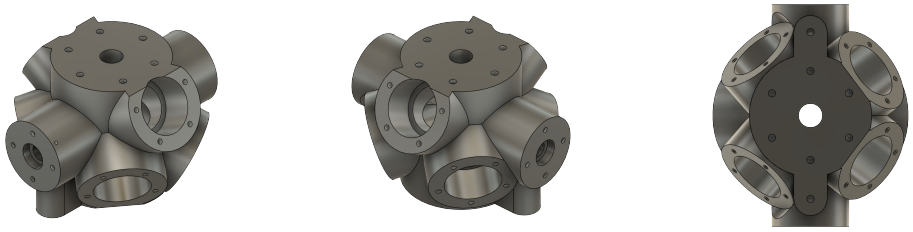

(a) (b) (c)

Figure 2.11: Model of the third chamber design. (a) shows aerosol and beam ports, as well as PMT ports, (b) shows beam exit port and remaining PMT ports. (c) shows the underside of the chamber, including the mounting threaded holes.

Chamber Design Four

Ultimately, it was decided that a focus on improving the existing configuration would take precedence. As part of this development, chamber four (shown in figure 2.12) was proposed. The positions of the lens and aerosol ports are identical to chamber one, although the laser ports have been extended out from the main body slightly. Chamber four also has points like chamber three, where the chamber can be secured in place, although this design has four threaded holes instead of two. There are also no negative draft angles within the chamber centre; this makes machining the chamber less complex. There is potential for this to cause turbulent air flow as well as additional internal reflections (due to the sharp internal edges and their increased proximity to the chamber's centre), factors whose effect on data would need to be evaluated.

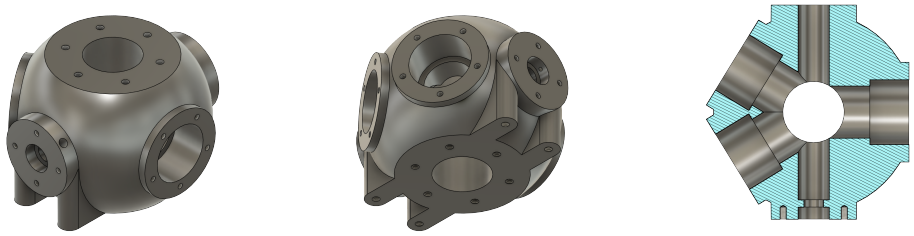

(a) (b) (c)

Figure 2.12: Model of the forth chamber design. (a) shows aerosol and beam ports, as well as PMT port, (b) shows the remaining PMT ports and underside of the chamber. (c) shows a cross-section aligned with the PMT ports.

Chamber Design Five

Chamber five (shown in figure 2.13) was the final chamber which was manufactured for use in laboratory experimentation. In terms of functionality and geometry, it is almost identical to chamber four. However the shape of the body has been changed in order to simplify the machining process: The body was based on a larger diameter cylinder with champfered ends. This had the additional effect of increasing the mass of the chamber. This is not a concern in terms of wasted material due to the subtractive machining process, but does add weight to the final instrument. The chamber was made from relatively lightweight Delrin so this did not prove a major issue. This chamber being made from Delrin meant it could support threading, thus eliminating the need for threaded inserts which had proved unreliable for maintaining an airtight seal. The laser ports had countersunk holes of a larger diameter (0.5 inch) than the through-hole for the the beam path. This allowed for standard 0.5 inch optical windows or neutral density filters to be temporarily glued into place, which would create an airtight seal while allowing the beam to enter and exit the chamber. This was made possible by using a mount for the collimating lens which sat away from the chamber, thus allowing the lens to not form part of the chamber seal. This also allowed for the potential to add more

optical components in between the collimating lens and the chamber. Two methods were used to achieve this, detailed later in this chapter.

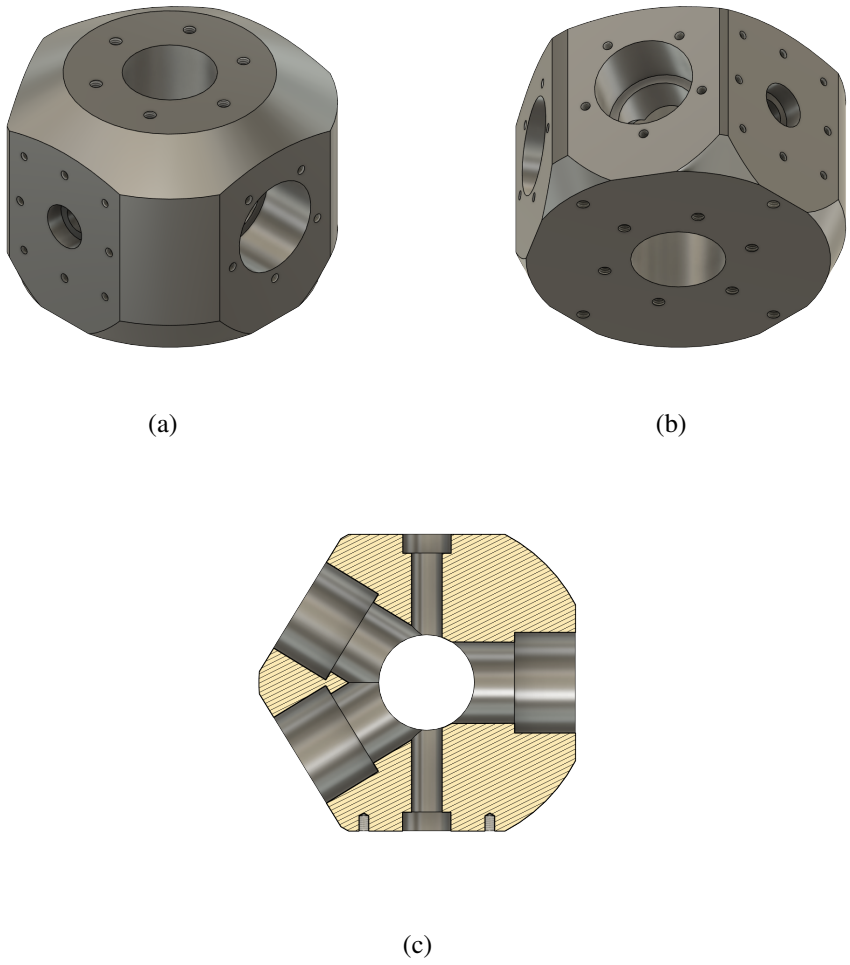

(a) (b)

(c)

Figure 2.13: Model of the fifth chamber design, which was manufactured and used for laboratory tests. (a) shows aerosol and beam ports, as well as PMT port, (b) shows the remaining PMT ports and underside of the chamber. (c) shows a cross-section aligned with the PMT ports.

The modular design of the MPS allows for the redesign and interchanging of individual components without a complete redesign. Since the position of the detectors affects the region of scattered light detected, different detector configurations may allow for better characterisation, for example if there is distinctive scattering at a low angle. There is potential to decrease this minimum angle to 13° (detector centred at 36°) as seen in the third chamber

design, while maintaining lens range (and angle coverage) consistent with the previous design. This would allow detection of lower angle scattering and potentially a decrease in detection overlap. Currently azimuthal lens position has not been extensively considered since all lenses and detectors sit on the same plane. Adding/moving lenses off this plane would necessitate considering light polarisation (if the $\frac{1}{4}$ wave plate was not being used to circularly polarise the beam), but could also add to the MPS' characterisation potential.

Even with a filtered clean air flow through the instrument, there is still likely to be scattering of the laser which is detected - confirmed by detection of increased signal while the laser is on, regardless of the presence of PM. This has two possible sources, scattering off the interior instrument surfaces, and Rayleigh scattering from gas particles in the filtered air within the chamber. In order to determine the source of this scattering, PMT signal was monitored while the air pressure in the chamber was reduced to approximately 200 mBar and allowed to re-pressurise over several minutes. This pressure change would have an effect on the PMT signal only if the source of the scattering was Rayleigh scattering from gas particles, and signal would increase linearly with increasing chamber pressure. The pressure change would have no effect on scattering from surfaces.

It was observed that changes in chamber pressure below STP has no observable effect on scattering detected by the PMTs. This indicates that the scattering within the chamber is dominated by surface scattering, rather than Rayleigh scattering. This emphasises the need to minimise this internal surface scattering, in order to maximise the potential to detect weak PM scattering. Ways of achieving this include altering the light-scattering properties of the surfaces in the chamber. This could be done by choosing a different manufacturing

material, but would likely be more easily achieved using a matte-black coating such as a paint on existing and future surfaces. This is a common practice when working with optical instruments.[65] A prime candidate for this is the aluminium nozzle assembly, which currently has a highly reflective surface (although it is notable that there is still significant scattering even while the nozzle is not present). Other components such as the PMT/lens mounts and the aerosol outlet are manufactured from black Delrin, but still present a scattering risk due to its smooth finish. The central chamber is 3D-printed from black nylon, but the interior cavity is uneven and could have its scattering-potential reduced via different manufacturing techniques or a paint-coating. Another reduction method is would be replacement of the beam dump to one that is more effective at terminating the beam with no light escaping. A Thorlabs BT620/M beam trap was used in later experimentation, with a neutral density band pass filter window forming a chamber seal.

2.3.2 PMT spacers

The scattering collection array of the MPS is comprised of three PMTs, each with a bi-convex lens (with a focal length of 25.4 mm) focusing a portion of scattered light into its photosensor. For the MPS to function, each lens and PMT pair must be held in a constant position, relative to both each other and the intersection point. Additionally, the lenses must form an airtight seal with the chamber. To achieve these requirements, a component was designed to hold the PMT and lens in place, while applying pressure to the lens to compress an o-ring and seal the chamber lens ports, while being hollow in the centre and not impeding the passage of light between the lens and PMT photosensor.

These PMT spacers were machined from black Delrin, the same as the chamber for the same

reasons: The material would need to remain rigid under pressure, as well as minimise internal scattering and reflection. These spacers are secured to the chamber by five M3 screws, to ensure a consistent position and apply even pressure to the lens. A cylinder with an 26.5 mm diameter wall thickness and an internal chamfer extends into the lens port and applies pressure to the biconvex lens. The lens is pressed against a 2.55 mm lip on the chamber's lens port, between which is held by a 1 inch o-ring, to maintain the chamber seal. The other end of the spacer attaches to the PMT via its front facing M2 threaded holes surrounding the photosensor. Counter-bored holes in the outward face of the PMT matched these, providing a secure fitting. This attachment was not required to be airtight, since it was external to the chamber.

The initial design of the spacers proved suitable for the duration of instrument development and data collection, and no further modifications were required.

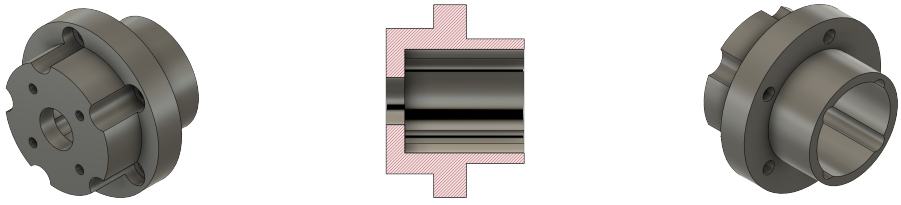

(a) (b) (c)

Figure 2.14: Model of the PMT spacer. (a) shows the face onto which the PMT is connected, (b) shows a cross-section, and the hollow centre of the component, and (c) shows the side which extends into the chamber to hold the lens in place.

2.3.3 Collimating Lens Holder

This three-part component was designed with the goal of holding the collimation lens in place, away from the chamber. One of the advantages to a configuration where the collimating lens

does not make up part of the airtight seal of the chamber is that it allows for a far more simple window to be used in in its place. Additionally, this space would allow for the inclusion of a quarter wave plate or similar optic. The entire holding assembly, including collimating lens, could be removed from the chamber without compromising its seal. A larger distance between the lens and the intersection point also allows for more reliable collimation and focusing since the collimating lens struggled to consistently collimate the beam at a distance less than about 30 mm of the lens.

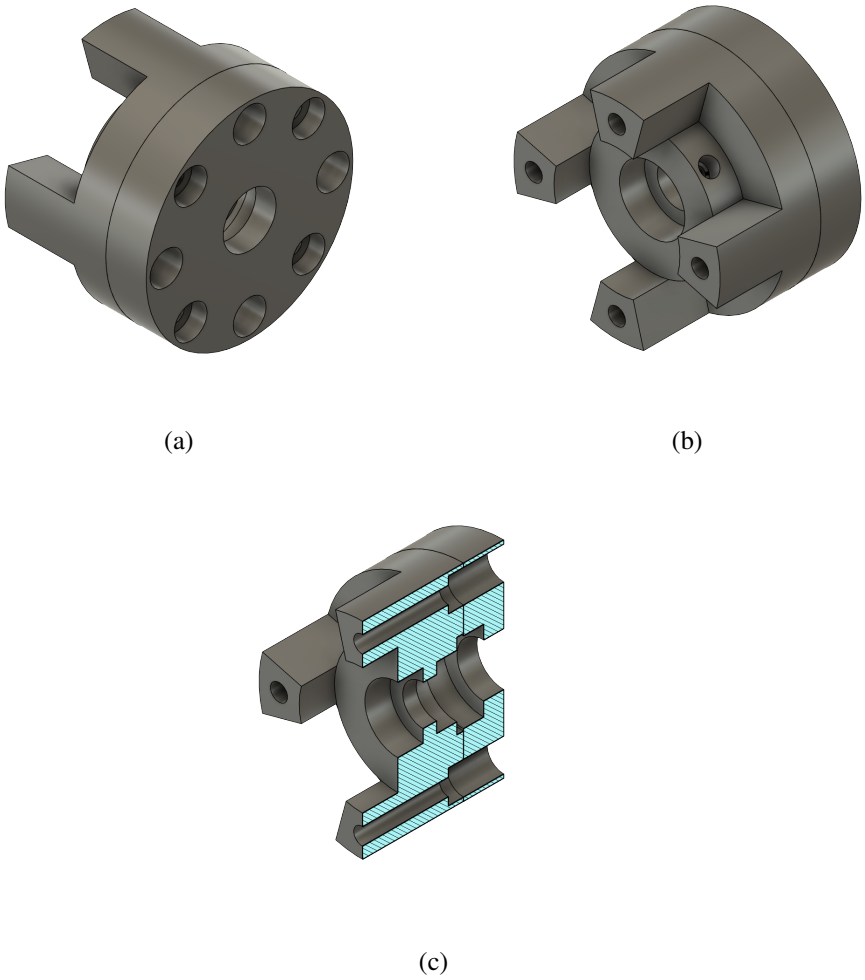

Figure 2.15: Model of both parts of the collimating lens holder. (a) shows the cap which secures the collimating lens while still allowing the entire holder to be detached from the main MPS body. (b) and (c) show the four hollow legs through which the holder is screwed into the chamber and a cross-section of same, respectively.

2.3.4 Optical Cage System

The Collimating lens was connected to the central chamber via a 30 mm Thorlabs cage mount. This facilitated both easy variation in the distance between the beam origin and the chamber, as well providing a mounting point for apertures, dichroic mirrors/beamsplitters and polarising lenses among other components when required during instrument development and testing. Figure 2.13.a shows the face to which the cage system is attached via four screws.

2.4 Electrical Hardware

2.4.1 PMT Power and Signal Application

In response to detecting light, the H10721 series PMTs (HAMAMATSU, Japan) each produce a signal voltage. Before being passed to the DAQ, and subsequently to the PC, a transimpedance amplifier (TIA) is used both to convert the current to a DC voltage, and amplify the signal.

The amplification of the signal from each PMT can be varied independently (each controlled using a potentiometer), allowing for the different intensities of scattering reaching each detector to be made detectable. Each PMT outputs a voltage which is passed to the potentiometer, for which the resistance can be manually adjusted, changing the outputted voltage which is returned to the PMT. The PMT's signal is amplified based on the change in the voltage after it returns.

The PMTs require power to operate, and their signals need to passed to a computer for

collection. During potential future development of the MPS, all the electronic components may have been housed together with the MPS chamber and accompanying optical and aerosol arrays. However, this would present additional difficulties during early development, while designs are not finalised. For this reason, the power supply and potentiometers were housed in a small, separate box.

The front panel of the box features sockets for the PMTs analogue signals, via three SMA connection. Three M8 circular 4-pin connectors each facilitate the two potentiometer voltages, as well as power for the PMTs. The potentiometers are also mounted in the front panel such that the dials are accessible for adjustment by hand.

The back panel holds the connection for the power supply, as well as three BNC connectors which transmit the signal to the data acquisition device (DAQ).

2.4.2 DAQ

These signals were digitised using a DAQ (National Instruments) and recorded by a custom LabView (National Instruments) program. The DAQ was wired to digitise all three PMT signals, as well as transmit air flow data between one and three mass flow controllers (MFCs) which were used to monitor and/or limit air flow at different points in the aerosol delivery system. These digital signals are sent to the PC, and when the MFCs are being controlled externally, those signals are sent to the DAQ from the PC.

2.5 Software

2.5.1 Laser Control

Both lasers were controlled via USB connection to the PC, using associated software (Integrated Optics). The software allowed control of the laser power by setting the current delivered to the laser, as well as displaying device temperature. This would allow immediate activation and deactivation of the laser. However, activation of the laser produced a brief (less than a second) fluctuation in laser power, which would invalidate measured signals immediately after activation. This did not cause issues during primary data collection, since the laser was left on for the duration of data collection and only discrete peaks were analysed, but was considered in scenarios where continuous PMT signals were collected.

2.5.2 LabView

LabView (National Instruments) was used for the MPS software. The functionality and capabilities of the software expanded greatly over the course of development, but its core functionality remained the same: Process and collect MPS voltage data. It did this via use of a DAQmx reader vi which is included in LabView software as a means to streamline communication between the DAQ and the PC. The parameters of the signals received from the DAQ, principally rate (in Hz), could be defined by the user within the program.

Initially, all data was collected in an array and updated using a shift register, before being written to a newly created file along with termination of the data collection session. However, this proved exceptionally inefficient and slow, as well as introducing risk of a software crash causing data to be lost. For this reason, an array containing data from each

PMT for that collection cycle (usually 5-10 cycles per second) was added to a data queue in the same loop that it was being collected from the DAQ. This data could then be dequeued in a separate loop dedicated to appending the data to text files created with initialisation of the program. These files were loaded upon creation and not closed until data collection was terminated, whereupon any data remaining in the queue could be quickly dequeued and written to the files before the program stopped running. This proved much more effective, minimising risk of data loss as well as allowing for longer periods of data collection without significant slowdown or excess RAM usage.

The software was able to optionally perform a multitude of processes when required, including displaying waveform data and producing snapshots of the current waveform with adjustable resolution. It could also perform peak detection with adjustable threshold and width parameters and display a continuously updating history of the mean and standard deviation over session time, as well as produce a live histogram of peak amplitude. Components such as MFC control, data collection and peak detection could be enabled and disabled at will, based on the currently desired function. MFC set flow rate, PMT data acquisition rate and data saving directory input could also be manually set.

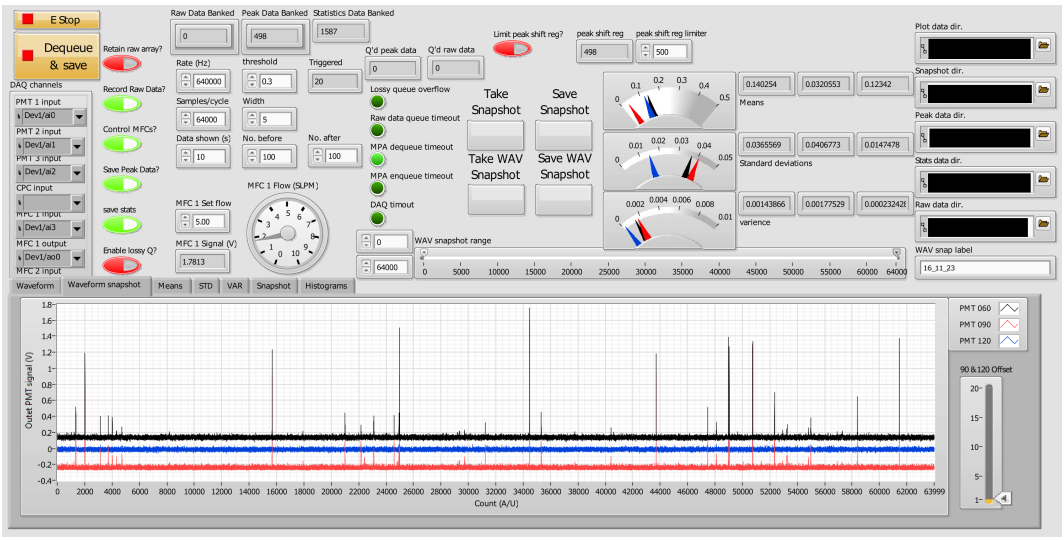

Figure 2.16: LabView MPS operating software, front panel.

Raw Data Processing

PMT data consists of a series of voltages recorded at a dictated rate (normally 0.5-0.64 MHz), written as a new line to an open text file at another user-determined rate (usually 5-10 Hz). This is done for all three PMTs, resulting in three text files generated every time the program is run. These delimited text files can be read using an R script, to allow for data analysis and visualisation. These files become large quickly, depending on the acquisition rate, as large as hundreds of megabytes each within a few minutes of operation.

A timestamp is created once data collection is started, and the design of the program and use of queues ensures that the three raw data files do not deviate from each other in terms of absolute time. Time-based misalignment was further controlled for using the peak detection system described below. Peaks detected by each PMT, identified as originating the same source particles, were determined to show microsecond-level time agreement, meaning that there is not a risk of peaks being grouped by source particle incorrectly

Threshold detection and Peak Collection

Due to the high maximum acquisition rate of the PMTs, and the brief and infrequent windows of time where any given particle was interacting with the beam, only a small percentage of the data is required to perform peak analysis. For this reason a peak detection system was implemented to limit the data collected to that necessary to perform peak analysis. This significant reduced the size of data files and thus sped up later data processing and analysis.

The definable parameters include the peak threshold and width. The signal must exceed the threshold value for a number of signals greater to the width for a peak to be recognised and the signal data to be retained. The number of points either side of the trigger point, where the signal first exceeded the threshold value, could be independently varied.

Threshold values were set manually based on an observed background signal, so that even small peaks could be detected, but few if any 'false peaks' were erroneously detected. The width parameter was found most effective when kept between 5 and 10, at no point were non-particle based peaks an issue. Points before and after trigger point were kept equal, usually between 50 and 200, as this was enough to ensure capture of the whole peak profile while being able to obtain a background signal from before or after the peak. Depending on the exact data acquisition parameter set for each experiment, these windows represent between about 100 and 500 microseconds of scattering data.

2.6 Auxiliary Components

In order for the MPS to function in laboratory conditions, several external components are required to perform specific tasks. This includes creation of a filtered air flow which can be then loaded with known test particles to be analysed. Air flow was induced using a

vacuum pump, which as alternately used to produce a low pressure internal environment or compressed air flow. To filter this air flow, Alicat (USA) in-line filters were used, since they could be integrated into a $\frac{1}{4}$ inch swagelok system. A full diagram of the MPS and its connection to additional components, including an airflow path and particle generation diagram is presented in figure 2.17.

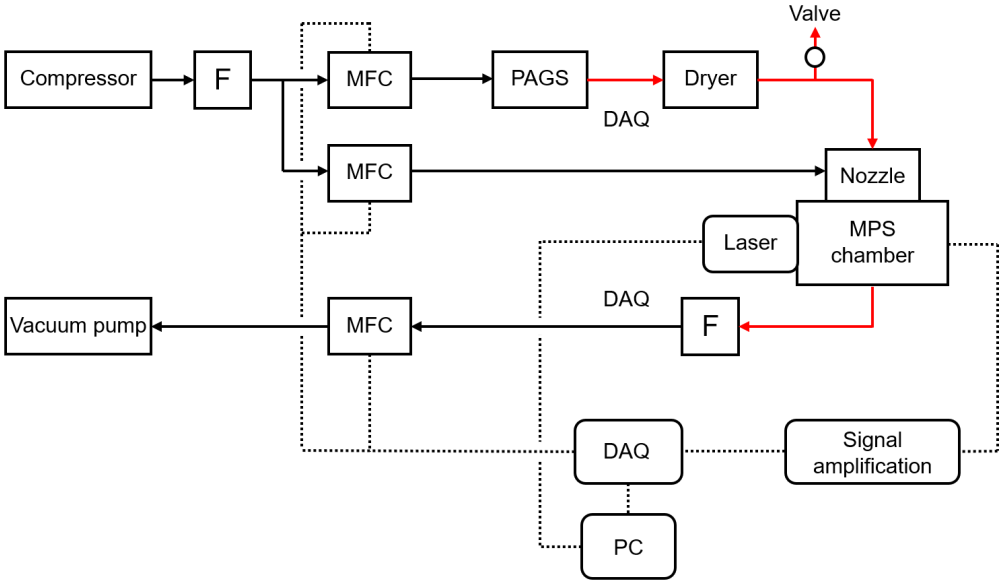

Figure 2.17: Diagram showing the particle generation setup of the MPS, as well as the PC connection to MFCs, laser and PMTs. Boxes labelled "F" represent in-line air filters. Solid black arrows show clean air flow(no added aerosols), solid red arrows show airflow seeded with particles from the PAGS, and dotted black lines show a data connection.

2.6.1 Particle Generation

In order to test the aerosol characterisation potential of the MPS, a controllable and robust system for aerosol generation of known, monodisperse particles was required. In places flexible tubing was required, conductive tubing was used to prevent static buildup, which would cause airborne particles to stick to the internal surface of the tubing, reducing the effectiveness of the particle generation assembly.

Portable Aerosol Generation System

The primary particle generation device used for experimental work was the Handix Scientific (USA) PAGS (portable aerosol generation system), which used high pressure airflow to aerosolise particles from a water-based suspension. This suspension was placed in a receptacle with an inlet for high pressure air which induces nebulisation in the liquid suspension, and an outlet to deliver the aerosolised particles. The PAGS also includes a clean air bypass, which allows either just clean or seeded air, or any mixture of the two.

Use of the PAGS for aerosol generation was always immediately followed in the aerosol generation system by a in-line dryer; a cylinder containing silica gel beads to absorb moister and dry the newly generated aerosol. This would be important as a layer of water on the aerosol would change the diameter of the particles, as well as the refractive index and particle composition (effectively becoming core-shell particles). It could also potentially introduce lensing effects. It is possible that some portion of the aerosols were lost due to the dryer, but experimentation demonstrated that aerosol delivery to the chamber was more than sufficient to gather large quantities of scattering information quickly.

The PAGS was, in the course of all following experimental work, only used to generate polystryene latex sphere (PSL) aerosol, of varying size and colour. Stored as a dense suspension, the PSL beads were diluted in distilled water for use with the PAGS.

Printed Fluidized Bed Generator

Although no data from particles aerosolised using the PRinted FluidIZed bed gEnerator (PRIZE) system has been included in this thesis, it will be described here owing to its

potential to be deployed for future work with the MPS. This alternative particle-generating system was based on a published particle generating system.[69]

The system is custom made, taking the published design and modifying it for integration with the current MPS aerosol system. This allows for the system to made directly compatible with the current flow-network, decreasing the potential for leaks and other points of failure, as well as reducing wait-time if replacement or modified components are required. The printed fluidized bed generator (PRIZE) functions by laying a small quantity of test dust over a 1-inch diameter bed of 100 µm beads and an 80 µm mesh. This can be seen in the internal diagram in figure 2.18. Clean air is pushed up through the bed, aersolising the test dust. This has the advantages of creating a dry aerosol, thus eliminating the need for a dryer and subsequently streamlining the setup. Dusts that were considered for testing include Arizona test dust, Arizona test dust, DMT quartz dust[70] and 0-5 micron iron oxide dust.[71] These would a provide particle sets of relatively known size distribution, as well as non-spherical particle shapes.

Figure 2.19 shows the main body of the PRIZE, as well as the lid to keep the PRIZE chamber contained and the disc which would disperse the flowing air through the fluid bed. The main body is a simple rectangular metal body which can be secured an optical table, and an o-ring groove to allow the lid to create an airtight seal. Within the body is a cylindrical cavity, with a notched funnel at the bottom to allow the disc to sit securely at the base of the chamber. There is a $\frac{1}{4}$ inch threaded hole to allow an NTP fitting to be secured, through which pressurised air flow can enter the bottom of the inner chamber and flow upwards through the fluidised bed. The initial design of the disc (figure 2.19.e) was replaced with

design (figure 2.19.f) which would be stronger and easier to manufacture. The reduced number of slits proved more than sufficient to sustain nebulisation.

Through testing, it was found at a low flow rate of less than 1 lpm was sufficient to agitate the fluidised bed and in turn agitate the solid particles, resulting in nebulisation.

During initial testing, the nature of the fluidised bed meant that exchanging particle types also required the removal of the now contaminated bed particles. Although separation and reclamation of the glass beads would be possible with the right process and equipment, that ultimately did not prove necessary. Another observed issue was the solid particles quickly deposited on the inside of the MPS chamber. This would have the effect of reducing transmission through the lenses, as would require significant disassembly of the MPS for cleaning.

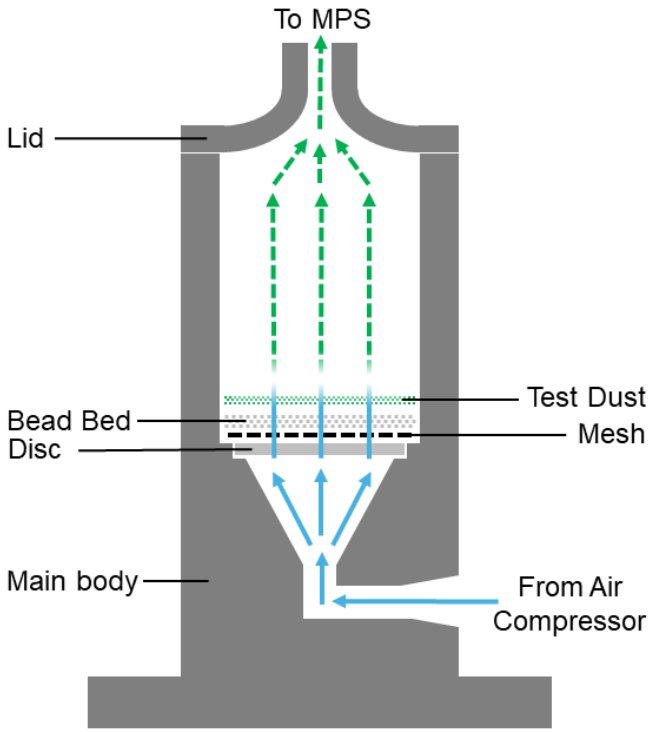

Figure 2.18: Internal diagram of the PRIZE, showing the flow of air and the aerosolisation of the test particles induced by the agitation of the bead bed.

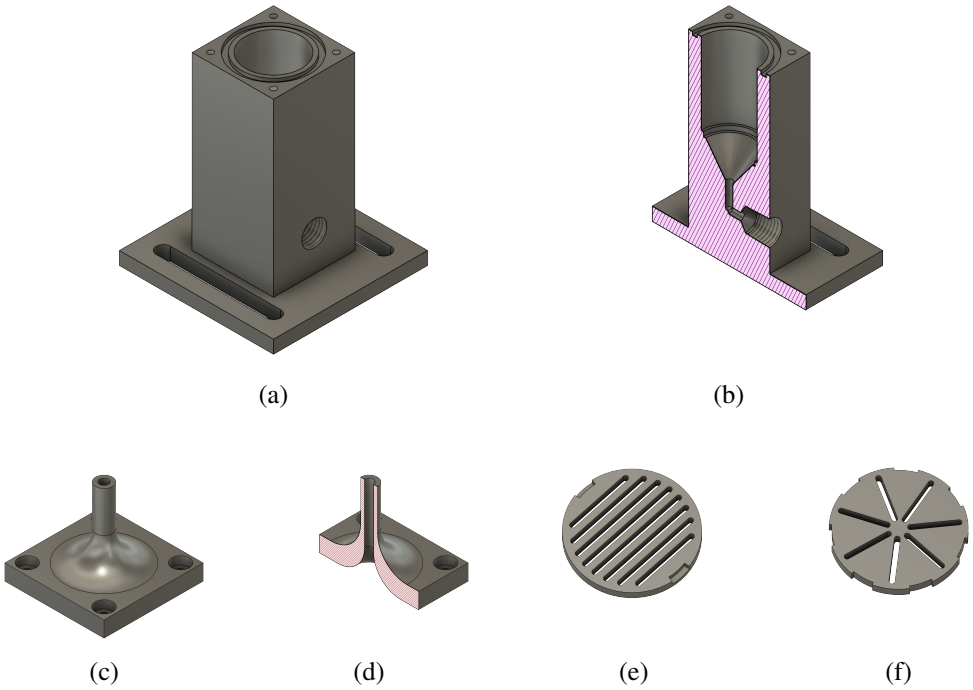

Figure 2.19: Models of PRIZE components, including the main body (a, b), lid (c, d) and filter disc (e, f).

2.6.2 Condensation Particle Counter

The particle counter (CPC) operates by inducing condensation of a liquid (in this case butane) onto the particles, in order to increase their size and allow for detection and subsequent concentration quantification using light refraction. The Condensation Particle Counter (CPC) has two modes of operation; high and low flow (1.5 lpm and 0.3 lpm, respectively) while the upstream and downstream mass flow controllers (MFCs) are precisely controllable with a maximum rate of 5 and 10 lpm respectively. The CPC allows verification of both the presence and quantity of PM but also that the system does not contain stray air particles when test particles are not being generated.

2.6.3 Mass Flow Controllers

Up to three mass flow controllers (MFCs) (Alicat, USA) were used simultaneously to manage airflow throughout the aerosol system. MFCs were either controlled manually via an inbuilt control panel, or using the functionality added to the LabView software, via connection to the DAQ. MFCs were always preceded with an inline air filter, to avoided loaded air flowing through them and possibly causing damage.

2.7 MPS Performance

During the development process, the MPS and its components were continually tested. This included tests of the laser along with associated lenses and optical components, air pressure tests, photodetector evaluation and calibration, as well as others. The signal recorded from the the PMTs without any laser or external light input was found not to contain any unexpected

noise or contamination. Scattering signals of even the smallest PSL particles analysed were definitively distinct from the background noise observed within the PMT signals.

2.7.1 Amplification Calibration

Since the gains of the three PMTs were varied manually via potentimeter, the relative signals cannot be accurately or productively compared without calibration. Via use of a uniform light source, the relative gain being applied to each PMT can be determined, resulting in direction factors that can be applied to collected data so that PMTs signals can be cross-analysed.

To simplify analysis, the gain for each PMT was usually set manually according to the background signal caused by the beam in a clean chamber and were not altered between data collection sessions unless it could not be avoided. This way a single set of gain correction factors could be applied to all data collected with the same set gains.

Chapter 3

MPS Capabilities and Experiments

3.1 Introduction

This chapter is concerned with experiments performed using the MPS, in order to assess its capabilities, both as a standard OPS instrument, and how its novel design impacts its analytical abilities. It is a culmination of the work presented in chapters one and two; where the theoretical and experimental coalesce, in order to test the veracity of both.

3.2 Simulation of Instrument Data

With the spacial and optical parameters of the MPS known, Mie theory scattering models can be used to simulate the scattering detected by the MPS. This simulation is able to take into account the geometry of the MPS, as well as the wavelength of laser selected. The Mie theory simulation was based on the model published by Bohren and Huffman in 1998, as mentioned in chapter one.[45] This model requires the size parameter of the particle and complex refractive index (CRI) as inputs, and is able to calculate a simulated full-angle scattering

phase function for that particle, as well as properties such as scattering cross-section. With the angle ranges covered by the collection lenses which direct light to the PMTs known, the proportion of scattered light collected by each lens can be determined from the Mie model data.

From this, the relative magnitude of scattered light detected by each PMT can be predicted, either as a set of three scattering intensity values, or as three ratios comparing these values. This is part of the advantage of using multiple detectors, as the relative scattering within each angle range will often be more sensitive to minor or localised changes in the scattering phase function of a particle, than the scattering within a single large angle range.

This initial simple MPS data simulation method is fast, but only simulates a 2-dimensional approximation of the MPS. The scattering intensity is calculated for a series (the total of which is user-defined) of angles comprising the full 180 $^\circ$ range, but this does not account for the 3-dimensional space within the chamber, and the circular lenses. Given that the PMTs are detecting light which is focused by the full lens area rather than a single line across it, the MPS data simulation should cover a full 3-dimensional area. The existing code had limited ability to do this, so additional calculations were added to the simulation to approximate a fully 3-dimensional scattering sphere. Using the centre point of each lens (e.g. $\theta = 90$ $^\circ$ for PMT90), and the angle segment covered by each lens (48.6 $^\circ$), an array was created containing a sequence of azimuthal angles from $\phi = 0$ $^\circ$ (aligned with the orthogonal plane) to $\phi_{max} = 24.9$ $^\circ$ (the maximum distance from the orthogonal plane). It is important to keep the step value between ϕ values equal to the step value between θ values, so that the grid of discrete points with a scattering value within the 3-dimensional scattering environment is

uniform. Using Pythagoras theorem, the θ angle-range collected at each ϕ angle increment was determined for each lens and held in matrices, with this θ range decreasing as the ϕ angle approached ϕ_{max}. With this one half of each lens coverage has been approximated as horizontal 'bands' of θ angles, so using the calculated 2-dimensional scattering data, the scattering collected by each band can be totalled to obtain the total scattering collected by that half of the lens. By doubling these values to account for the other half of each lens, the total scattering collected in 3-dimensions can be determined.

Both this and the underlying 2-dimensional method for determining the scattering by each lens are dependent on selecting an increment or step value, so that the scattering can be calculated at each discrete angle. By decreasing this step value, the resolution of the resulting phase function increases, along with the time required to perform the simulation. This also means that simply totalling the scattering values within a given angle range will give an essentially arbitrary value, since it will increase with the increased precision of smaller step values. To account for this, the scattering values can be normalised by determining the total scattering calculated for the full 180 $^\circ$ range, and the scattering predicted for each PMT can be represented as a proportion of the whole.

This same above-described method to use the 2-dimensional phase function to approximate a full 3-dimensional environment was also utilised to calculate the total scattering expected at all possible angles, by using $\phi_{max} = 90\ ^\circ$, so that all 360 $^\circ$ are included in the eventual scattering total.

3.2.1 Quantifying the Benefits of Multiple Detectors

The basis of using multiple detectors for the MPS was to give it the ability to be less dependant on Mie theory and assumptions of particle sphericity and pure scattering behaviour with no absorbing component. Figure 3.1 shows a demonstration of this. Typical OPS instrument use a single detector, capturing light from a wide angle range, centred 90 $^{\circ}$ from the incident beam. An equivalent to this is using the data from only PMT090. Figure 3.1 shows that while a single detector shows good size-discrimination of a non-absorbing PSL particle in the 400-600 nm diameter region, the signal from a larger PSL particle with an absorbing component would be indistinguishable from a smaller non-absorbing PSL particle. Two examples have been highlighted in figure 3.1; a 500 nm black PSL particle would produce the same signal as a 419 nm white PSL particle, and a 600 nm black PSL particle would produce the same signal as a 431 nm white PSL particle. A further problem is that this error caused by assuming non-absorbing particles is that the distortion is not uniform, so it would be difficult to correct for after data collection. The advantage of using two additional detectors is made clear in figure 3.1, since by comparing the scattering of these absorbing and non-absorbing particle pairs using regions covered by PMT060 and PMT120 provide a method of confirming that an assumption of non-absorbing character is incorrect, since the simulated signals deviate significantly.

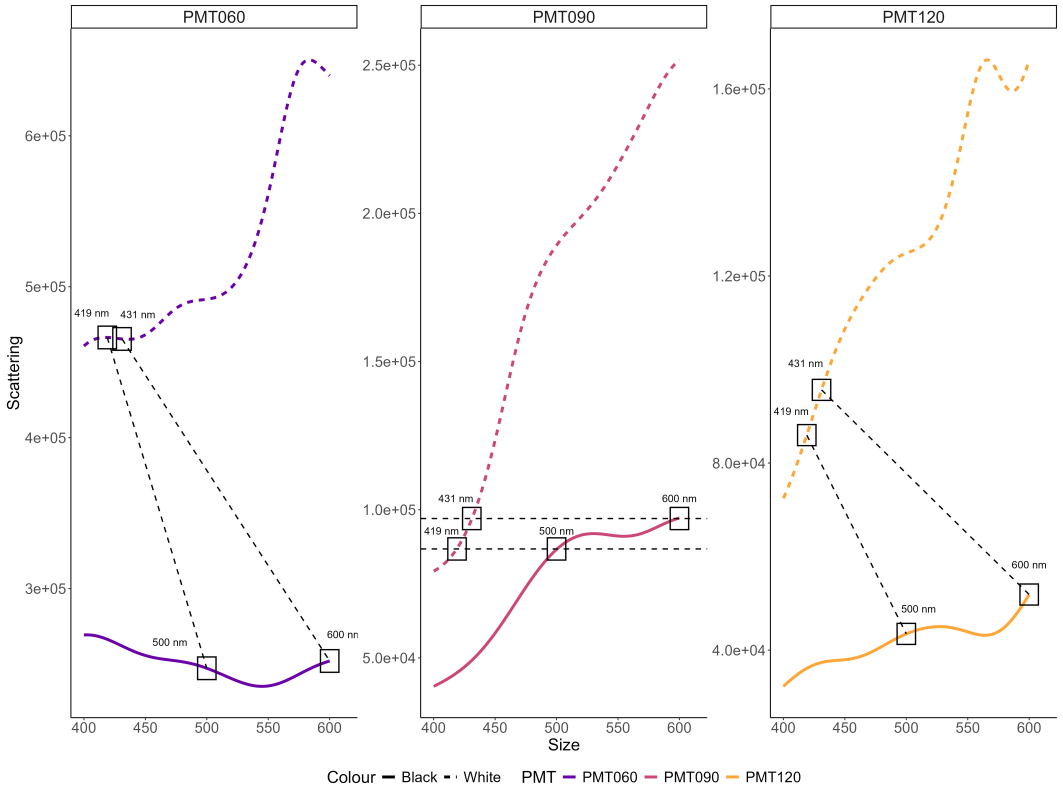

Figure 3.1: Simulated scattering within the PMT060, PMT090 and PMT120 regions for both a white (undyed) and black (dyed) PSL particle, for a range of diameters (400-600nm). For the PMT090 region, the scattering of a 500 and 600 nm black PSL particle have been highlighted, along with the diameter of white PSL particles which would produce the same magnitude of scattering within that region (419 and 431 nm, respectively). The scattering of these particles within the PMT060 and PMT120 is also highlighted to show the differentiation power of using multiple detection regions.

A significant component of Chapter Two concerned the potential of altering the MPS' detector configuration, with the goal of improving analytical capabilities. Figure 3.2 shows a quantification of the effect of changing the angle ranges of detection. The scattering expected from a range of different diameter PSL particles is shown, as well as the scattering of the same particles if the forward- and back-scattering PMTs and associated angle ranges were moved further away from 90 $^{\circ}$ to the incident beam (where PMT090 is located).

Figure 3.2 shows that there is a significant increase in scattering over most of the particle size-range, with scattering increasing by approximately 200 % for 400 nm PSL particles

and over 400 % for for 600 nm particles when PMT060 and PMT120 are moved 22 ° away from PMT090. This was the maximum angle change proposed in Chapter Two. These results are consistent with the predictions of Mie theory; that as particle size increases relative to light wavelength, forward-scattering becomes increasingly dominant. This data validates the hypothesis that capturing more low-angle scattering would increase the ability of the MPS to detect smaller particles.

Figure 3.2 also shows an overall increase in detected scattering when the back-scattering PMT is moved further from 90 °. however, this increase is far less uniform over the chosen size range of 400-600 nm PSL particles. Some regions, around 460 and 570 nm, show a sharp increase, while almost no change is seen around 520 nm. Below about 420 nm, scattering decreases when the PMT is moved further back. This suggests that while moving the forward-scattering PMT further forward may decrease the smallest particles that can be detected, moving the back-scatter PMT backwards may also increase the capability of the MPS to determine particle size, since the difference in scatterig with particle size bcomes more significant.

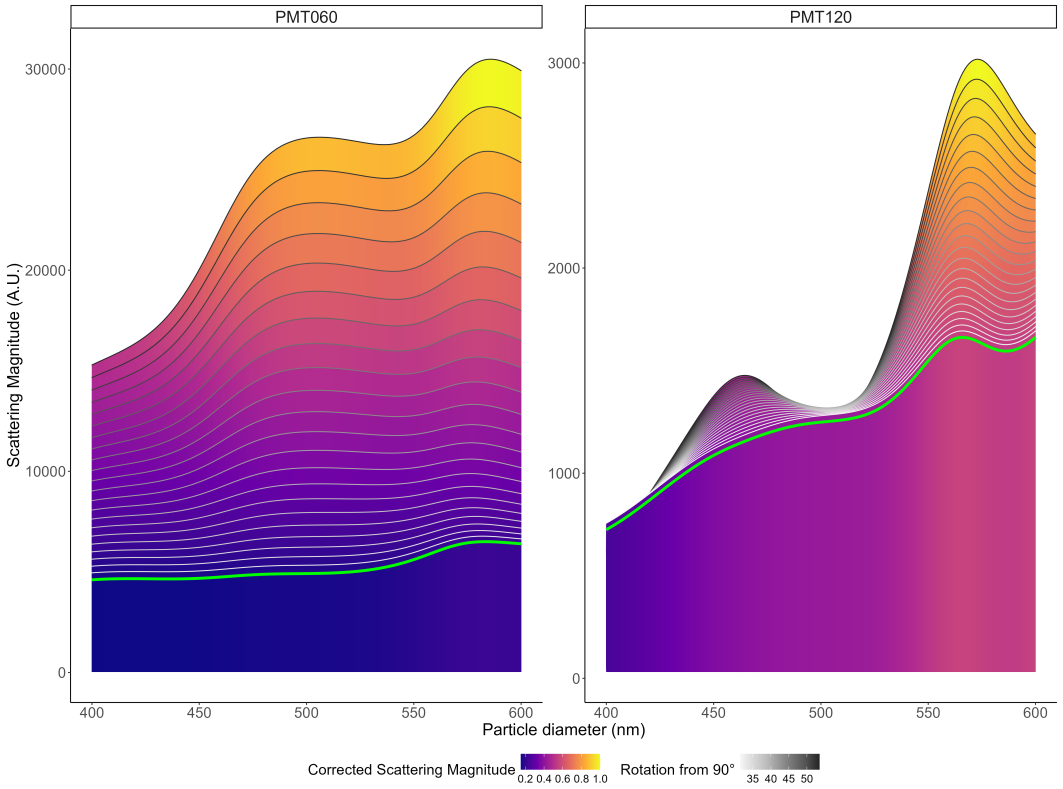

Figure 3.2: Diagram showing how changing the angle of PMT060 and PMT120 would affect the magnitude of detected scattering from white PSL particles (RI = 1.60 + 0i) between 400 and 600 nm in diameter. The green lines show the current MPS configuration, with the forward-scattering- and backward-scattering-detection regions. (31.5 ° from PMT090, which is positioned perpendicular to the incident beam). The maximum angle deviation explored shown is 53.5 °.

3.3 Performance

When testing the performance of the MPS, there are many factors to consider. These factors include resolution of scattering data, data processing, analysis and storage, air flow rate and particle concentration, and their combined effect on the rate of particle detection.

As each particle passes through the laser, the resulting scattering is detected by the PMTs and passed to the LabView software. This expresses itself as a peak in the series of discrete intensity values, as the particle enters and leaves the beam. This means that increased acquisition rate of the software increases the resolution of these peaks and thus the information

that can potentially be gained through analysis of these peaks. This increase in acquisition rate places an accompanying increased demand on the software in terms of data processing and storage. The initial solution to this was to use an acquisition rate of 0.50 MHz (recording scattering every 2 μs), and mitigate software performance issues by minimising extraneous tasks and improving software efficiency. This was an ongoing process throughout MPS development, with the software going through several iterations to improve performance and add functionality in ways which didn't impede primary functionality. These included the use of queues to hold incoming data, a structure which is used in so-called 'producer/consumer' situations, where a large amount of data is being produced by the DAQ, and consumed in the sense that it is written to a text file and subsequently discarded from memory. The queue allows these producer and consumer routines to run at different rates, so data collection is not negatively impacted once data-consumption slows down over time.

Another concern was the large amount of data produced, not primarily for storage, but for the ability to open large text files and manipulate the data contained therein. To reduce the impact of the latter issue, the peak detection functionality detailed in chapter 2 was added in parallel to the saving of all the raw, unedited PMT data. This meant that peak data could be analysed separately, reducing file size significantly; anywhere from a factor of ten to multiple thousands, depending on the frequency of detected peaks. The peak data being collated separately alongside the full data set allows for much more efficient data manipulation, since each set of peaks is recorded together, with a predictable format. The large, raw data files were retained as a backup of the data, if there was an issue with the collated peak data, or to analyse other aspects of the data such as background determination or signal analysis.

As detailed in chapter 2, built into the software was the ability to set the number of data points before and after the trigger point at the start of a particle-induced signal peak. A balance was sought between conflicting goals of not needlessly saving irrelevant data and risking capturing other peaks within the retained dataset, and ensuring that all peaks are fully captured and not cut off. It was determined that between 75 and 125 points both before and after was sufficient to fully capture peaks, since it was very uncommon for two particles to pass through the beam within that window of time (less than 500 μs) using the standard experimental setup including flow rate and particle concentration. The points saved before the peak trigger were kept the same as after, both for the sake of consistency and to retain a region with no particle scattering which could be used to obtain a background for that peak. This was the best way to find a background for each peak, since it would be immune to the distortion of longer-term fluctuations, unlike using a single background value for the entire set of peak data. While it would theoretically be possible to apply a peak detection algorithm to the raw data, and thus have a potentially more accurate background and resulting peak data, this would be impractical given the sheer size of the raw data files and the available computation resources.

3.4 Effect of Particle Size

An effective method for testing the capabilities of the MPS is through using a range of particles with the same composition, but varying sizes. This allows all parameters except size be controlled, which helps compare both experimental and simulated scattering data. In many cases, absolute scattering increases with increasing particle diameter, within the Mie scattering regime. However, this overall increase does not occur uniformly across the angular scattering profile, the profile of which changes significantly with even small changes

to particle diameter. This shift expresses itself within the predicted phase function over small, secondary peaks which migrate and change magnitude as the particle diameter is changed. Given the strict collection angle ranges, when light either reaches the sensor or does not, this fluctuation of the phase function's secondary peaks causes the magnitudes predicted to be detected by each PMT to change relative to each other. Polystyrene latex (PSL) beads were chosen as the primary aerosol particle to be analysed in the course of testing the MPS in laboratory settings. Their use in development and calibration of optical instruments is pervasive throughout classic and contemporary literature.[72–77] This is due to a number of factors, including low cost and high availability, mono-dispersity, suitability to be dyed different colours, chemical inertness, minimal health hazards and well-established optical properties (such as refractive index). This makes them easy to aquire and work with in laboratory settings, and makes simulation of their scattering under specific conditions relatively straightforward.

For experimentation, un-dyed, white PSL were acquired in a range of diameters; 200, 350, 500, 750, 1000, 2000 and 3000 nm. In addition, black-dyed PSL beads with diameters 200 and 500 nm, were bought from the same manufacturer, Polysciences Inc. (Pennsylvania, USA). Additionally, 200 and 500 nm white PSL microspheres from Alfa Aesar (now Themo Fisher Scientific, Massachusetts, USA) were also used. Table 3.1 shows the true size variation of each class of PSL bead.

Manufacturer	Code	Diameter	Minimum	Maximum	SD	Colour	CRI
PB	PB_WPSL0200	200	180	220	16	White	1.60 + 0.0i
PB	PB_WPSL0350	350	315	385	17.5	White	1.60 + 0.0i
PB	PB_WPSL0500	500	450	550	15	White	1.60 + 0.0i
PB	PB_WPSL0750	750	675	825	22.5	White	1.60 + 0.0i
PB	PB_WPSL1000	1000	900	1100	30	White	1.60 + 0.0i
PB	PB_WPSL2000	2000	1800	2200	100	White	1.60 + 0.0i
PB	PB_WPSL3000	3000	3000	3300	150	White	1.60 + 0.0i
PB	PB_BPSL0200	200	180	220	16	Black	1.60 + 0.1i
PB	PB_BPSL0500	500	450	550	15	Black	1.60 + 0.1i
AA	AA_BPSL0200	200	180	220	-	White	1.60 + 0.0i
AA	AA_BPSL0500	500	450	550	-	White	1.60 + 0.0i

Table 3.1: Physical properties of the PSL particles analysed with the MPS, as given by the manufacturer, PolyBeads (PB) and Alfa Aesar (AA). Alfa Aesar does not provide an estimation of standard deviation of particle size, so it has been assumed to be equal to the equivalent diameter PB particle where it is necessary. The minimum and maximum sizes for these particles are equal, so AA_WPSL0200 and PB_WPSL0200 can be treated as equivalent when discussing experimental and theoretical simulation data. All diameter and related distribution values are presented in nanometres.

3.4.1 Simulating scattering of PSL Particles

With the range of particles described above, it was possible to use their physical parameters to calculate their theoretical scattering cross-section and scattering phase function using the model outlined above, and therefore build a dataset of expected relative scattering to each PMT. The diameters of each particle type advertised by the manufacturers are only the mean diameter of the particles provided; a degree of polydispersity is expected, even in a nominally monodisperse sample. The manufacturer provides a range of diameter values, with all provided particles in a sample of that product expected to be within that range, along with coefficient of variance (CV) which can be used to calculate the standard deviation information is given. These size ranges are shown in table 3.1. This polydispersity is not necessarily a significant problem for particle characterisation and assessing MPS' capabilities, since it can be accounted for in simulations. It is also more realistic in terms of using laboratory tests to simulate a real-world, unknown particle environment where monodispersity is likely not expected. The other physical parameter required is the wavelength-dependant complex refractive index (CRI). This is partially provided by the manufacturer, who give a value of $\sim$ 1.59 - 1.60 for the real component of the refractive index. This presents potential issues,

since the CRI is composed of a real and imaginary component. For the 'white' or un-dyed particles, it may be sufficient to assume this imaginary component is equal to zero, given that these particles are not expected to absorb a significant portion of the light. For the dyed particles, no information is provided regarding their light absorption, but it can be expected to be significant.

Another issue is that CRI is often wavelength-dependant, and the refractive index provided is for light with a wavelength of 589nm. This is sufficiently different from the MPS beam wavelengths (405 and 445 nm) that a CRI of 1.60 + 0.00i should not be unquestionably be assumed for the un-dyed particles. Fortunately, one of the reasons PSL beads were chosen was due to their common use in published literature regarding mie scattering and OPS instruments.

Based on literature sources which report a value for CRI at 445 nm and similar wavelengths, it was assumed for white PSL that $CRI = 1.60 + 0.00i$.[61] For the dyed PSL particles, a value of $CRI = 1.60 + 0.1i$ was used for theoretical simulations, as an estimate in the absence of available literature values at the 400-450 nm wavelength for dyed PSL particles.

Using these parameters, The scattering of 445 nm light was simulated for all variants of the PSL particles. Figure 3.3 shows the generated phase functions of the white PSL particles. While there are fluctuations in the profile of the phase function at different particle diameters, it is clear that both absolute scattering and the relative bias towards forward scattering increase with increased diameter. This is the expected result according to the

principles of Mie scattering as the particle size increases beyond the Mie regime and scatters according to geometric scattering, where forward-scattering is even more dominant.

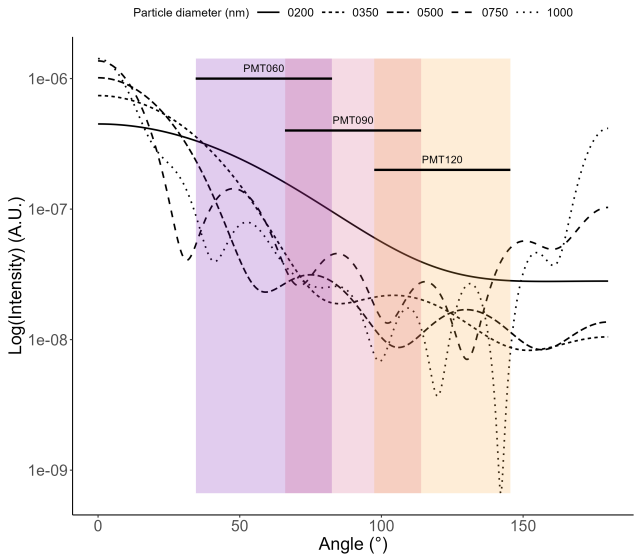

Figure 3.3: Phase functions of the white PSL particles analysed in this chapter, produced using the Mie Theory code[45] and the physical properties detailed in table 3.1. Data for 2000 and 3000 nm particles have been excluded for clarity, and since the scattering data for these particles is not presented.

The same scattering simulation data is presented in figure 3.4 in the form of the proportion of scattered light detected by PMT060, PMT090 and PMT120. This is the form which the data from the MPS will take; a collection of sets of three signals, so analysis of the relative signals between the PMTs is vital.

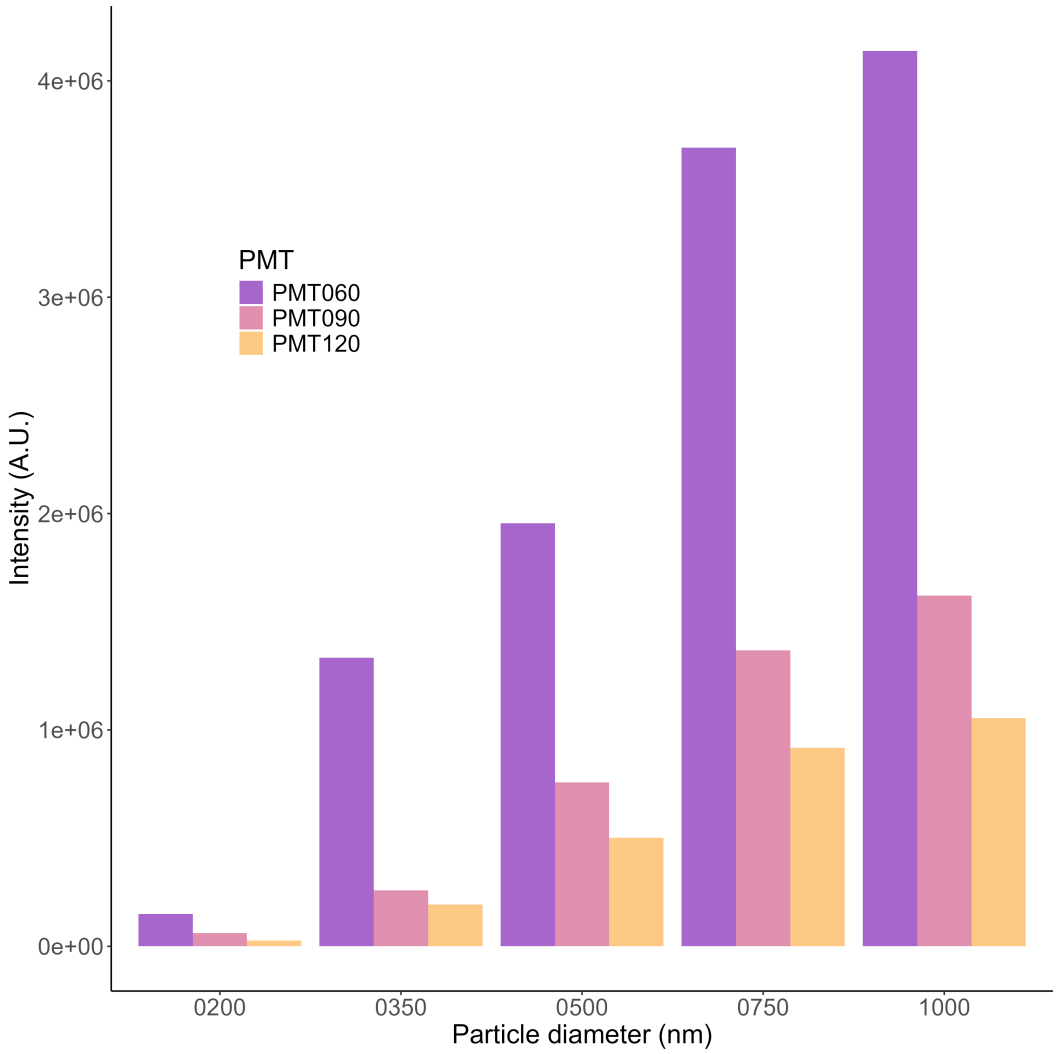

Figure 3.4: The total scattering intensities predicted to be detected by each of the MPS' PMTs, calculated using the phase function data of the white PSL particles shown in figure 3.3.

Diameter Distribution simulations

In order to account for the variation in particle size within the samples shown in table 3.1, and assess its potential to effect experimental data, scattering simulations were performed using a series of particle diameters spanning the range of particle sizes stated by the manufacturer. This provided a series of sets of three scattering values spanning the minimum to maximum diameter for that particle species, allowing an analysis of how much the signals were expected to change. However this range of values is not necessarily representative

of expected data, since the range of particle sizes within each sample is not uniform, but will follow a distribution. For this new dataset a normal distribution (with the mean and standard deviation following the data provided by the manufacture) was calculated. Using this distribution, the sets of scattering values weighted according to the probability that a single particle will have that diameter and therefore produce scattering equivalent to the simulated data.

Figure 3.5 is an illustration of how the simulated angular scattering changes with small differences in particle diameter, it shows how even small differences in diameter can produce significantly different scattering. The portion of the phase function within the collection range of the MPS' PMT060 detector is displayed for each 2 nm difference of diameter within the range provided by the manufacturer, as given in table 3.1. The shifts in the phase function are smooth, with peaks and valleys of varying intensity migrating gradually.

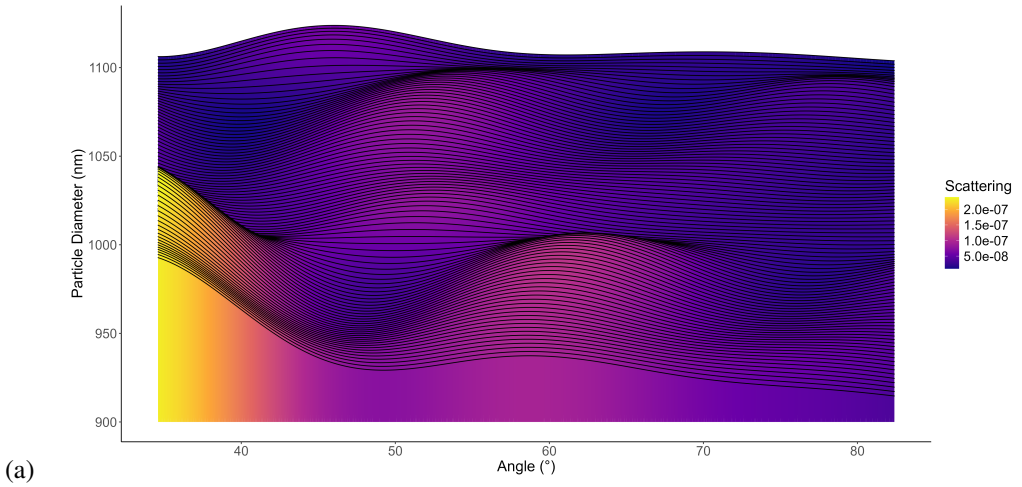

(a)

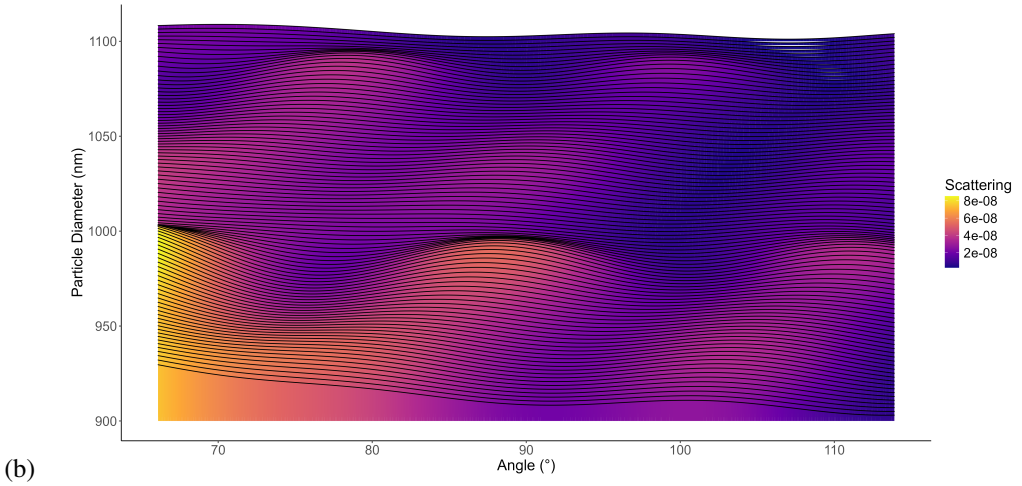

(b)

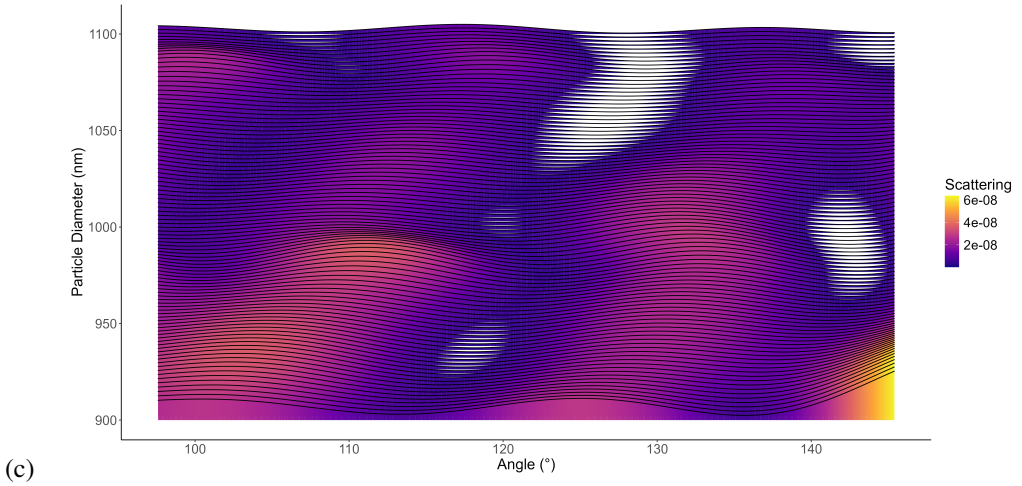

(c)

Figure 3.5: Visualisation of how the simulated phase function changes over the diameter range provided for PB_WPSL1000 (table 3.1), within the angle ranges of each PMT: (a) shows the PMT060 range, (b) the PMT090 range and (c) the PMT120 range. Each phase function is coloured according to its magnitude at that angle, the scale is arbitrary. Ridge height shows angle-specific intensity, the scale of which is unified across all plots.

While visually compelling and qualitatively informative, this figure does not necessarily provide precise insight into the exact effect on simulated MPS data, since each PMT collects all the scattering within its detection angle range as a single intensity. To represent this, figure 3.6 shows related data to that shown in figure 3.5, but the relevant regions of the phase function have been totalled as a representation of how the total detected scattering is predicted to change based on any given particle's true diameter.

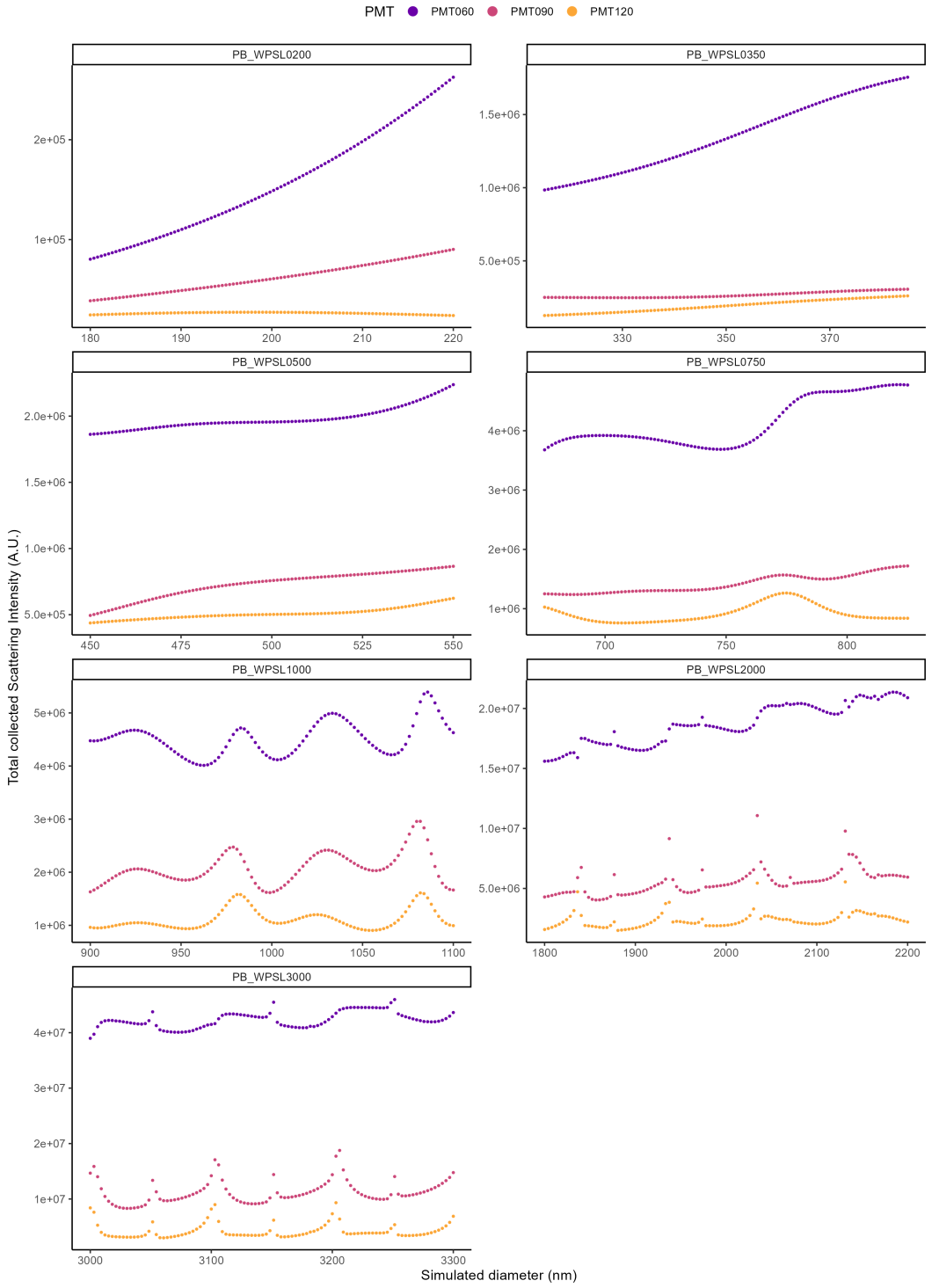

Figure 3.6: Total simulated scattering intensities of the white PSL particles using the range of sizes detailed in figure 3.1, demonstrating how the particles in the samples may produce varied scattering signals.

This data reveals both the general trend of positive a correlation between size and total scattering, as well as the increased fluctuation of the phase function (and thus PMT data) with increased particle size. From particle diameters of around 1000 nm or more, the data begins exhibiting increasingly sharp spikes, which are a phenomenon known as Mie resonance. It also demonstrates the extent to which variation in scattering is to be expected in the experimental data, purely as a result of the range of particle diameters within each sample.

3.4.2 Experimental Data

Evaluating Data Processing Options

PSL particles were nebulised, dried and analysed using the MPS, and their scattering data was collected and analysed.

Using this peak data, the scattering peaks were analysed to calculate values for peak maximum, width and area, with respect to signal background. The suitability of peak maximum (amplitude) as opposed to peak area was evaluated, given its negligible computational requirements, which would be beneficial due to the large number of peaks to be analysed for current and future datasets. Peak area is also susceptible to distortion if the particles are not in the beam for a consistent duration. Analysis of the peak width reveals significant variation, which would imply differences in the duration that particles are travelling through the beam

Run ID	Particles Detected	Run Duration (s)	Particle Frequency (s^{-1})
AA_WPSL0200	22276	61.7	361.0
PB_WPSL0350	52139	90.8	574.2
PB_WPSL0500	11966	159.2	75.2
PB_WPSL0750	15008	74.2	202.3
PB_WPSL1000	12640	91.8	137.7
PB_WPSL2000	2156	182.7	11.8
PB_WPSL3000	1066	171.1	6.2

Table 3.2: Statistical data regarding the MPS data collection sessions, the data for which is presented in this chapter.

area. Based on the width MPS signal peaks, the average particle spends approximately 50 µs in the beam, with some peaks lasting for as long as 100 µs. This is likely due to two primary factors. Either there is variation in particle speed, or variation in the trajectory of the particles in relation to the beam, since moving across the full diameter of the beam will result in a longer scattering duration than a path which results in a glancing hit (assuming equal particle speed). With this in mind, it was determined that for the duration of laboratory work, peak maximum would be used for analysis. There is precedence for doing this in the analysis of OPS instrument data, for example in the work of Njalsson and Novosselov (2018), where scattering pulse amplitude was examined.[78]

Given the calculated particle frequency presented in table 3.2, there is a significant probability that two particles will intersect the beam within the same 300 µs capture window; as high as 16 % for PB_WPSL0350. This was accounted for during data processing, preventing it from affecting results. The probability of two particles' signals overlapping is only 0.5 %, so it is not expected to have a significant effect on the results. At a particle frequency of 1024 particles per second, the overlap chance would be 1 %.

Data Visualisation

Using peak maximum as the metric to evaluate individual scattering signals, the next stage in data investigation revolves around how to visualise the data to best understand the observed scattering data. Treating scattering data from all particles in a sample originating from a single PMT (e.g. PMT060) as an isolated data set - which represents how a standard single-detector OPS instrument would produce data - allows it to be treated as a one variable

continuous dataset. This makes a histogram an ideal visualisation technique for this data; histograms of the different experimental data are presented in figure 3.7.

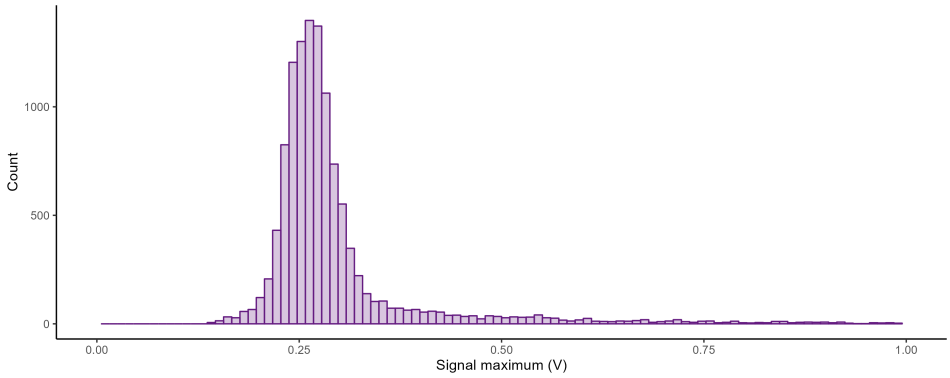

Figure 3.7: Histogram of the scattering signal peaks detected by PMT060 for a sample of particles of the PB_WPSL0500 species.

This data representation is useful for assessing the variation in scattering of a body of particles, and the difference in the distribution of different groups of particles. Using Mie theory, the scattering can be used to determine - or in this case validate - the diameter of the PSL particles, since the CRI is known. Figure 3.8 shows the PMT060 scattering signals from different PSL particle sizes analysed. The there is a significant difference in the distribution of signal intensities, an explanation for this is presented later in this chapter.

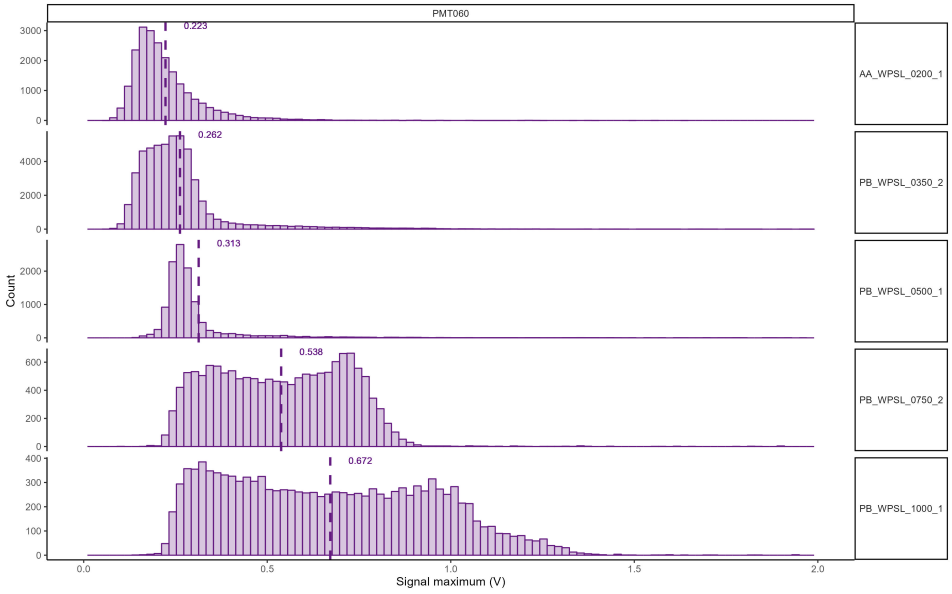

Figure 3.8: Histograms of the scattering signal peak maximums for a range sample of particles, including the data presented in figure 3.7 - AA_WPSL0200, PB_WPSL0350, PB_WPSL0500, PB_WPSL0750 and PB_WPSL1000. It shows the difference in scattering detected by the front-scattering PMT, depending on particle diameter.

However, this data is, in isolation, no more useful than that produced by established OPS instrumentation. Incorporating the data from all three PMTs allows for more nuanced analysis, since each particle produces three scattering signals. Figure 3.9 uses the same datasets as previous figure 3.8, but also includes the data from PMT090 and PMT120, in addition to PMT060.

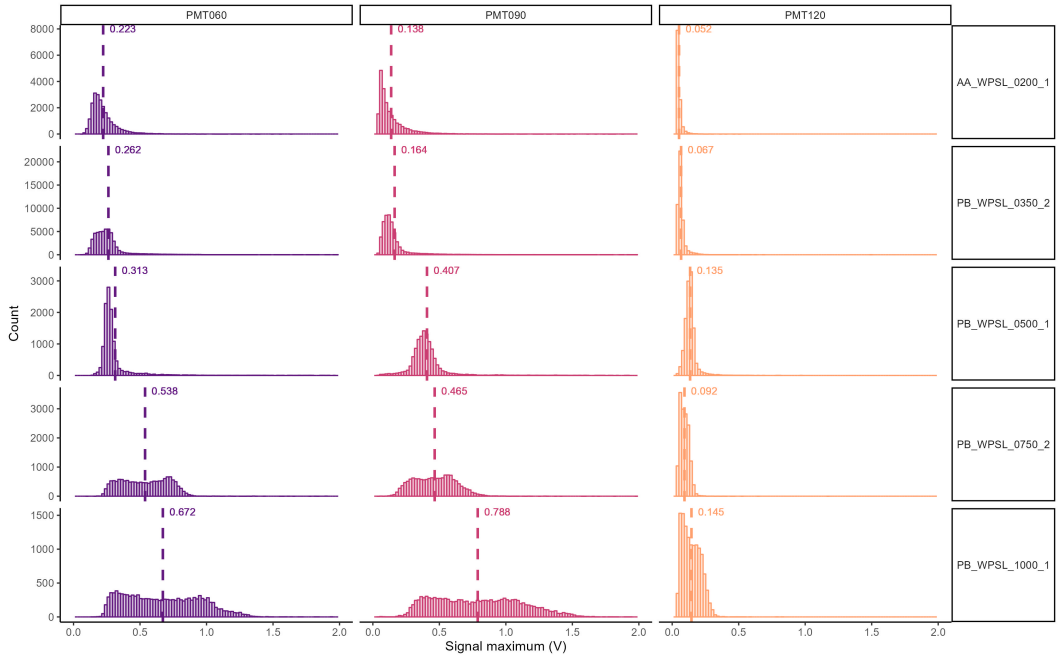

Figure 3.9: Histograms of the scattering signal peak maximums (the same as figure 3.8, but now including data from all three PMTs) for a range sample of particles; AA_WPSL0200, PB_WPSL0350, PB_WPSL0500, PB_WPSL0750 and PB_WPSL1000.

Using this additional data, there is more information available to differentiate signals; each group of analysed particles have produced a set of three distributions with mean values that distinguish them from the other groups. This is not the limit of the extra information provided, since these three distributions of scattering are made up of sets of scattering intensities which originate from individual particles, thus these distributions themselves can be inter-compared to illustrate an even more sophisticated picture of the scattering behaviour of the particle set.

Figure 3.10 shows an example of this inter-comparison, where the signals produced by each particle are plotted as co-ordinates using the three PMT detectors, using data collcted from PB_WPSL0500.

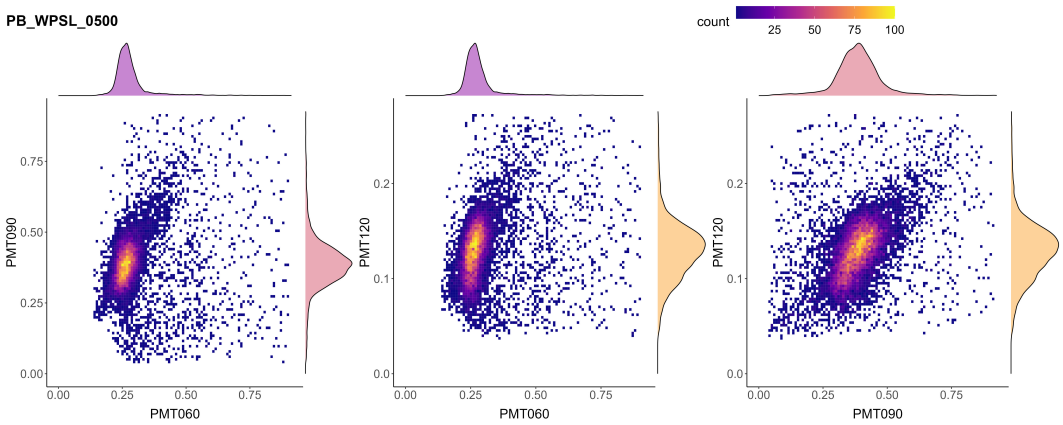

Figure 3.10: Density plots using pairs of PMT scattering signals from individual particles as coordinates for an analysed sample of PB_WPSL0500.

Since there are three PMTs, there are also three pairs of PMTs that can be used to create a unique plot. It would be possible to create a single 3-dimensional plot incorporating all three PMT signals, but this is not necessarily superior in terms of clear data visualisation. By presenting the data in this way, the relationship between light scattering at different angles is given additional clarity. Each particle species produces a distinct pattern indicating the variation of scattering signals produced, which is potentially caused by the known variation in diameter within the samples.

Comparison of Experimental and Theoretically-derived Simulation Data

Using this visualisation method, the other different diameter white PSL samples are presented in figures 3.9.

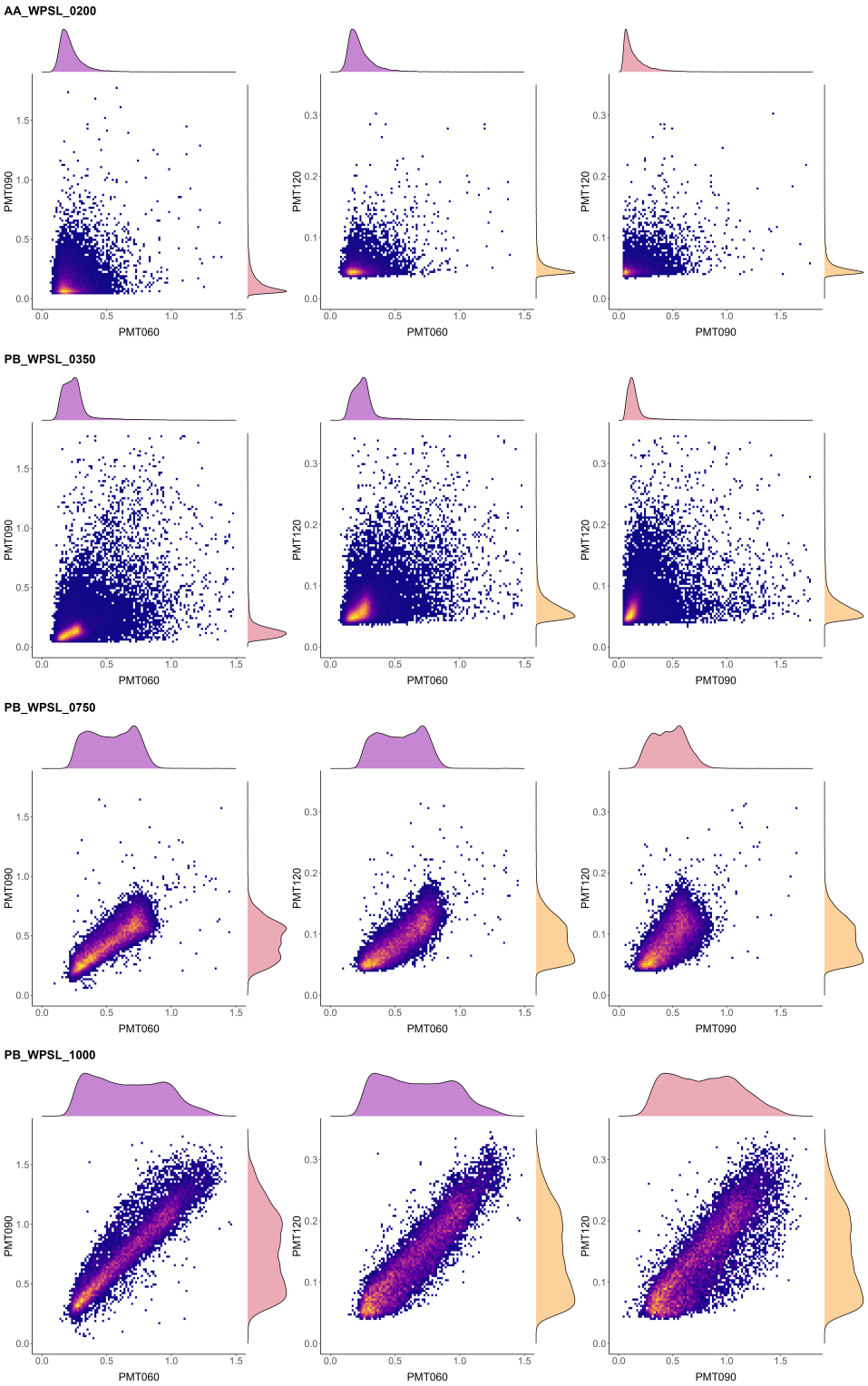

Figure 3.11: 2-dimensional scattering intensity heat-maps with aligned density plots for AA_WPSL0200, PB_WPSL0350, PB_WPSL0750 and PB_WPSL1000.

Notably, in addition to each particle size producing a different signal pattern, there is an identifiable trend of positive signal correlation between the recorded scattering intensities for each particle by the different PMTs. This is a good indication that the variation in scattering between relatively uniform particles is being caused by the diameter variation which is known to exist, rather than an external factor such as signal noise.

Looking at the progression of data from 200 nm to 1000 nm PSL particles, there are notable patterns in terms of scattering signal distribution. AA_WPSL0200, PB_WPSL0350 and PB_WPSL0500 all show a consistently unimodal distribution in the PMT060 and PMT090 ranges, whereas PB_WPSL0750 and PB_WPSL1000 show a bimodal distribution and a significantly broader spread in scattering intensities than the smaller particle classes. Data for PB_WPSL2000 and PB_WPSL3000, are not presented, since particle detection was significantly lower than for the smaller particle sizes (table 3.2), and the few signals successfully detected did not follow any identifiable pattern. These signals were likely due to contaminate particles in the air flow, and that the larger PSL particles are either not being successfully nebulised, or otherwise lost to collision with the interior of the tubing connecting the PAGS and MPS nozzle (or within the nozzle itself). The bimodal scattering patterns are, at least upon initial evaluation, an unexpected phenomenon. Although the PSL samples were expected to all have a unimodal size distribution, that does not necessarily translate to a unimodal distribution of scattering, due to the complexity and variation of Mie scattering (evidenced in figures 3.5 and 3.4).

It appears from the data presented in figures 3.12, 3.13 and 3.14 that for AA_WPSL0200, PB_WPSL0350 and PB_WPSL0500, the simulated scattering would present as unimodal,

which does not seem to be the case for PB_WPSL0750, where there are two distinct regions where the scattering signals of each size congregate. PB_WPSL1000 presents an increasingly convoluted pattern, as the phase function of the particles become increasingly complicated.

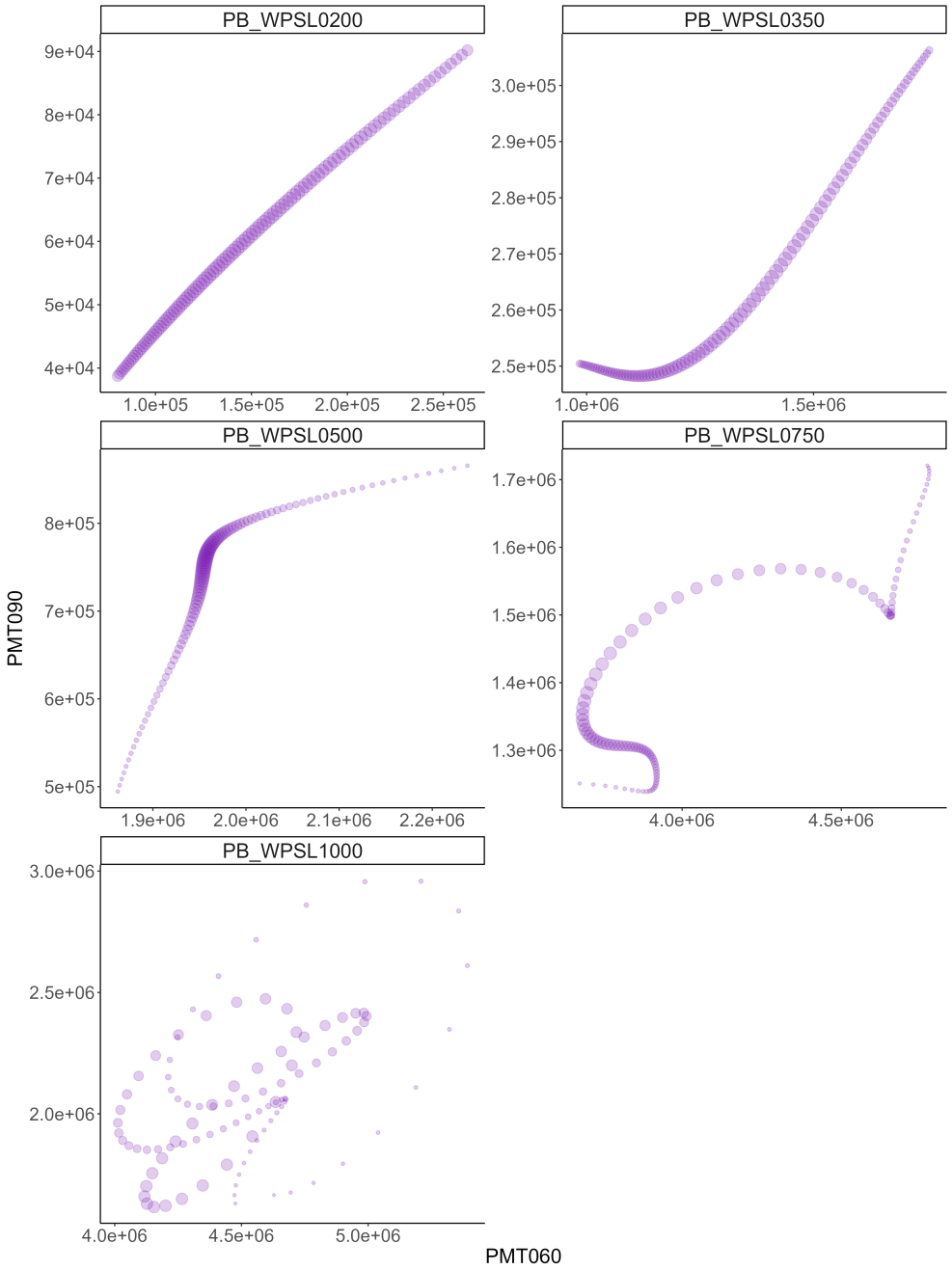

Figure 3.12: Theoretical scattering data using the ranges of size distribution for the PSL particles 200 to 1000 nm, as described in figure 3.4 and table 3.1. These particle data have been plotted using PMT060 vs PMT090 to match how the experimental data has been presented in figures 3.10 and 3.11. To represent the distribution of particle size, each point has been scaled relative to its probability for a random particle in the sample.

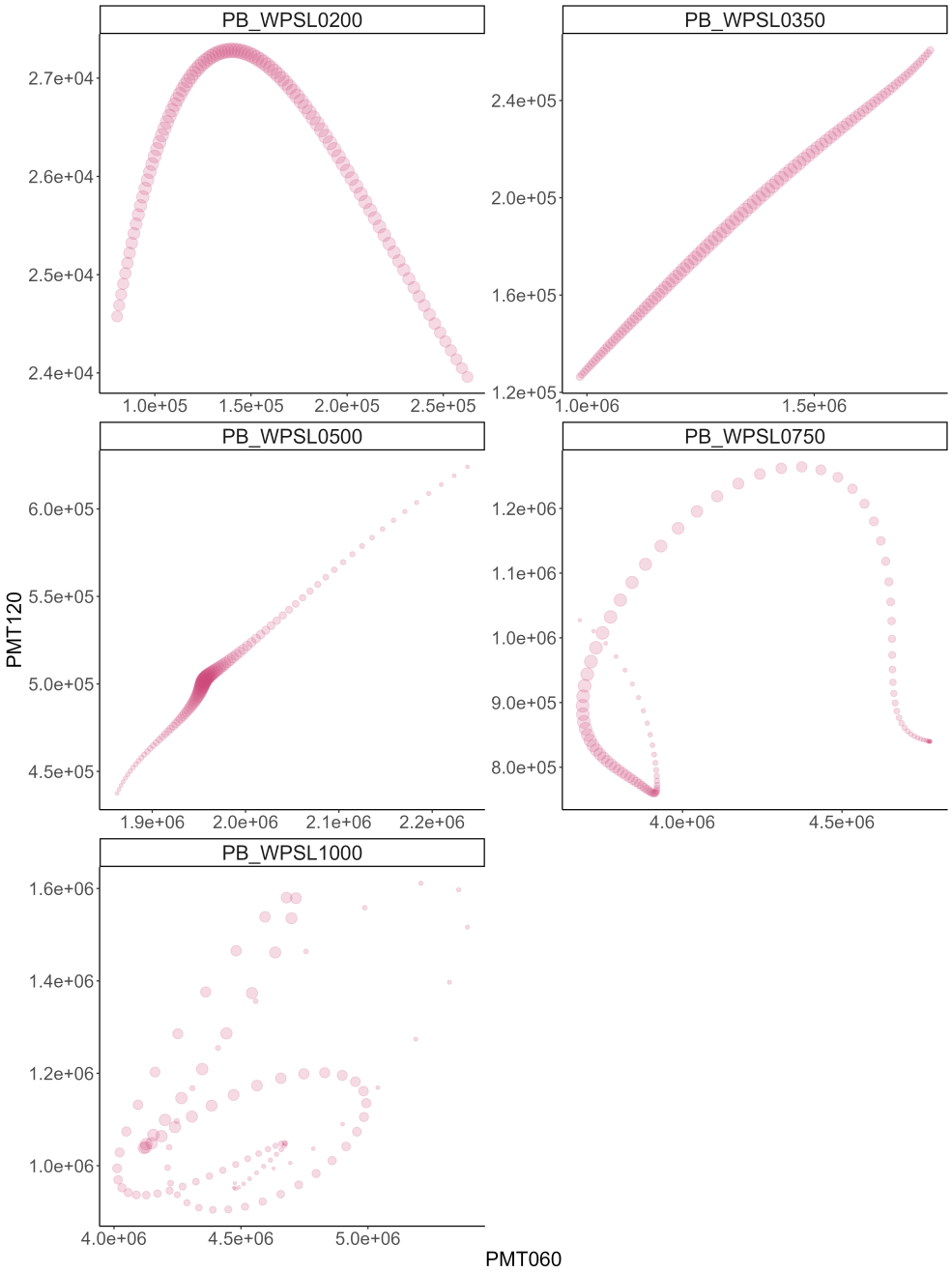

Figure 3.13: Theoretical scattering data using the ranges of size distribution for the PSL particles 200 to 1000 nm, as described in figure 3.4 and table 3.1. These particle data have been plotted using PMT060 vs PMT120 to match how the experimental data has been presented in figures 3.10 and 3.11. To represent the distribution of particle size, each point has been scaled relative to its probability for a random particle in the sample.

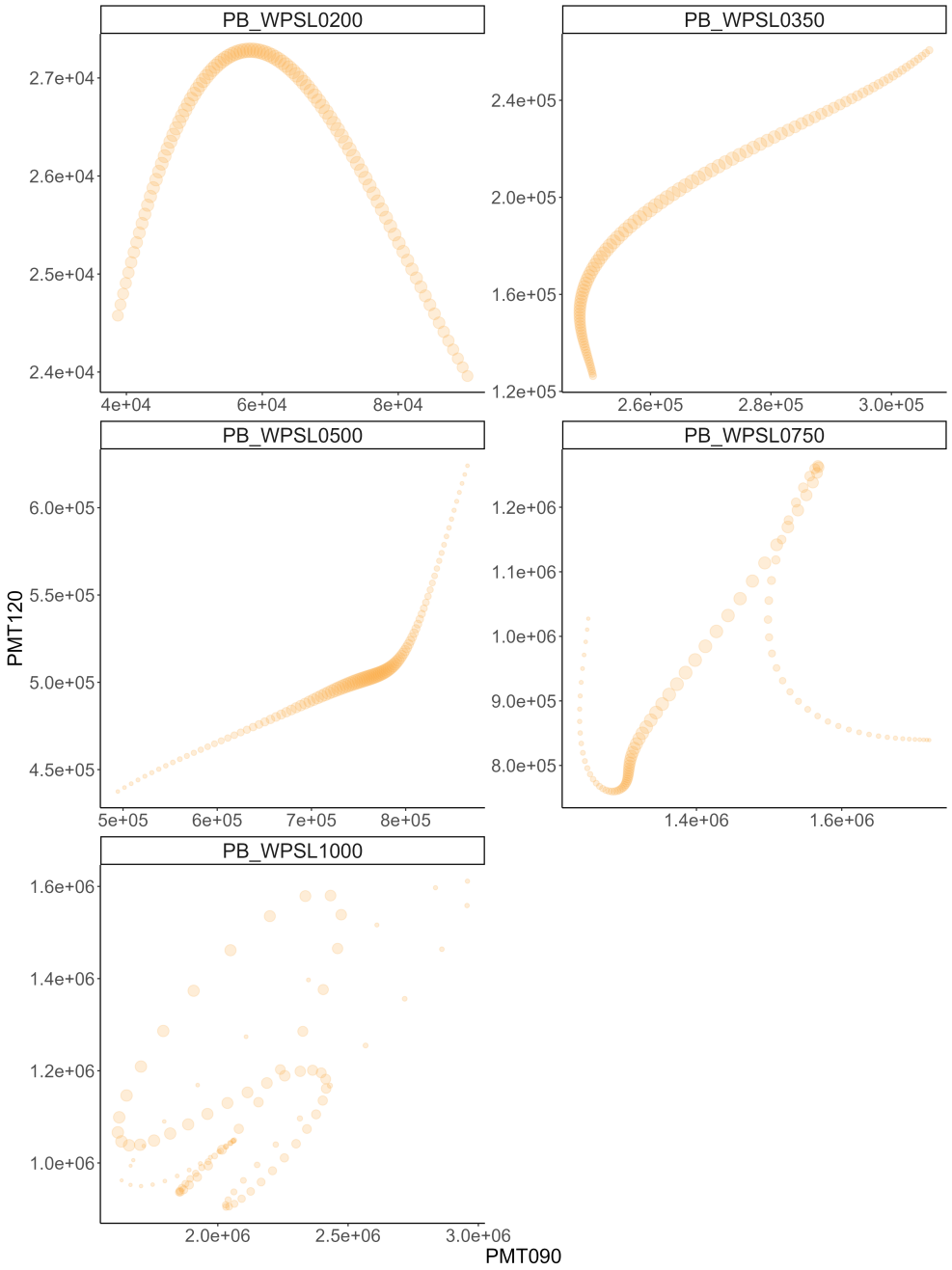

Figure 3.14: Theoretical scattering data using the ranges of size distribution for the PSL particles 200 to 1000 nm, as described in figure 3.4 and table 3.1. These particle data have been plotted using PMT090 vs PMT120 to match how the experimental data has been presented in figures 3.10 and 3.11. To represent the distribution of particle size, each point has been scaled relative to its probability for a random particle in the sample.

It is, however, perhaps unclear in the 2-dimensional representation of figures 3.12, 3.13 and 3.14, exactly how this data translates to the form the experimental data may actually take. To overcome this the resulting scattering for each particle size range and PMT were sorted into ten equal bins, multiplied by the probability of that particles in the sample being that size, and totalled in an attempt to qualitatively represent how the distribution of the experimental dataset would be expected to present. This visualisation is presented in figure 3.15.

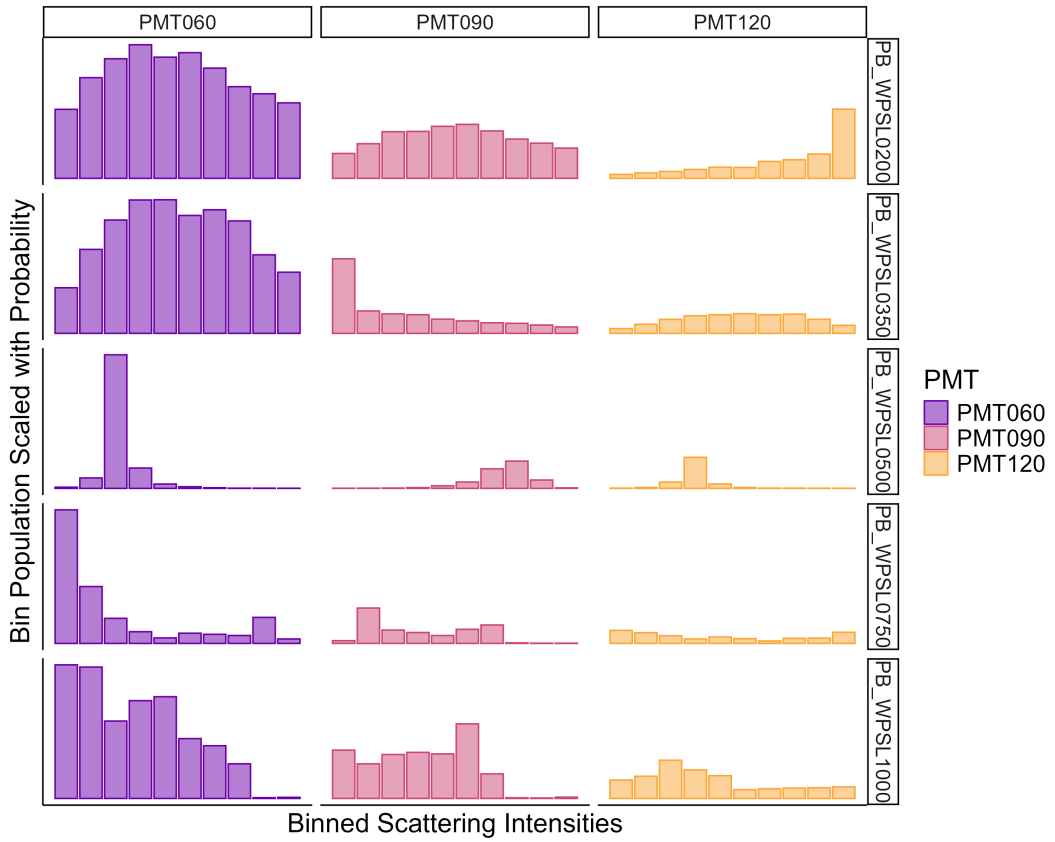

Figure 3.15: Data from figures 3.12, 3.13 and 3.14, collated into 10 equal width bins according to scattering intensity and totalled after being multiplied by their corresponding probability, in order to approximate the expected profile of a histogram formed from experimental scattering of a particle set with that distribution. Plots are presented qualitatively in accordance with their intended function; both axis scales are arbitrary and the scales of the binned scattering intensities are different for each particle class

The significance of this as a match for the experimental data is most acute with the similarity between the predicted and actual scattering distributions for PB_WPSL0750; not only does it predict a bimodal distribution, abut also correctly represents the approximate weighting

between the two peaks. PB_WPSL0500 also shows strong agreement in terms of he shape of its distribution, lending further validation to the ability of the the simulated data to predict the nature of the experimental scattering based on particle population properties.

The relationship between mean scattering of the different size particles from experimental data and theoretical simulations is presented in figure 3.16.

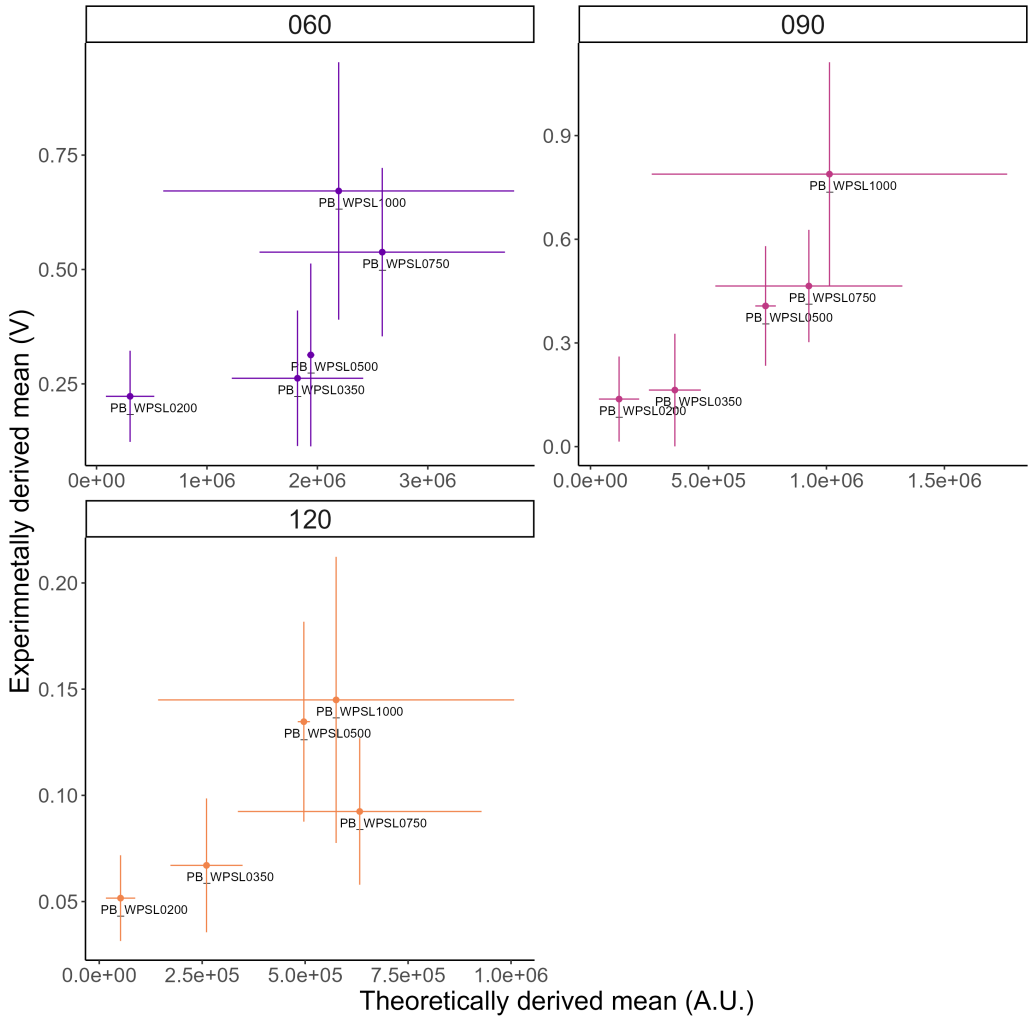

Figure 3.16: Mean scattering of each PSL particle size, from experimental data and theoretical simulations, plotted against each other, using standard deviation to show uncertainly.

This plot, combined with the above-described visual similarities, demonstrate that while the MPS is capable of detecting and evaluating particles, there is significant variation within the data sets. The uncertainty within the data - both experimental and theoretical - throws the current resolution of the instrument into doubt. However, it is possible that the representation of the relationship is being distorted by the bimodal distributions of the 750 and 1000 nm PSL particle classes. Looking at the smaller particle classes (200, 350 and 500 nm), there is a reasonably linear relationship between the experimental and theoretical data.

Figure 3.16 shows that while there is a positive correlation between the experimental and theoretical data, the uncertainty introduced by the size range of the test particles, and the wide range of scattering intensities, currently precludes definitive and accurate particle sizing. Further experimentation would be required, with potential avenues to reduce this uncertainty being to either source more monodisperse test particles, or filter the existing samples by diameter to achieve a more uniform sample of particles.

3.5 Mixed Particle Samples

So far all presented samples have been made up of a single type of particle, where all particles are expected to exhibit the same scattering behaviour, with allowance of variation due to factors discussed above. However, this is potentially unrepresentative of field test scenarios, where it is unlikely that any sampled air will contain only one type of aerosol particles. It is an important component of assessing the performance of the MPS to evaulate how well a mixed sample of particle signals can be identified as such, and whether these signals can be accurately sorted according to their likely source.

This analysis could be done theoretically, using 2 or more of the discussed single-type samples described above, and estimating how effectively the signals could be separated if they had been recorded during a single run. However, a more robust method would be to mix the particles as a suspension then nebulise and analyse the resulting dataset. This has been done with two pairs of different particle types.

3.5.1 Mixed Size Sample

The first mixed sample analysed was a 1:1 (by suspension volume) mixture of white PSL particles of different diameters. The particle sizes chosen were 350 and 500 nm, since both particle sets gave good scattering results, and produced similar signals. This was done to test the limits of the MPS size resolution given the available particle sizes, with a difference in mean size of only 150 nm. In an ideal scenario or in future experimentation, particle mixtures even closer in diameter would be analysed to further test the MPS' resolution.

Evaluating the single particle species sample data for PB_WPSL0350 and PB_WPSL0500 in figure 3.17, the mean signal detected using PMT060 are very similar, although there is a greater spread of signals for PB_WPSL0350. In contrast, the mean signals detected by PMT090 and PMT120 are different for these samples, with PB_WPSL0500 producing greater scattering in these detection regions. This relationship means that this pair of particle classes is an ideal candidate to demonstrate the capabilities of the MPS, since the two classes are not distinguishable using only the forward-scattering collection range.

A suspension with a 1:1 ratio of PB_WPSL0350 and PB_WPSL0500 was prepared and analysed using the MPS. A 2-dimensional plot of the peaks collected is shown in figure 3.17,

and demonstrates how using a multi-detector approach allows the two different scattering patterns to be visible.

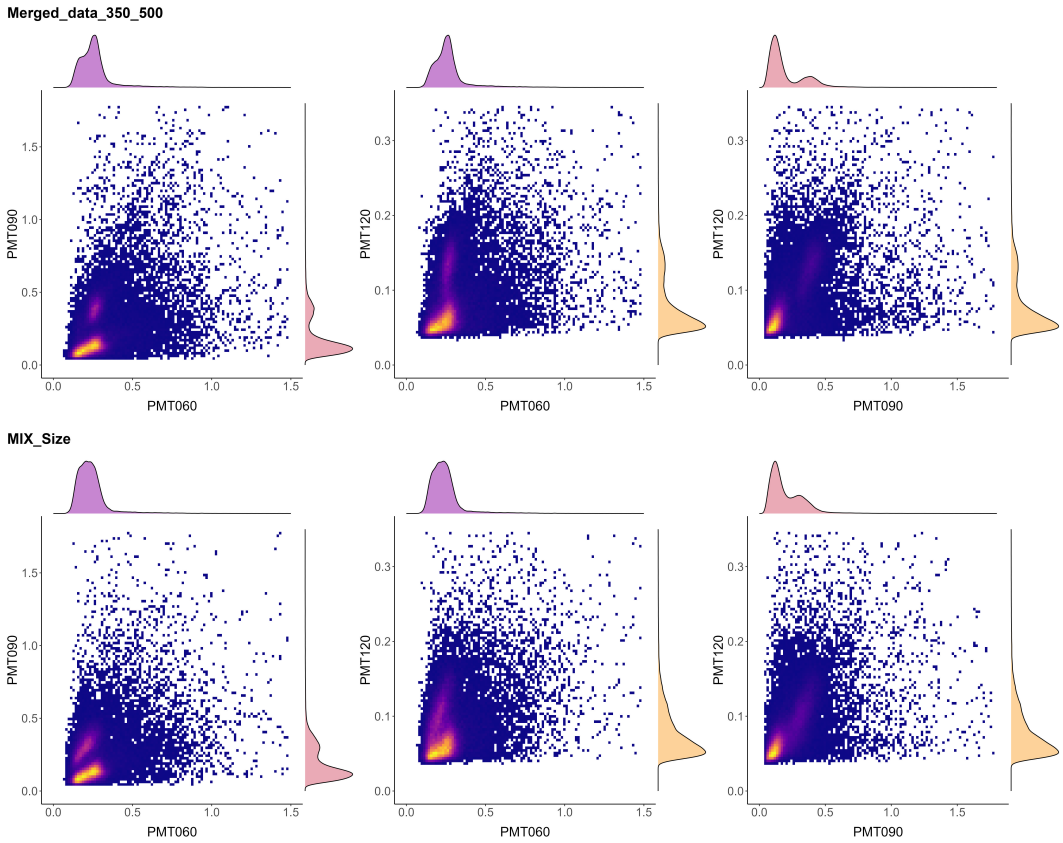

Figure 3.17: 2-dimensional scattering intensity heat-maps with aligned density plots for a merged dataset of PB_WPSL0350, PB_WPSL0500 (from figures 3.11 and 3.10, respectively) and a combined mixture (1:1) of 350 nm and 500 nm WPSL particles.

As expected, the signals detected using PMT060 appear unimodal, but cross-analysing these signals by each particles' PMT090/120 ratio of signals reveals two overlapping but distinguishable regions.

Using these bimodal signal patterns at PMT090/120, the signals can be split into two groups, each belonging to one of the particle types; either PB_WPSL0350 or PB_WPSL0500 based on the single particle class data. This reveals that there were more signals identified as being produced by the scattering of PB_WPSL0350 particles than PB_WPSL0500, in

spite of the initial mixture being a 1:1 mixture. There are multiple possible reasons for this, including that smaller PSL particles being nebulised more easily, or that the larger particles have conglomerated or settled out of suspension more during storage, an expected occurrence over the limited shelf-life of the samples. This hypothesis is bolstered by the significantly higher particle frequency shown by PB_WPSL0350 than by PB_WPSL0500 during their individual run (as seen in table 3.2). It could also be that while the particles are nebulised in equal amounts, more of the larger PB_WPSL0500 are lost within the air flow tubing that precedes the MPS chamber, via collision or electrostatic attraction (in spite of the efforts to prevent this described in chapter two) with the tube walls. This is likely the same mechanism (or combination of mechanisms) through which the larger samples, namely PB_WPSL2000 and PB_WPSL3000, produce far fewer scattering signals (which themselves are of dubious origin) over the same time period as the smaller particle classes.

3.5.2 Mixed Absorption Sample

With it established that the MPS could be used to better distinguish between particles of different size, its ability to do the same for particle types based on absorbing component. To this end a 1:1 mixture suspension of PB_WPSL0500 and PB_BPSL0500 was analysed in the same way as above.

To predict the results of this combined-sample run, the single-class results from figure 3.18 were evaluated. The scattering exhibited by PB_WPSL0500 and PB_BPSL0500 are far more similar than the previous pair, with no major deviations within any of the three PMT regions. The mean scattering signal means and standard deviations of PB_WPSL0500 and PB_BPSL0500 are presented in figure 3.18.

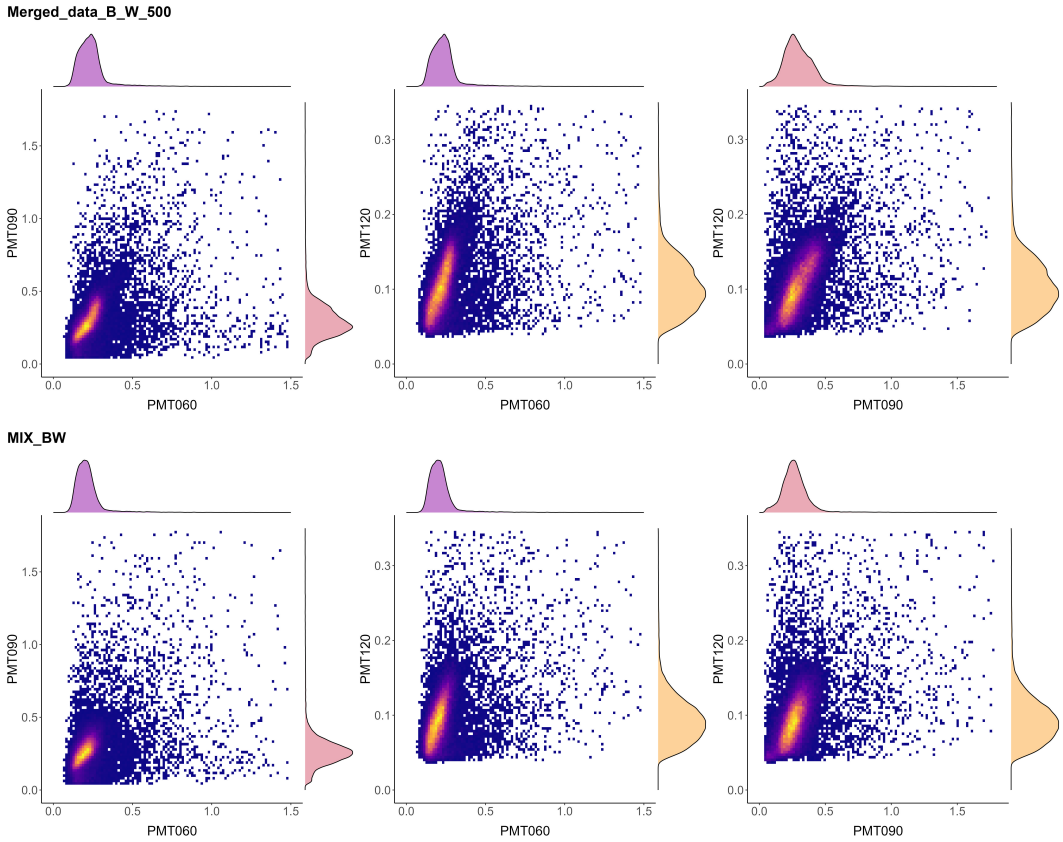

Figure 3.18: 2-dimensional scattering intensity heat-maps with aligned density plots for a merged dataset of PB_BPSL0500 and PB_WPSL0500 and a combined mixture (1:1) of 500 nm BPSL and WPSL particles.

This data shows there is not a defined difference in observed scattering behavior when the PSL particles are dyed black, using the MPS in its current configuration. This may be due to incomplete penetration of the dye into the body of the particle. Incomplete penetration would result in a light-absorbing surface and non-absorbing core. This would likely result in a scattering signal not as distinct from an un-dyed particle as expected from a fully dyed sphere. While this could be verified using the theoretical simulation, which can account for core-shell particles such as this, the extend of dye penetration cannot be determined.

3.5.3 Principal Component Analysis

Principal component analysis (PCA) is an analytical technique that reduces a multidimensional data set based on the calculation of unit vectors (principal components) within the data that account for the most variance. Using a version of the coordinate data re-calibrated about the origin, a line of best fit is calculated that preserves the maximum amount of information regarding the spread of the data across all variables. With this vector defined as the first principal component (PC1), a second principal component (PC2) is defined, maximising variance orthogonal to PC1 (it does not contain information preserved within PC1). For an n-dimensional dataset, n PCs are defined, with PC1 accounting for most of the variation, and PC_n accounting for the least. With these PCs calculated, an n-dimensional dataset can be displayed along only two axes (PC1 and PC2) while preserving as much variation within the data as possible. This is a suitable method for displaying the three-dimensional data produced by the MPS, and an alternative to either the three sets of plots (PMT060 by PMT090, PMT060 by PMT120 and PMT090 by PMT120), or a full three-dimensional coordinate plot. It would also remain suitable of the MPS were ever modified to collect additional scattering data with additional detectors.

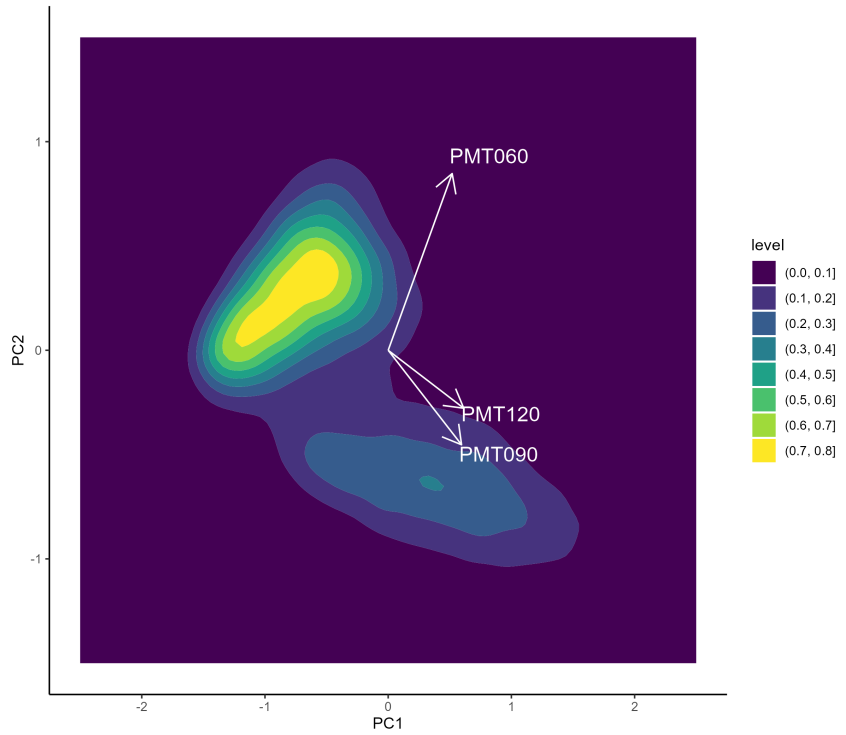

Figure 3.19: Heat-map showing the results of PCA analysis on the mixed-size PSL data. Maximal variance within the three-dimensional dataset is preserved by using PC1 and PC2. Vectors showing the contribution of each PMT's data to the variance within PC1 and PC2 are shown in white.

PCA was performed on the mixed-size PSL sample. The data is displayed along the first two principal axes in figure 3.19. The two regions representing the scattering of the 350 nm and 500 nm diameter PSl particles can be seen as distinct. This representation looks visually similar to previous plots including figure 3.17, but rather than being limited to observing the variation across only pairs of PMTs (for example; PMT060 and PMT090, only), this plot includes the variation within the data from all PMTs to the maximum degree possible in two dimensions.

PCA can quantify the contribtiuon to overall variation of each principal component. For this mixed size PSL scattering data, PC1 accounts for 64.0% of variance, PC2 for 22.2% and PC3 for 13.8%. Consequently, the plot in figure 3.19 contains 86.2% of the total data variance.

The calculated PC1 has approximately equal weighting from all three PMTs, as seen by the horizontal magnitude of the labelled vectors on figure 3.19. An interpretation of this is that PC1 represents an overall trend of increased scattering across all variables as particle size increases. PC2, however, shows that the variance within the data from PMT060 is opposed to that of PMT120 and PMT090. This is the axis of variance which accounts for the majority of separation between the types of particle, which can be seen visually in figure 3.19, where the two clusters of signals are separated clearly along PC2. This suggests that comparison using PMT060 and PMT090 reveals the most distinction between the clusters of signals, and therefore the particles. This is because PMT060 and PMT090 scattering data contribute more to this contrast component; PC2. With more sets of mixed-particle data, it would be possible to confirm if that is consistent across more cases. It indicates that while PMT120 scattering data is contributing to distinguishing between the signal clusters, its impact is less than that of the other PMTs. This aligns with other observations, including the PMT060 by PMT090 plot in figure 3.17 showing the greatest degree of separation between the clusters, as well as the generally low signal intensities captured by PMT120, which were less distinct from noise than the other PMTs. However, it does indicate that while the PMT120 signals are less distinct, the addition of a third PMT adds additonal discriminatory power to the PMT. PCA would also be able to determine if another PMT added in the future, whether it was substantively adding the to the MPS' analytical capacity.

3.5.4 Analysis using DBSCAN

The PCA analysis demonstrates the MPS' capability to qualitatively discriminate between scattering of two or more particle types. For the MPS to be a more value analytical tool, the ability to quantify the number of each particle types that are present in the sample data

would be desirable. To achieve this, a data clustering algorithm known as Density-Based Spatial Clustering of Applications with Noise (DBSCAN) was utilized to quantify the proportion of particle signals. Other commonly used clustering methods were considered, including k-means clustering, but only DBSCAN was found capable of grouping the data appropriately. DBSCAN identifies points as belonging to a cluster if they have enough other points within a certain proximity. The number of proximal points and radius are determined manually, but DBSCAN does not require a dictated number of clusters to search for. This is in contrast to k-means clustering, which requires the desired number of clusters as an input.

Performing DBSCAN on the mixed-size particle sample data, 70.33 % of the 58,025 signals were grouped into a cluster. The cluster corresponding to the WSPL0500 data contained 17.38 % of the clustered signals, and the cluster matching the WSPL0350 data contained 52.95 %. This data indicates that approximately three quarters of the PSL particles passing through the MPS chamber were WSPL0350, and only one quarter were WSPL0500. This clustering data has been overlaid onto both the PCA data and the raw scattering data, in figures 3.20 and 3.21, respectively. This is a significant deviation from the intended 1:1 sample mixture. Possible reasons for this include increased clumping or sedimentation of the initial WSPL0500 suspension, or increased losses of the larger PSL particles after nebulisation. It is also possible that the clustering percentages from DBSCAN analysis are inaccurate, but the higher proportion of 350 nm signals matches the calculated signals per second shown in table 3.2. It must be noted, however, that the particle detection frequency shown in table 3.2 would predict the 350 nm particles dominating the signal distribution even more than estimated by DBSCAN analysis.

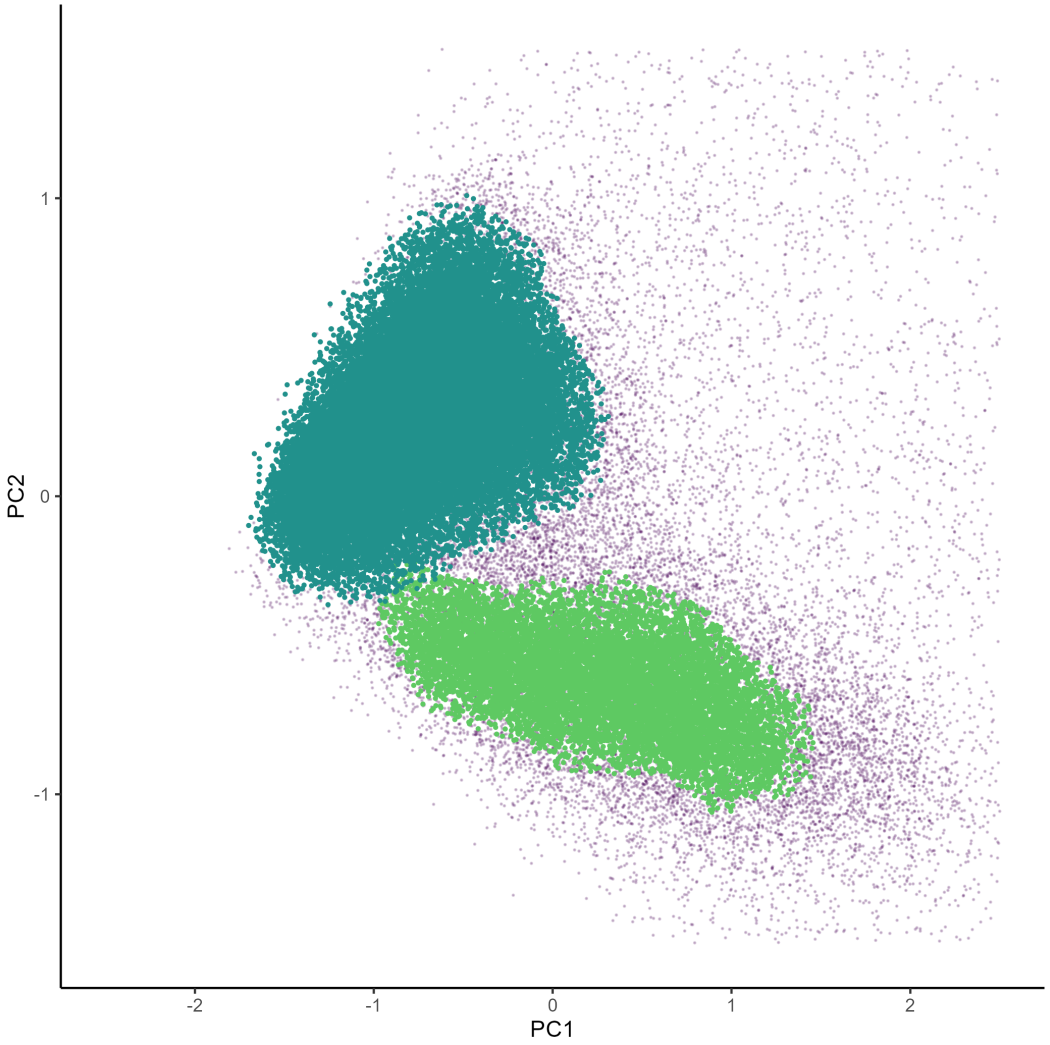

Figure 3.20: Scatter plot showing PCA analysis results of the 350 nm and 500 nm PSL mixed-particle sample data, with the DBSCAN clustering results coloured by cluster. Teal shows the cluster associated with 350 nm PSL particles, made up of 30724 signal groups (52.95 %). Green shows the cluster associated with 500 nm PSL particles, made up of 10085 signal groups (17.38 %). The 17217 signal groups (29.67 %) not considered part of either cluster have been made purple and less prominent.

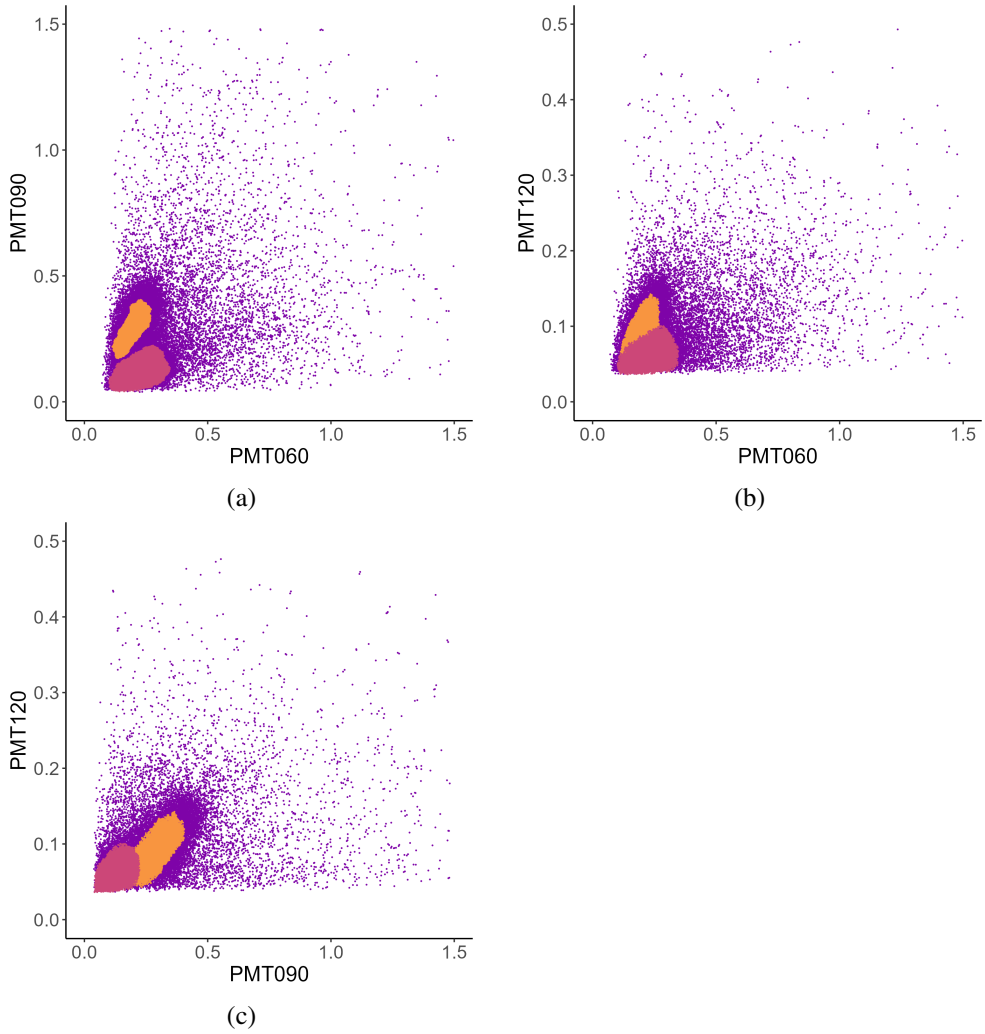

Figure 3.21: Scatter plots showing the 350 nm and 500 nm PSL mixed-particle sample data from figure 3.17, with the DBSCAN clustering results coloured by cluster. Pink shows the cluster associated with 350 nm PSL particles, made up of 30724 signal groups (52.95 %). Orange shows the cluster associated with 500 nm PSL particles, made up of 10085 signal groups (17.38 %). The 17217 signal groups (29.67 %) not considered part of either cluster are purple.

This ability to quantify the clustering of a set of signals is exceptionally useful for characterising the aerosol present in an area, but this currently method using DBSCAN does have limitations. With only one set of mixed-sample data which shows any separation, it is not possible to find parameters for DBSCAN which will consistently cluster data appropriately. If the parameters have to be entered manually, clustering is then being done by the user's interpretation, and is prescriptive based on what the user desires to find rather

than descriptive of the data. As part of potential work developing the MPS, further analysis using PCA and DBScan would improve the MPS' capacity to characterise complex aerosol environments. This would be further improved in conjunction with lookup tables indicating typical scattering patterns of common aerosol.

3.6 Conclusions

Experimentation using the MPS has demonstrated that the OPS instrument-class, while well-established and robust, has potential to provide greater insight into optical scattering behaviour of aerosol particles. The theoretical and laboratory experimentation presented in this chapter showcase the viability of utilising more complex scattering collection arrays to gain more information about scattering behaviour. The use of three detectors unlocked a new dimension of visualisation, which demonstrated an impressive ability to differentiate mixed samples, match experimental data to simulated data based on distinct regions of scattering, and validate data by having multiple data points for each particle where a standard OPS would have one. This also made it far easier to identify anomalous signals by verifying the signals detected at that moment by all three detectors.

PSL particles of between 200 and 1000 nm provided clearly identifiable signal patterns that largely agreed with theoretical simulations, both in terms of signal distribution and relative intensity of scattering within the different regions. This is exceptionally promising, as it demonstrates the successful use of multiple detectors to get more scattering information from each particle, and therefore build a more detailed picture of the various aerosols in a given environment. There is scope to use the scattering model to build extensive lookup table libraries, and thus be able to identify particle signatures within mixed samples. However,

accurate determination of the MPS' size resolution was not possible over the course of the experimentation during the project , and given the available particles. Further experimentation with a wider array of particle types would be beneficial, along with reducing the uncertainty of scattering results (both experimental and theoretically determined via simulation). While the resolution of the MPS has not been fully explored, the high dynamic detection range of the MPS has been demonstrated. Comparing absolute scattering signals from the 200 nm and 1000 nm PSL reveal the sheer range of scattering intensity which is possible to detect with the MPS, especially since even the largest scattering signals do not approach the upper limits of the PMTs' range.

Within the scope of this chapter and the detailed experimentation, the versatility of the MPS modular design was not expressed to a great degree, as most physical specifications were kept constant during lab-work. Based on this, the benefits of modularity are still purely theoretical; based on evaluating the simulated data. However, chapter 4 details the MPS in a significantly different configuration, with a significantly different experimental setup, for a distinct purpose.

Experimentation also showed areas in which the MPS' ability is limited, either due to design flaws, or insufficient simulation capabilities. The poor results of the attempts to analyse the larger PSL particles (2000 and 3000 nm) may be flaws in the auxiliary components, as well as the MPS nozzle.

It is apparent that the core systems of the MPS are functional and capable of collecting scattering data from aerosols, but considering the MPS as a full self-sufficient instrument, it

is still decidedly in the early stages and would require more iteration. In order for the MPS to be usable in a field-test or any other non-laboratory environment, the core components would need to be contained in a case with connections for sample intake and vacuum pump or air compressor, rather than existing as linked but separate components.

Chapter 4

Integration with Optical Tweezers

4.1 Introduction

Previous chapters have detailed the creation and testing of the multi-angle particle sizer (MPS), exploring its use as an optical particle sizer (OPS) with the added capabilities of utilising multiple detectors. However, one of the main considerations from the initial design process was a desire to maintain the modularity of the MPS. This would allow flexibility during the design, manufacturing and early laboratory testing, before all the components were finalised and before the exact functionality of the instrument was determined.

This modularity also provided an additional secondary benefit; by creating alternative versions of some core structural components but leaving the optical parameters and software unaffected, the MPS could be repurposed to perform different forms of analysis. In this case, the MPS was modified to integrate with another instrument which allowed for the observation of optical properties of aerosols which change over minute- or hour-timescales.

Much of the design experimentation and analysis described below took place concurrently with work presented in previous chapters, especially the design iteration and component manufacturing detailed in chapter 2. Advancements and discoveries made within the course of this work went on to effect elements of previous chapters. For the sake of continuity of theme, all of the elements relating to the following laboratory work, including the design of components and alterations to software parameters, have been thus-far omitted and are presented here.

4.1.1 Limitations of the MPS and Other OPS Instruments

OPS can be used to precisely analyse and characterise aerosol particles using the scattering of a particular wavelength of light. Achieving this scattering from a single particle is often done using a focused jet of aerosol and measuring the momentary scattering that occurs while each particle crosses the laser beam. This approach allows for characterisation of many particles very quickly, but limited scattering data is retrieved from each individual particle (over a micro-second time-scale). This can cause problems when testing an OPS instrument like the MPS since it is not possible to observe scattering from a specific particle more than once, or over an extended duration. Observations of this kind would be useful as they could be used to evaluate the MPS' ability to detect small or gradual changes in particle properties and thus the instrument's sensitivity. It would also expand the scope of the MPS' capability to either characterise how the optical properties of volatile or otherwise short-lived aerosol particles change over time, or use optical characterisation to identify other changes in physical properties that are not easily observed using other methods.

Another drawback of the current MPS configuration that uses a jet-delivery approach is that it also precludes simultaneous analysis of each specific particle using additional optics. An alternative method of particle delivery into the MPS that did not change fundamental functionality and would allow for simultaneous analysis using other optics was considered for investigation; use of an optical tweezers setup.

4.1.2 Optical Tweezers

Optical tweezers are a class of instrument that use focused light to trap and manipulate microscopic objects and particles. They are used in the analysis of biological molecules such as proteins and bio-polymers as well as non-biological materials like polystyrene latex beads and liquid droplets.[79] A microscope objective lens is used to focus a laser in such a way that the forces exerted by the light form a potential energy well, into which the particle can become trapped. The tweezers can either be constructed using a single objective lens, or two lenses, the focused light from which exert opposing forces on a trapped particle. This trapping can be maintained for as long as the particle remains sufficiently stable. Due to its contactless nature, it allows the trapped particles to be analysed using other optical analytical techniques without obstruction. Other methods of contactless trapping are available, but it was not possible to access equipment to test integration with the MPS.

Figure 4.1 shows a diagram of the optical tweezers used for this experiment, adapted from a paper by Jones et al., 2013.[80] It is a two-objective trap which uses a 1064 nm neodymium-doped yttrium aluminum garnet (Nd:YAG) laser to produce the trapping beams, and a windowed aluminium cell which sits between them.[81] The power of the beams at the point of focus is 10 mW for the upwards-facing beam and 15 mW for the downwards-facing

beam. The cell provides a sealed, controllable environment to contain the particle while it is trapped. It is this cell and the side imaging apparatus that was replaced with the modified MPS for this experiment.

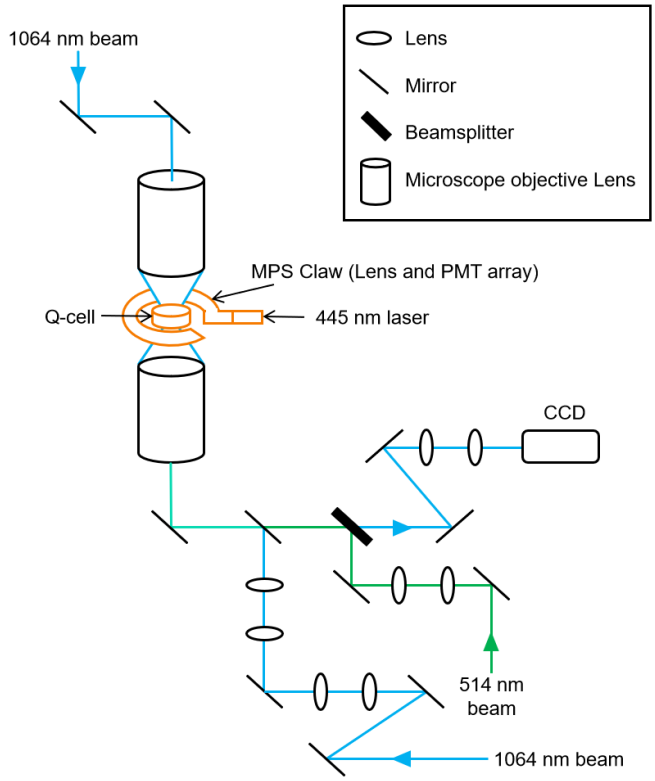

Figure 4.1: Diagram of optical tweezers setup. CCD was used for live particle imaging.

4.1.3 Limitations of the Optical Trap

There are limitations on the particles that these optical tweezers can trap, based on the particles' properties. For example, spherical particles are optimal since the forces exerted on it while trapped do not change with orientation, non-spherical particles would be pushed unevenly and become more likely to escape the trap. Particles must be within a given size range for optimal trapping, around 1-3 microns in diameter for these optical tweezers. The trap was also very sensitive to physical disturbances, so the entire experimental setup was

preformed on a passive, pneumatically damped optics bench.

The trapping of particles is not directly controllable; many particles must be introduced into the cell so that it is very likely one will enter the trapping location and be trapped. This has the side-effect of leaving the cell with a high concentration of excess particles which could interfere with scattering measurements and therefore must be left to settle on the cell walls or removed using gentle flow of a dry exhaust gas (e.g. nitrogen). In addition, for liquid samples that must be nebulised, the size of the droplet can't be controlled or predetermined, and the nebulisation and trapping process may need to be repeated multiple times to achieve trapping of a droplet of the desired size. The optical properties of the trapped particle are also important, since a particle that absorbs light at the wavelength of the trapping beams would become excited and either escape the trap or decompose via evaporation.

4.2 MPS modifications

The standard function of the MPS instrument relies on illuminating a jet of aerosol particles with a laser and measuring the light scattered in different regions using three photodetectors positioned at different angles. These components surround an enclosed central point, where the laser beam and particle jet intersect. The beam and photodetection array all align on a single plane which is perpendicular to the path of the aerosol. This geometry allows for the particle jet inlet and outlet to be replaced with a similar single-axis method of delivering particles to the beam path (such as the optical tweezers) without disrupting the spacial arrangement of the beam and photodetection array. The fundamental method of particle analysis based on quantification and comparison of scattering to multiple regions, including

the specific angular size and location of those regions, can be retained while using the MPS in conjunction with an optical trapping instrument.

4.2.1 Central Chamber

The main consideration was redesigning the central chamber that holds all other pieces in position as well as creating an airtight environment, as the requirements are different. In both instances the laser, detectors and optics are arranged on a single plane, surrounding a central point; the point at which the scattering beam interacts with a particle. In the original MPS chamber design incorporates ports for a nozzle which delivers an aerosol jet, which travels orthogonal to the optics plane, and an aerosol outlet. For this application the optical tweezers take the place of the aerosol nozzle and outlet, and require windows for the trapping beams as well as free space for the objective lenses (figure 4.2) to sit in their standard positions.

The first approach considered was an attempt to fulfill the requirements of both the MPS as well as the trapping cell using a single component. As such the design was composed of a disc which provided mounting points for the laser and photodetecion array as well as an enclosed centre with windows on the top and bottom to allow for trapping. Ports for injection and exhaust of the nebulised particles were also necessary, as well as a port for the optional inclusion a relative humidity and temperature (RHT) sensor. A model of the design can be seen in figures 4.2 and 4.3, with figure 4.3 also showing how it would be integrated with the optical tweezers.

This design, while simple in the sense that it could be manufactured from a single piece of aluminium and supported all necessary components, introduced a number of issues which

ultimately would have made it impractical to use. The distance between the top and bottom objective is only 34 mm so, due to the existing PMT mount designs being 41 mm tall, the design needs to be thinner in the centre than at the edges. The requirement that the cell move up and down to maximise the chances of trapping mean that to maximise its potential as a trapping cell; the thickness of the centre of the chamber was limited to only 15 mm. This causes issues such as structural weakness. Additionally, due to the required diameter of this indentation, the chamber blocks a portion of the light which would otherwise reach each detector. The need to manipulate the whole MPS to move the cell for trapping necessitated mounting it on a single translation stage, increasing the risk of misalignment due to the combined weight of all components.

Another issue with this design was the need to periodically clean the interior of the cell to remove condensed aerosol from the windows (and lenses in this design), as this buildup would reduce trapping ability and affect the scattering reaching each detector. This would be impossible to do without removing the entire MPS instrument, which was sufficiently difficult, delicate and time-consuming to ultimately make this design infeasible as a solution.

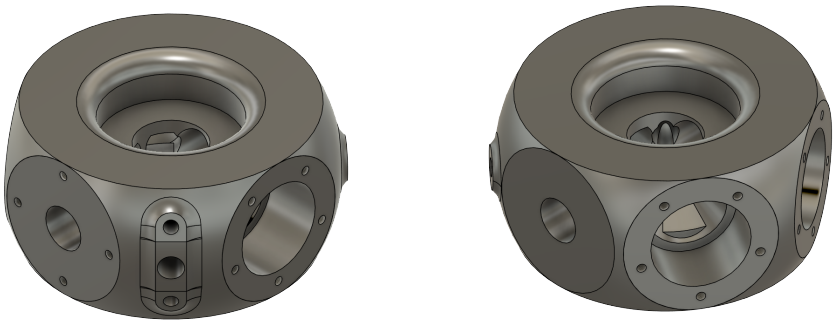

(a) (b)

Figure 4.2: Isometric view of the proposed all-in-one modified central MPS chamber. (a): Front view which shows, left to right, laser-in port, aerosol and humidity sensor ports, and finally the PMT 90 port. (b) Rear view which shows, left to right, the chamber-mounting point, the laser-out port, and the PMTs 60 and 120 ports. The chamber is 41 mm thick width a diameter of 88 mm.

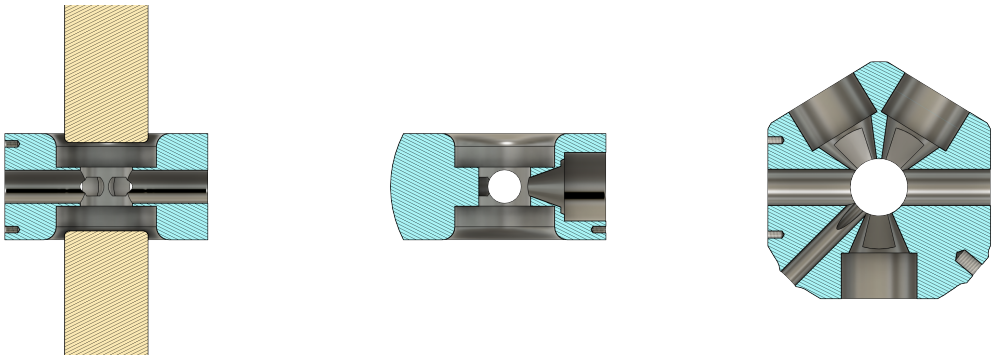

(a) (b) (c)

Figure 4.3: Cross-sections of the all-in-one chamber design. (a): Shows the laser path as well as representations of the size and position of the optical tweezers' objective lenses (yellow). (b): Perpendicular cross-section, showing conical cavity which facilitates collection of scattering by PMT 90. (c): Horizontal cross-section showing all ports to the chamber's centre.

An alternative approach utilised a two-part design, with one part maintaining the relative positions of the laser and detectors, and another acting as the sealed cell. This approach had a number of benefits over the one-part design, as well as some drawbacks. With the cell as a separate component, the outer chamber no longer needed to completely enclose the trapping location or maintain an airtight seal. This outer component (henceforth referred to as the claw) almost completely surrounds the cell (as seen in figure 4.4), and supports the

laser, three photodetectors and all optical components. The beam dump did not need to be attached to the main assembly for this configuration, which reduced congestion around the trap.

The cell (also referred to as the q-cell due to its shape, seen in figure 4.4) component was required to have seven windows; two for the trapping lens objectives, two to allow the MPS laser to enter and exit the cell and three which are angled to face the three PMTs. As with the single-piece design, injection and exhaust ports in addition to space for a RHT sensor were included. These were placed in line with a mounting arm that was positioned to not block the laser or make contact with the claw. The aerosol inlet port was also specifically designed with direct, straight-line access to the cell's centre, to minimise loss of particles via deposition during nebulisation and injection.

This separation of optics mount and trapping cell added significant complexity to the experimental setup, since the trapping objectives, optics mount and cell needed to be precisely and reliably aligned such that no scattering was lost, and results between trapping events were comparable. The chosen method to align the cell with the trap was to place a needle in the cell via the RHT port, such that the centre of the needle was in the centre of the cell, and align the point of the needle with the trap via the in-built camera. The claw could then be adjusted until the MPS laser reflected off the needle point, ensuring the centre of the cell and the claw were aligned with the trap. An advantage of this system, however, was that the cell could) be re-positioned, removed and cleaned (which would be necessary due to deposition of nebulised material build-up on the lower window) without adjusting the optics. Due to the size and arrangement of the optics mount, removing it from the trapping location was tedious and carried a risk of disturbing the upper objective's supports (and thus

misaligning the tweezers). This design ultimately simplified experimental procedure because the optics did not have to be removed, or adjusted as frequently. Two copies of the cell were manufactured to protect against component failures and reduce experimental down-time.

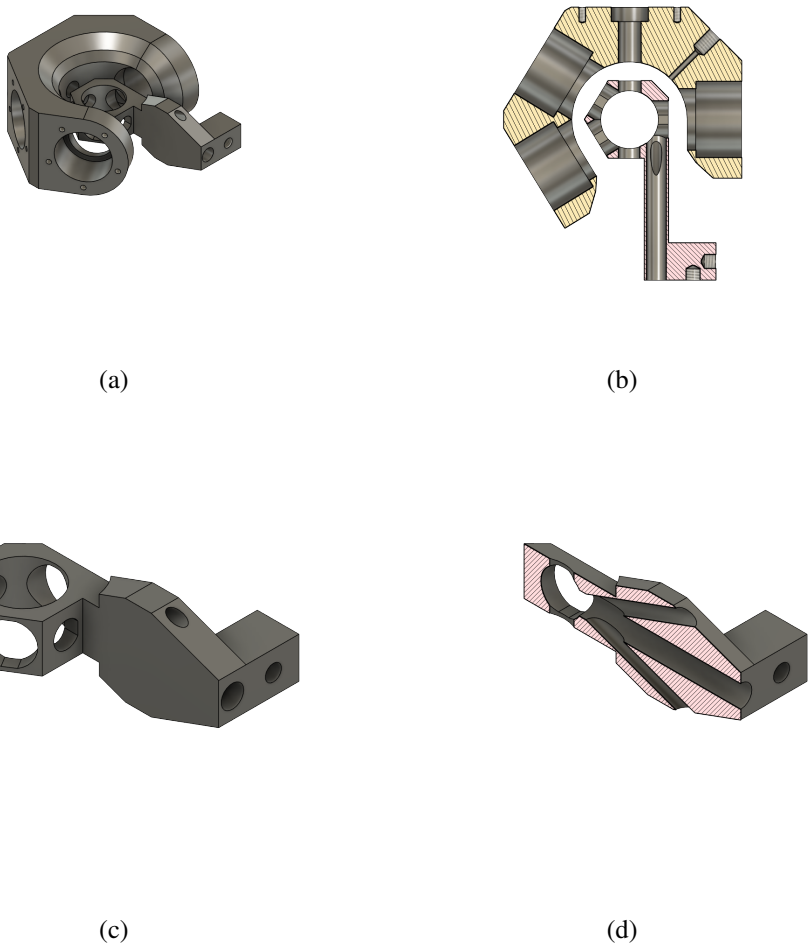

Figure 4.4: Model of two-part MPS design. Image (a) shows the claw and q-cell in the correct alignment for experimental work within the trap. (b): A top-down cross-section. (c): Q-cell only, shows circular cutouts over which glass coverslips were placed. (d): Cross-section along aerosol inlet (top), aerosol outlet (bottom) and relative humidity sensor port (the larger, central port).

4.2.2 Laser

The MPS typically uses a linearly polarised, collimated, continuous wave laser with a wavelength of either 405 or 445 nm. During testing it was determined that, due to the laser's power output having reduced over the course of the project, focusing the beam at the trapping location would yield better scattering signals and facilitate better alignment with the trap. To achieve this the previous collimating lens mount was replaced with a Thorlabs 30 mm optics cage system, which housed the collimating lens, iris, and two focusing lenses. A diagram of the components contained by the cage system is shown in figure 4.5. This added size and weight to the MPS outer chamber, but did not make the claw too heavy to reliably adjust once integrated with the optical tweezers, and minimal changes to the chamber were required to integrate the cage system.

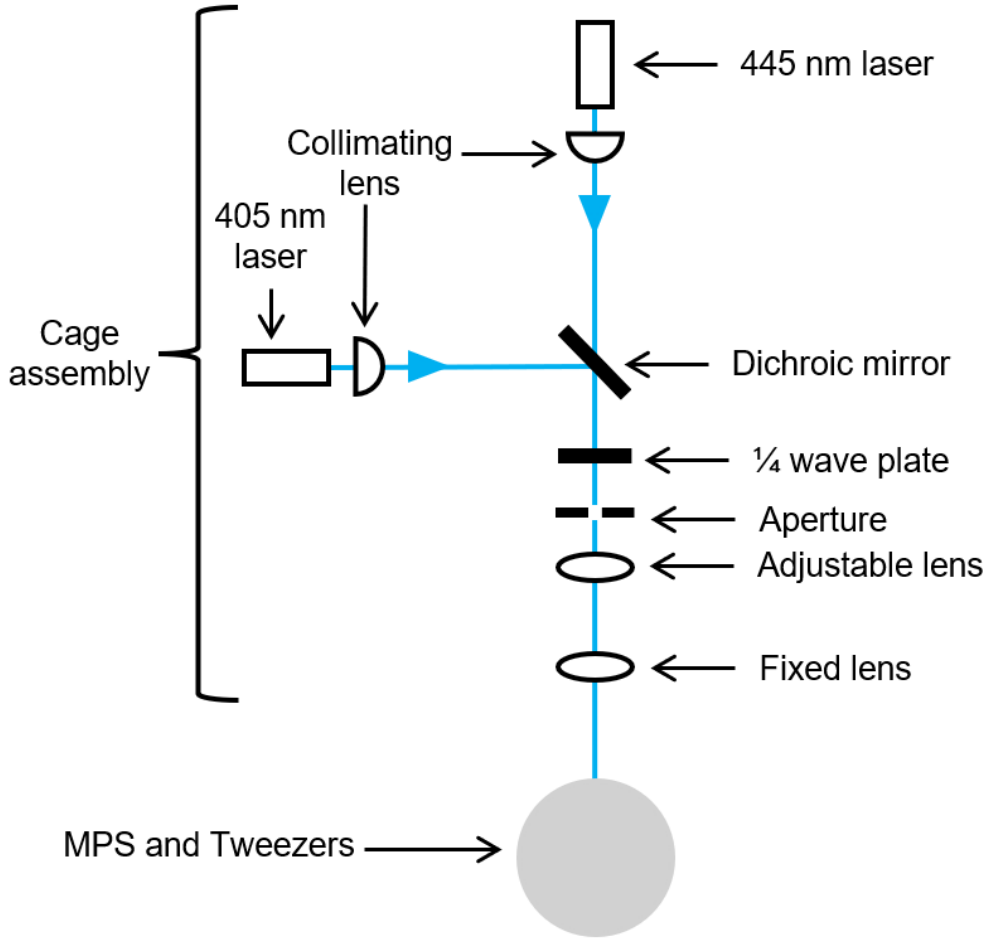

Figure 4.5: Diagram showing the components housed in the Thorlabs 30 mm cage system. Adjustable lens allowed for focusing of collimated beam.

4.2.3 Software and Data Acquisition

The custom MPS data display and acquisition software was adapted to allow for for this different application, without impacting previous functionality. Rather than detecting scattering peaks from particles intersecting the beam on a microsecond-timescale, the trap allowed capture of a single particle for times in excess of one hour. Consequentially, the standard sampling rate of 500-640 kHz was reduced to a more suitable 500 Hz(2 µs resolution), to reduce the risk of software slowdown or freezing disrupting continuous data collection.

4.3 Methodology and Experimental Procedure

4.3.1 Nebulisation and Particles

The substances analysed were aqueous NaCl, squalane in 1-propanol, trans-5-decene and aqueous ammonium nitrate (refractive indices in table 4.1). These were introduced into the q-cell using a nebuliser. These were chosen based on availability as well as ease of trapping. For example, gycerol was considered but all trapping attempts were unsuccessful. Polystyrene latex spheres were also considered but was not attempted due to the increased difficulty of trapping solid particles compared to liquid droplets, and the time needed to alter the setup to accommodate trapping solid particles.

Droplet	Refractive Index (Literature)
NaCl(aq.)	1.332[82]
Squalane	1.451[83]
Trans-5-Decene	1.424[84]
Ammonium nitrate(aq.)	1.410[85]

Table 4.1: Literature-reported indices of refraction of the analysed substances.

4.3.2 Imaging

A camera and imagining light are integrated into the optical tweezers, using the same objective lenses, allowing live imaging of trapped particles. It is important to note that while this camera was used to calculate size data complimentary to the data from the MPS, this was not its intended function. The purpose of the integrated camera was to allow for live viewing of the trapping zone, to visually confirm successful trapping and assess the behaviour of the trapped droplet. As such the resolution of the video and resulting images is only 480×640 pixels, enough to display the droplet clearly, as well as perform alignment checks, but not ideal for extracting size information, due to complications such as focus which is affected by

droplet movement within the trap. In spite of these drawbacks, the camera provided the only feasible source of droplet size information, which is highly unpredictable and is expected to change over the duration of trapping events, given the congestion around the optical tweezers caused by the MPS.

The scattering beam interacting with the trapped droplet was visible on the captured images which mostly or completely obscured the particle and thus prevented accurate size determination, so in order to obtain a useful droplet profile the scattering laser was turned off periodically for a short period. From the recorded video data, droplet size information was systematically determined for every frame in which the scattering laser was turned off. Each video frame was converted to an image, then to a matrix of pixel brightness values. Covering the region of the image where the droplet was expected to be (figure 4.6), each pixel row was separated. Due to the brightness of the droplet differing from the rest of the image, the area the droplet occupied on each row could be considered a peak in an otherwise uniform series. The particle's width on that row could be determined by calculating a rolling background (to account for the variability in background brightness) and determining peak width. The maximum peak width across the selected rows was selected as representing the droplet's diameter for that frame. This results in a series of diameter values over the duration of trapping.

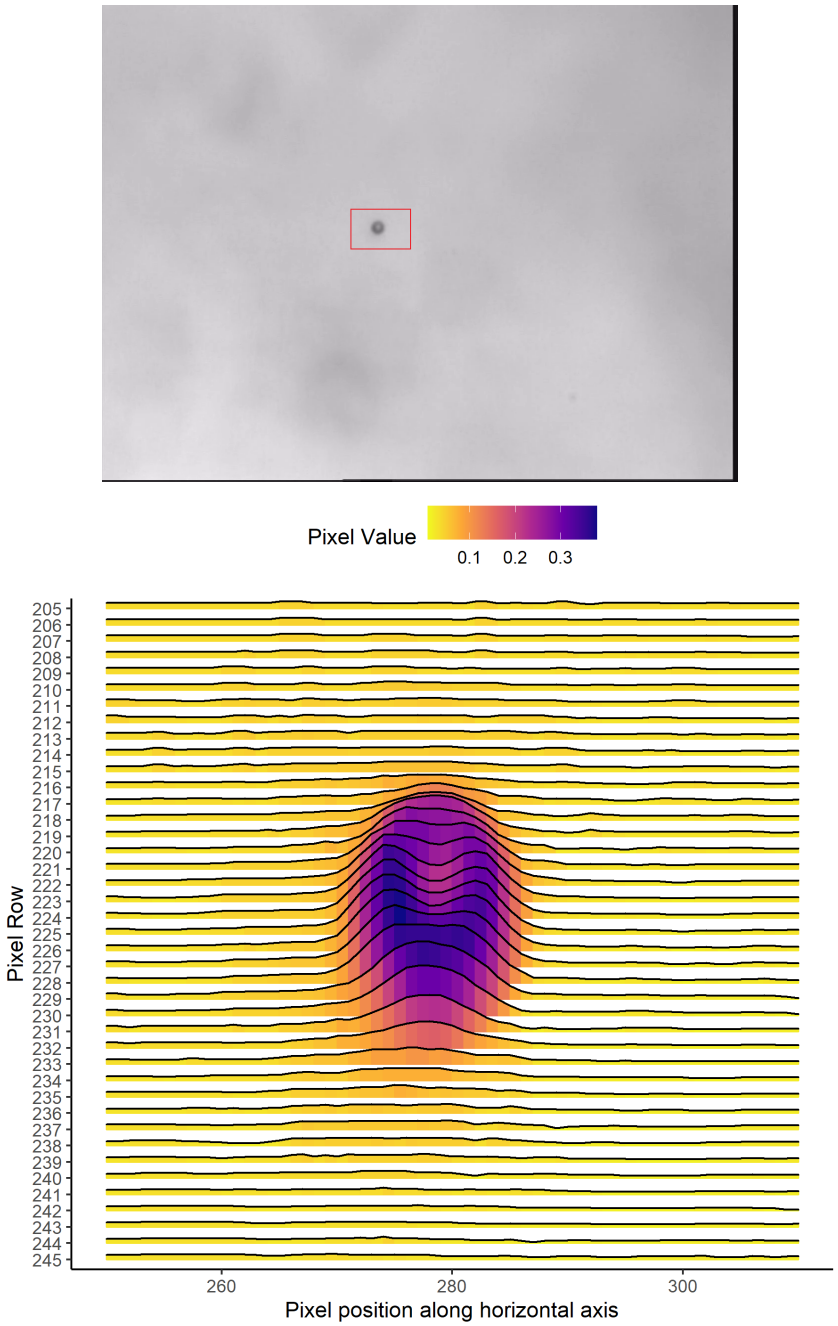

Figure 4.6: (Top): Single frame of 480 × 640 px resolution grey-scale video capture of aqueous NaCl droplet suspended in optical trap. Captured at 1 frame per second over duration of droplet trapping events. Red box indicates region displayed in plot. This image covers a 98 × 128 µm area. (Bottom): Plot showing peaks generated from pixel brightness values of the image, used to dynamically find the diameter of the particle in each frame. Based on this analysis, this NaCl particle was determined to have a diameter of 3 µm.

4.3.3 Relative Humidity

Humidity was measured in the q-cell using an RHT sensor (SHT75, Sensirion AG, Switzerland). Flowing dry nitrogen gas was, during some trapping events, pumped into the chamber to remove non-trapped droplets from the cell and particularly beam path in an attempt to reduce background noise, and reduce humidity. For another trapping event, the relative humidity was raised to a constant level by bubbling nitrogen gas through water before introducing it to the q-cell. This was done in an attempt to prevent evaporation from the droplet and improve its long-term stability.

4.3.4 Lasers

Three lasers were used to obtain scattering. The primary laser used for scattering was the 445 nm laser, also used by the MPS in its original configuration, aligned on the same plane as the MPS optics. Unlike with the original MPS where the beam was collimated, for use with the optical tweezers the beam, was focused to approximately 50 microns on to the trapping location. A 405 nm laser was used as a backup for this laser.

The third laser used was an Ar-ion 514 nm laser pre-integrated with the optical tweezers, which was tightly focused on to the trapping location via the lower objective. The configuration and alignment of this laser was similar to the white light source in figure 4.1. A consequence of this is that all three photodetectors are positioned 90 $^{\circ}$ from the incident direction. However, they were still expected to receive different amounts of scattering due to their differing positions relative to polarisation of the 514 nm laser.

4.4 Imaging Data

The imaging technique has a resolution of only 0.2 μm per pixel, and thus can only provide an approximate estimate of changing size given typical droplet diameters of $\sim$ 1-4 μm. Even with this limited precision it has been possible to quantify the changing size of the droplets over the trapping duration.

For each calculated value for diameter of the particle, it is possible to use the same scattering simulation detailed in previous chapters to predict the expected scattering that the MPS will detect with each PMT. However, much like the polydisperse PSL samples used in chapter 3, the image-derived values are only an approximate diameter. An important difference between this image-derived data and the size values used in chapter 3, is that the distribution of possible diameters of the trapped particle is completely uniform over the large range imposed by the low resolution. Due to this, each diameter measurement produces a range of possible sizes, each equally likely to be the true value, which can be used to predict scattering. These predicted scattering ranges form their own duration, the distribution of which is not necessarily predictable.

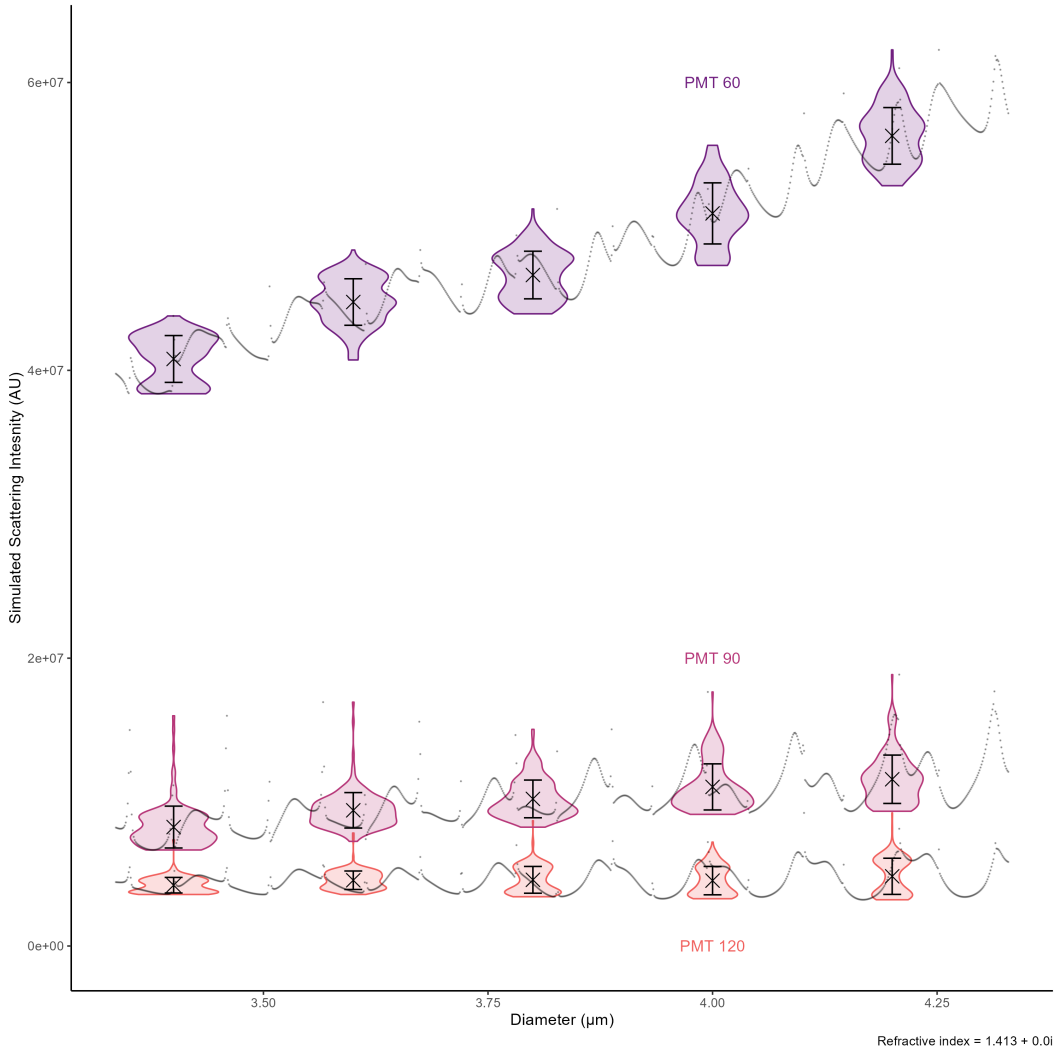

Figure 4.7: Scattering intensity which would be recorded by each PMT, for a range of particle diameter (assuming a uniform sphere with a CRI of 1.413 + 0.0i (a CRI in the region of the particles analysed)), along with mean values (crosses), representing the average intensity of each 0.2 μm range; the resolution of the in-built optical tweezers camera. Violin plots also show the distribution of intensities within these ranges.

Imaging data for all successful trapping events was processed using the method described above to produce a series showing the change in particle diameter over time. This provides a visualisation of the progression of particle size over the course of each trapping event, many of which lasted for more than 60 minutes. This approach required a lot of manual tuning, since in addition to the expected particles size fluctuations occurring over minute- or hour-timescales, initial size data displayed large variations in size within relatively small window of time. These apparent changes in size are in most cases due instead to oscillation of the particle within the trap. This oscillation is an issue because of the narrow focus of the imaging lens, which will in turn prevent the saved image from providing an accurate particle size. For this reason these points were removed from time-resolved size data, or selectively retained after manual image verification. The remaining data is presented in figure 4.8.

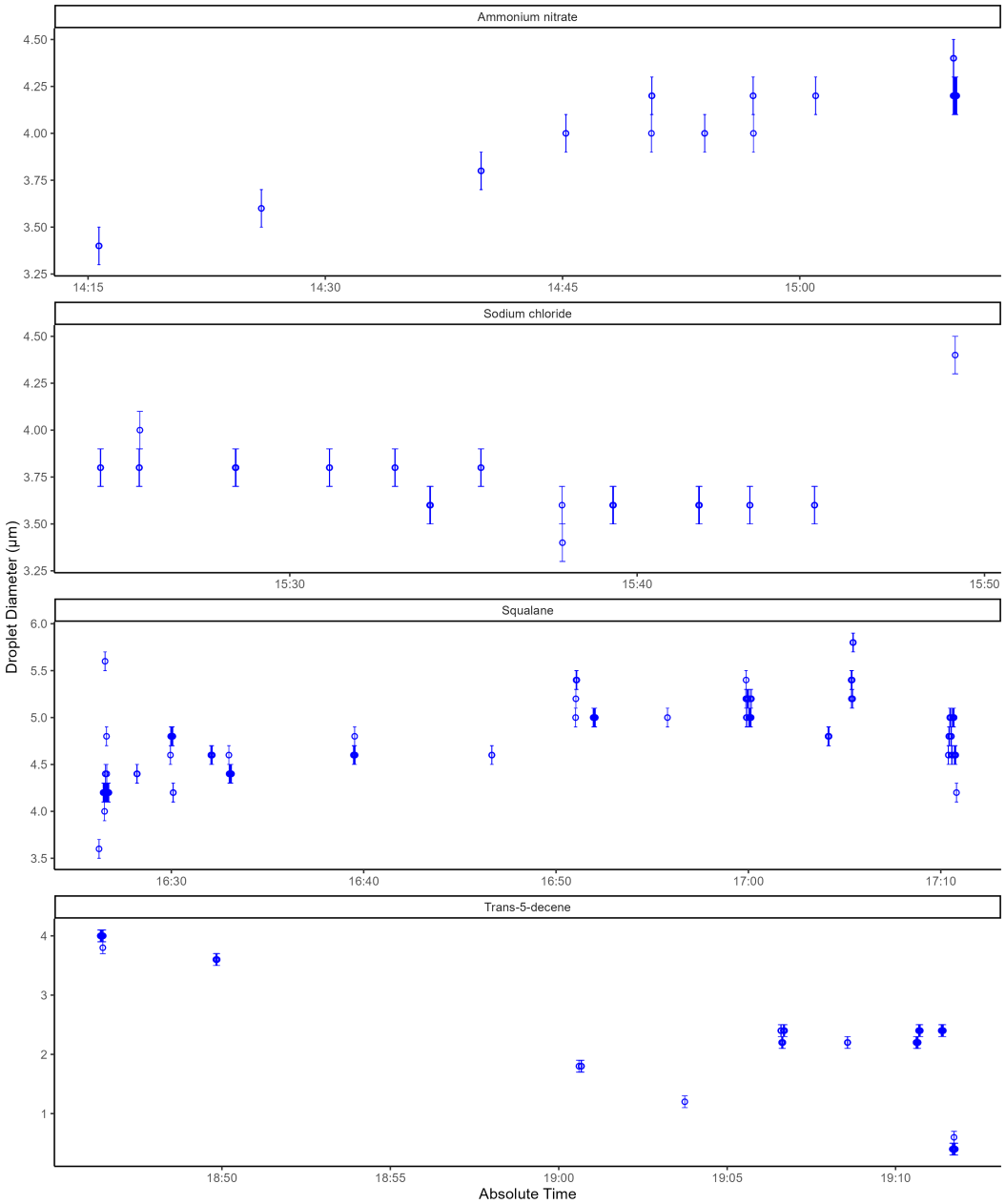

Figure 4.8: Calculated diameter measurements of the four trapping events discussed in this section: Ammonium nitrate (aq.), sodium chloride (aq.), squalane (in 1-propanol) and trans-5-decene. All error bars represent the ± 0.1 limits of the camera.

The majority of trappings events show a change of size consistent with expectations based on the internal conditions of the cell. For example, the ammonium nitrate (aq) droplet trapping event was performed in a high humidity environment and thus the droplet was predicted to increase in size over the course of the trapping event due to the addition of smaller water droplets to the trapped particle. In contrast, the squalane droplet trapping was performed in a low humidity environment to induce a gradual decrease in droplet size.

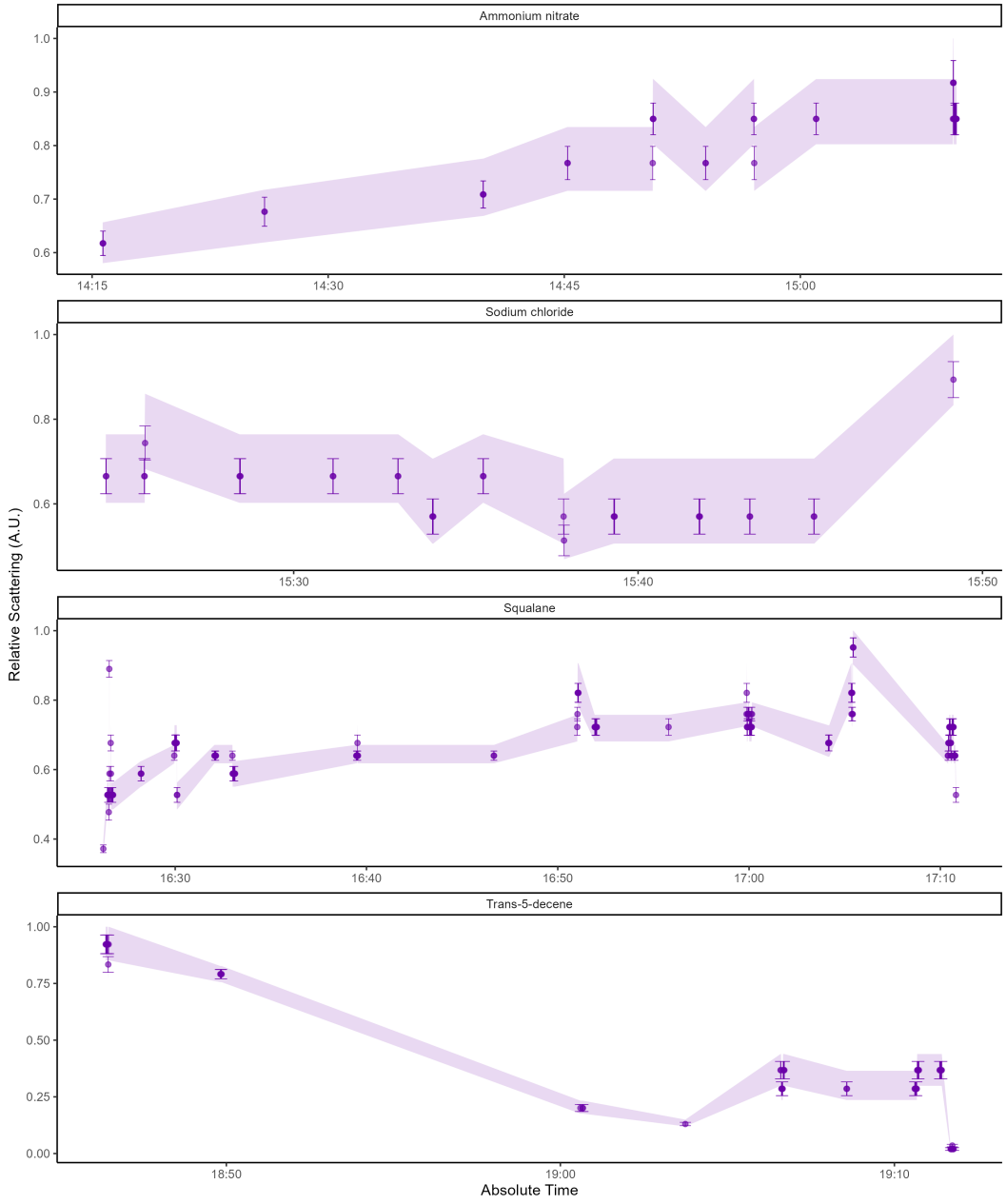

Figure 4.9: Theoretical scattering intensities predicted for the PMT060 photodetector, over the course of the trapping events (table 4.2), calculated using the diameter measurements (4.8). Points represent the calculated scattering for the exact sizes, the error bars show the standard deviation and the shaded area covers the full range of scattering possibilities given the large uncertainty in the image data

Figure 4.9 presents predicted intensity ranges of the scattering the trapped droplet would be expected to produce based on the currently observed size. These represent a dynamic window of scattering ranges, within which the MPS data is expected to reside.

4.5 Scattering data

4.5.1 Blue Laser Scattering

During the second week of experimentation, while many trapping attempts resulted in scattering data, this has limited usefulness unless paired with imaging data from which to obtain simulated scattering estimations and thus assess the MPS data. A total of nine trapping events performed have both MPS and image data. Of these, five were performed while observing 514 nm laser scattering only, two were performed while observing 445 nm laser scattering only, and two were performed alternating between the two lasers. The four trapping events including scattering from the blue laser are the main focus of analysis, given the MPS and complimentary theory simulations were set up to analyse scattering with that incident direction.

These four trapping events were performed with different droplet compositions, under different conditions, as shown in table 4.2. MPS scattering data was recorded for all of these, the raw PMT data for the ammonium nitrate, sodium chloride, squalane and trans-5-decene trapping events are analysed and discussed in this section. The raw MPS data from these events is displayed in figure 4.16, 4.10, 4.14 and 4.12, respectively. This PMT data has been

Droplet Composition	Duration (min.)	Environment	Laser	Diameter (μm) †
Ammonium nitrate (aqueous)	55	Wet nitrogen ‡	Blue only	3.4 - 4.4
Sodium chloride (aqueous)	36	Static	Blue only	3.4 - 4.4
Squalane (in 1-propanol)	71	Dry nitrogen	Blue and green	3.4 - 5.8
Trans-5-decene	46	Static	Blue and green	1.2 - 4.2

Table 4.2: Details of the trapping events wherein scattering was recorded using the 445 nm blue laser.
† Diameter here refers to the observed diameter calculated from camera images, with an uncertainty of $\pm$ 0.1 µm.
‡ 'Wet nitrogen' refers to nitrogen gas bubbled through water to produce a high-humidity environment.

scaled (by calibrating against a uniform light source) to correct for the individual set gains on the PMTs. For ammonium nitrate and sodium chloride, these data series are presented in full, as scattering was only produced using the 445 nm laser. In contrast, squalane and trans-5-decene, are discontinuous because the scattering produced by the 514 nm laser has been excluded.

All data series demonstrate the means by which images of the droplets were recorded; the laser was deactivated for at least 1 second leaving the droplet unilluminated by the laser, so it could be imaged and accurately sized. This can be seen in the data as the signal from all PMTs dropping to near-zero. These low regions were used as markers from which to calculate mean scattering values which could be compared to the image-derived theoretical scattering simulation data (figure 4.9). This was done by finding the mean and standard deviation of the 5000 (10 seconds worth) points which immediately precede each low region. This window was determined to be sufficient to calculate a meaningful average, while providing a region over which no significant drift in the scattering was observed, given the slow change in overall signal.

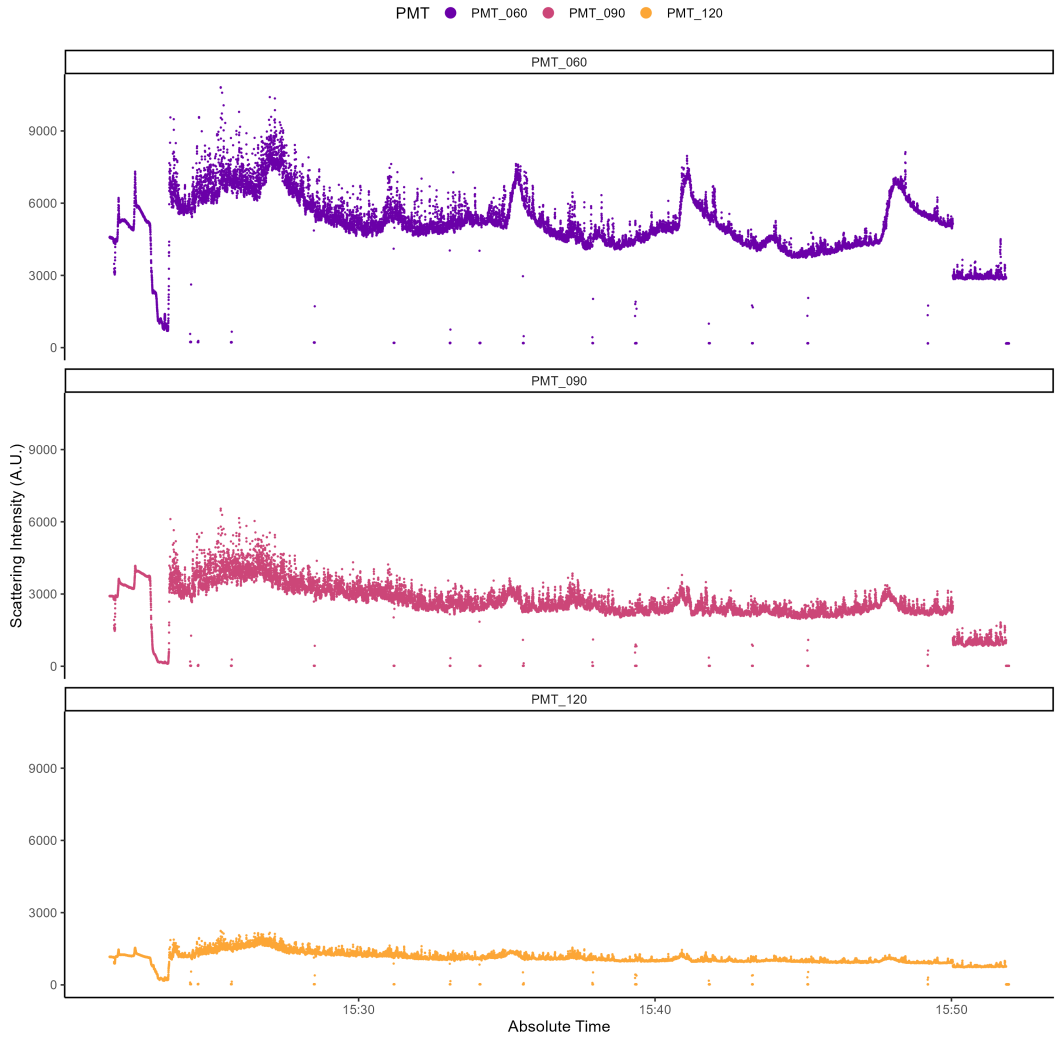

Figure 4.10: PMT intensity data recorded using the MPS, for the trapping of a sodium chloride droplet (detailed in table 4.2).

As stated in table 4.2, this droplet of aqueous sodium chloride was trapped for approximately 36 minutes, during which time the cell was sealed and no air flow was introduced. The most immediately apparent observation is the overall decrease in signal noise over the course of the trapping period, a phenomenon which is consistent across all datasets presented in this section. Given that this changes so dramatically across the 36 minutes, it is likely due to a change in the scattering environment. The probable cause of this is the high volume of nebulised droplets injected into the chamber, which will produce scattering signals whenever

interacting with the beam, and which gradually settle on the walls of the cell (or otherwise gather near the bottom of the cell) over time. The noise appears to reach a steady level at around 15:40 pm, indicating most of the non-trapped particles are no longer airborne or, at least, no longer in the beam path. The local environment has reached a stable state. Another feature of the raw data includes a steady decline in the scattering intensity over time. This is consistent with the predicted behaviour of the droplet; to gradually shrink due to evaporation, and therefore at least nominally consistent with the size data in figure 4.8. Finally, the steady decrease is punctuated with distinct peaks in scattering. These peaks are characterised by their regularity (about every 7 minutes), their constant shape (steep increase and relatively shallow decline), as well as the fact that they are present across all PMTs, but slightly offset from each other. Given the apparent steady decrease in size of the droplet, a possible candidate for the cause of these peaks is the fluctuation in scattering (predicted by Mie theory) that occurs within the angle ranges of the PMTs as the diameter of the particle changes, like those presented in figure 4.7. A potential method of testing this would be to analyse a stable particle not expected to change in size, such as a solid PSL particle.

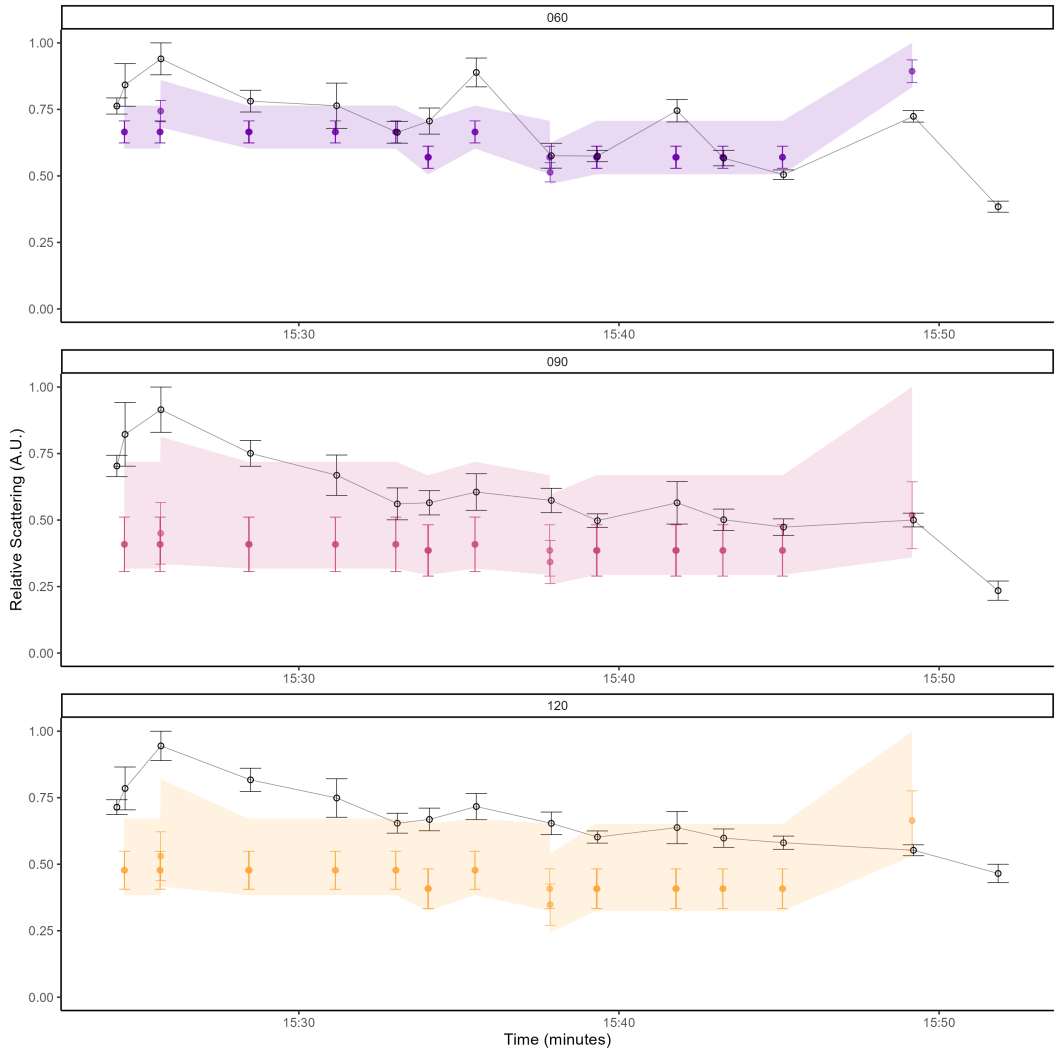

Figure 4.11: MPS scattering data (black) from the three PMTs, calculated from the raw data (figure 4.14) for each imaging window where the sodium chloride droplet was briefly deluminated. This data has been superimposed over the simulated scattering based on the image data (figure 4.8), the mean and full range of scattering based on that size range are shown.

Figure 4.11 shows a comparison between the PMT and image data, converted to relative scattering. Agreement of the trend in scattering is visible, but there are areas where they deviate significantly. This may be due to the low resolution of the camera and thus the uncertainty in the theoretical sizing data, as well as droplet movement interfering with image-sizing.

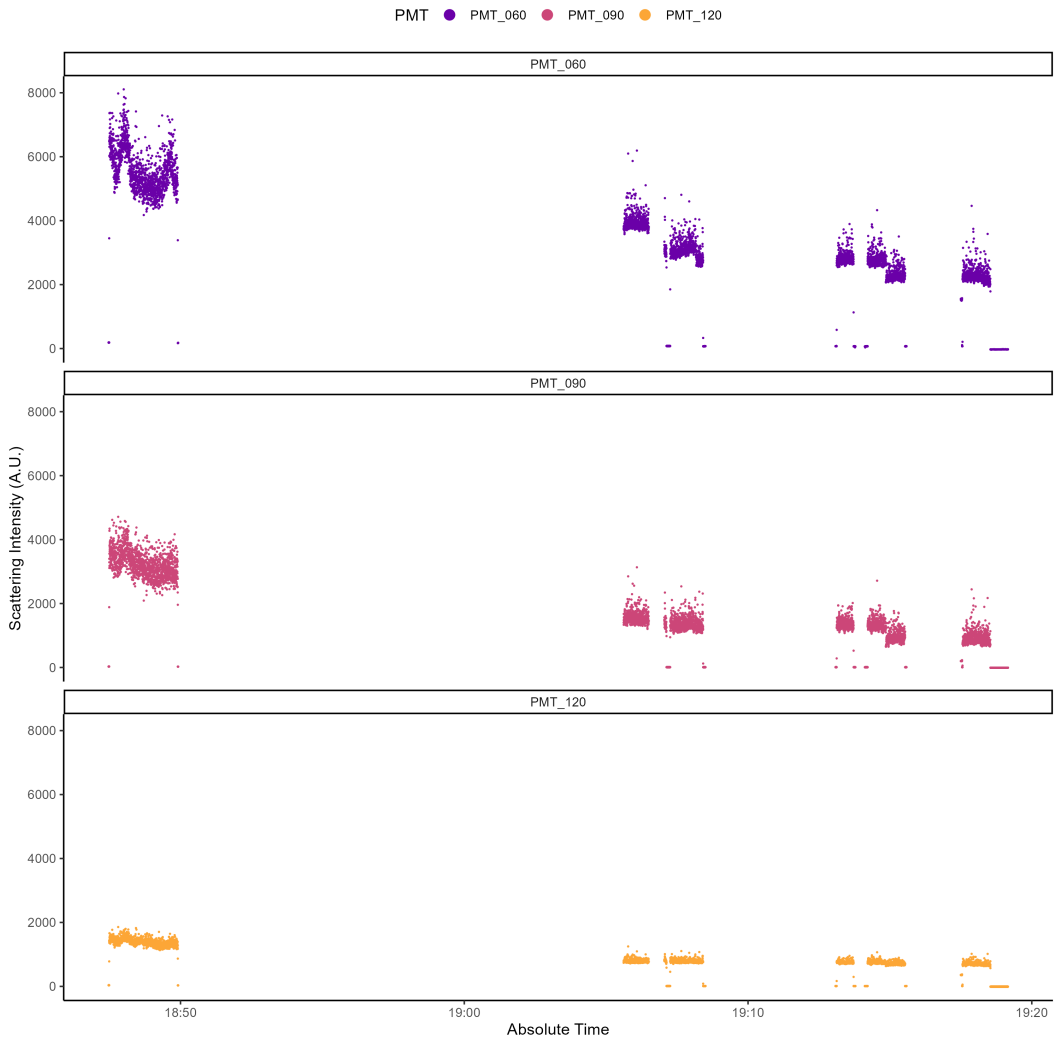

Figure 4.12: PMT intensity data recorded using the MPS, for the trapping of a trans-5-decene droplet (detailed in table 4.2).

Another trapping which was performed without any air flow was that of a trans-5-decene droplet, the raw PMT data of which is presented in figure 4.12, which was trapped for approximately 46 minutes. This dataset is discontinuous, due to alternation between the green and blue lasers, and only the blue laser scattering is presented here. As with the sodium chloride data, there is a clear decrease in scattering over the trapping duration, which matches the decreasing diameter measurements (figure 4.8). There is not a sufficient stretch of continuous 445 nm scattering to determine whether the same peaks of scattering observed in figure 4.10 occurred during this trapping event.

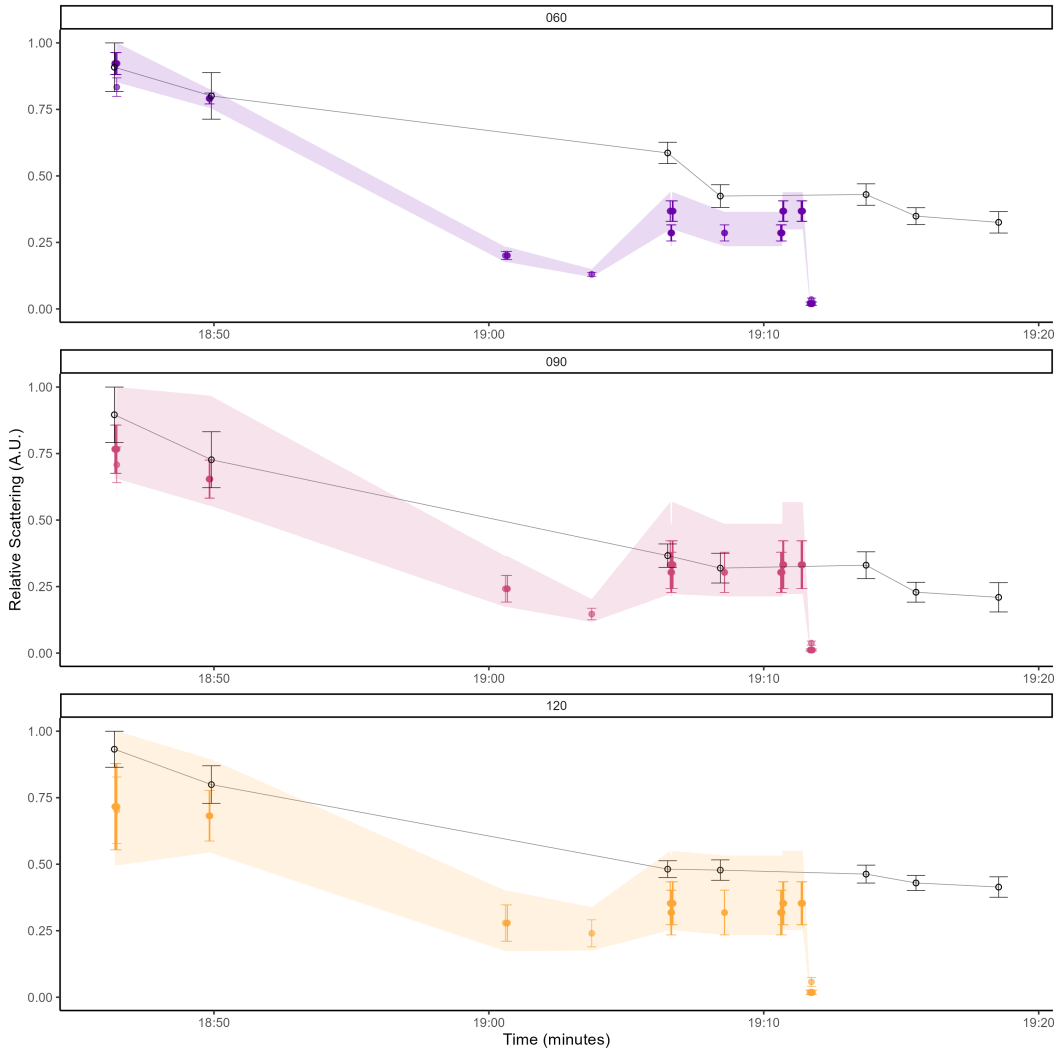

Figure 4.13: MPS scattering data (black) from the three PMTs, calculated from the raw data (figure 4.12) for each imaging window where the trans-5-decene droplet was briefly deluminated. This data has been superimposed over the simulated scattering based on the image data (figure 4.8), the mean and full range of scattering based on that size range are shown.

Figure 4.13 shows the agreement between the scattering data observed experimentally, and that calculated using the image data.

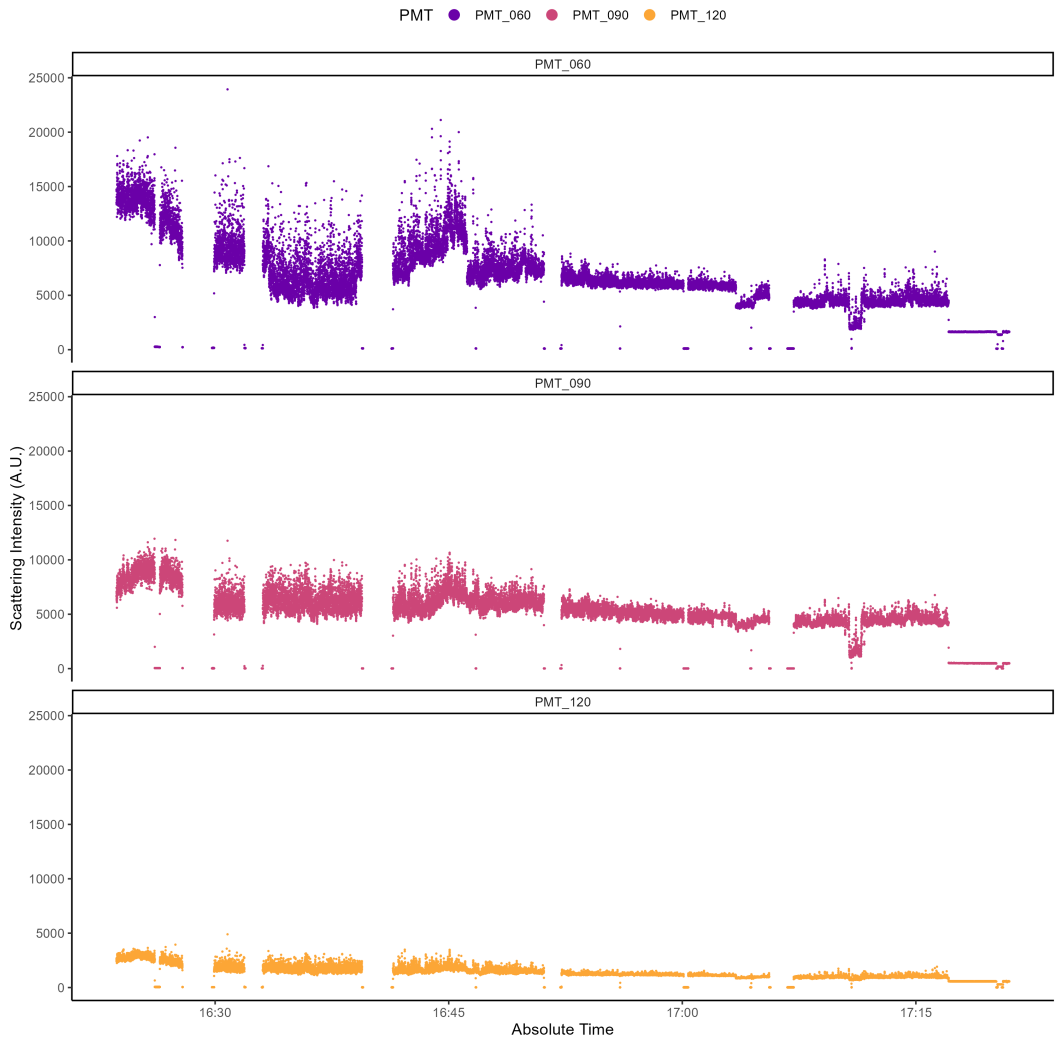

Figure 4.14: PMT intensity data recorded using the MPS, for the trapping of a squalane droplet (detailed in table 4.2).

The 71 minute trapping of a droplet of squalane in 1-propanol was performed under a dry nitrogen flow; approximately 100 $ml_n min^{-1}$ (millilitre normal per minute). The raw data (figure 4.14) shows that while the noise significantly decreases over time, it takes

approximately 25 minutes to do so, meaning that the flow of nitrogen may be agitating the droplets and preventing settling, rather than effectively removing them from the chamber. The PMT data shows a clear diminishing of scattering over time, which would imply a decrease in size. However, this conflicts with the image data (figure 4.8), which does not show a size-decrease. This droplet in particular was prone to instability within the trap. Attempts were made to correlate this instability which was observed using the live video feed with changes in PMT data, but this was unsuccessful as wobbling of the particle in the trap did not seem to have a significant effect on scattering. This instability may still be responsible for the incongruity of the image data and PMT data (figure 4.15), since movement of the droplet may have resulted in loss of focus and thus inaccurate diameter determinations.

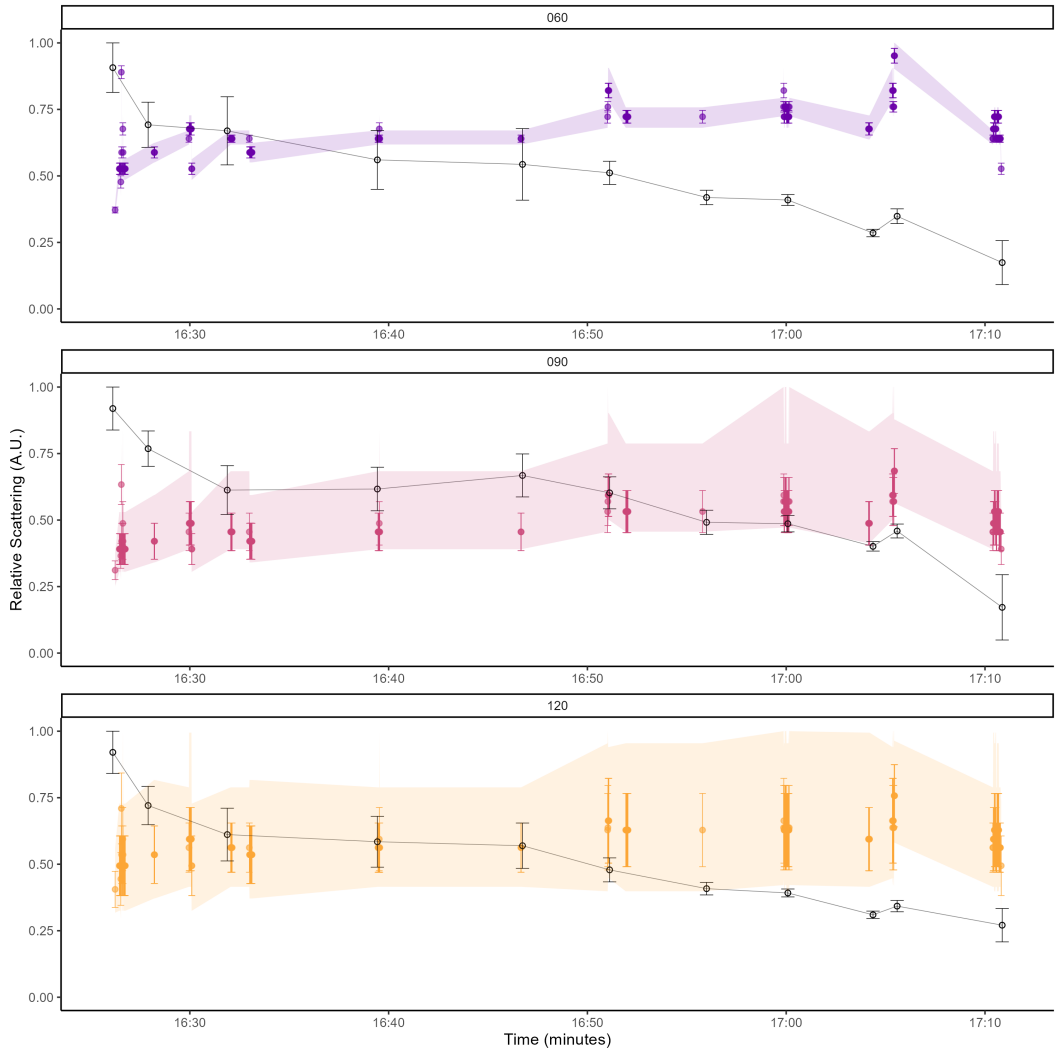

Figure 4.15: MPS scattering data (black) from the three PMTs, calculated from the raw data (figure 4.14) for each imaging window where the squalane droplet was briefly deluminated. This data has been superimposed over the simulated scattering based on the image data (figure 4.8), the mean and full range of scattering based on that size range are shown.

.

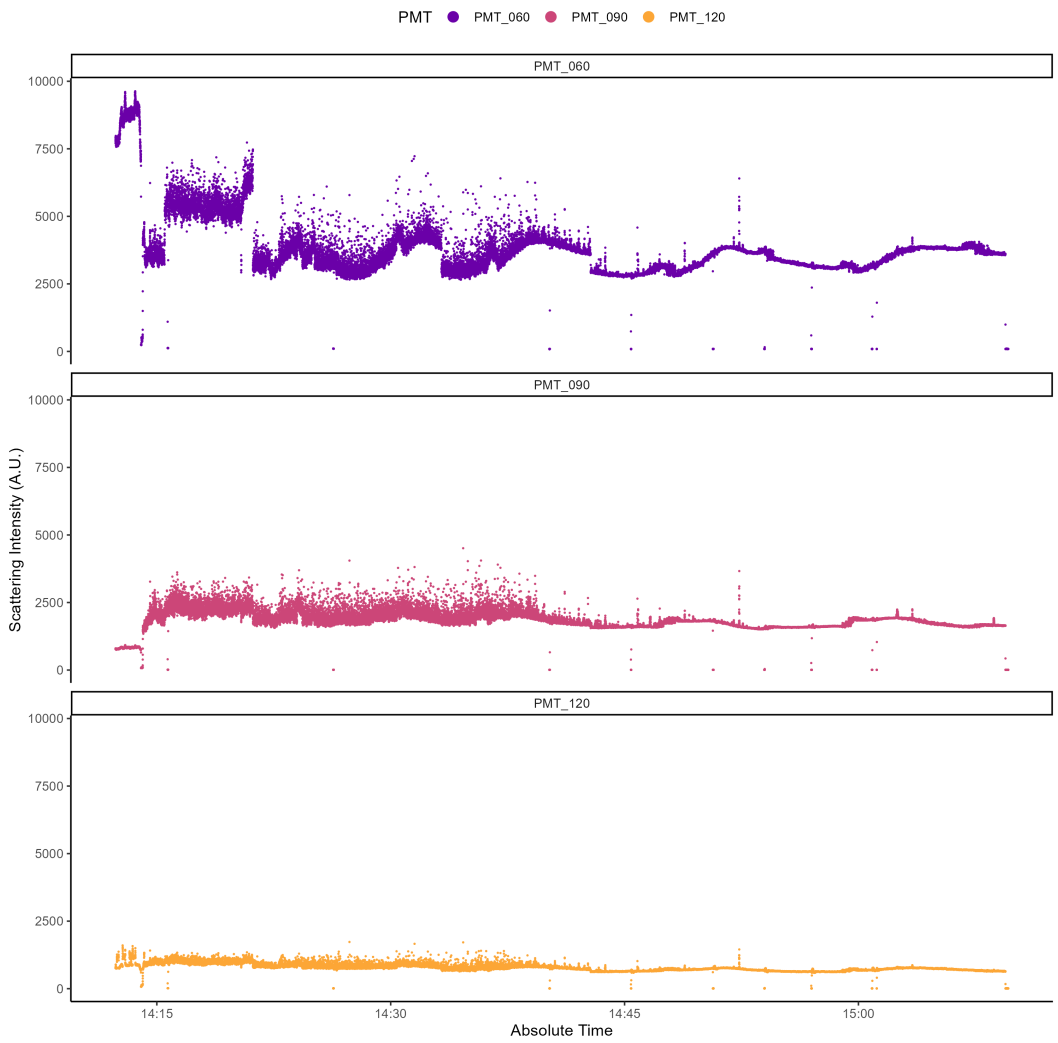

Figure 4.16: PMT intensity data recorded using the MPS, for the trapping of an ammonium nitrate droplet (detailed in table 4.2).

The forth and final trapping event performed with the 445 laser, with accompanying image data, was of an aqueous ammonium nitrate droplet. It was also unique in that it was the only successful run for which the humidity of the chamber was actively increased via bubbling a

flowing nitrogen source through water. This relative humidity data, recorded using the RHT sensor, is presented in figure 4.17.

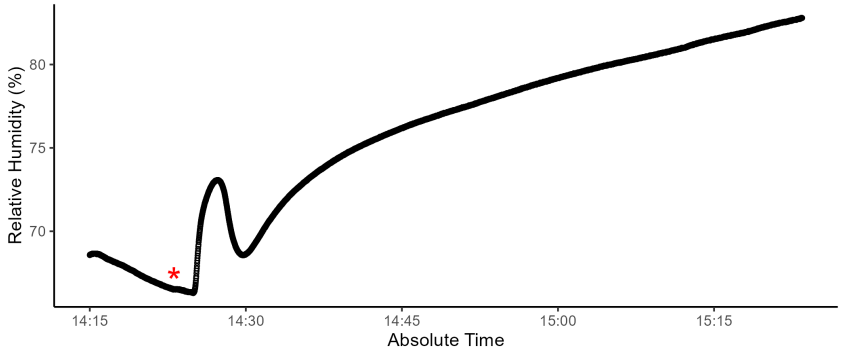

Figure 4.17: Percentage humidity within the MPS chamber cell, over the duration of the trapping on the ammonium nitrate droplet (table 4.2). The red asterisk marks the point at which the nitrogen flow into the chamber began.

As expected the relative humidity within the chamber steadily increased once the nitrogen line was inserted. The diameter measurements show an increase in size, which was the expected result of increasing the humidity; the the droplet would adsorb water from its surroundings and grow. Looking at PMT data in figures 4.16 and 4.18, however,it does not totally reflect this increase. The scattering remains relatively stable after about 15 minutes, after an initial drop, but agreement between this and the image data is inconsistent. A factor which is worthy of note is that the raw scattering data exhibits the most significant decrease in noise over time, which would seem to conflict with the continuous introduction of water vapour to the chamber. However it is possible that this flow facilitated more removal of other ammonium nitrate droplets from the laser path, by increasing their size and thus inducing more rapid condensation on to the cell walls, or at least caused them to favour gathering at the bottom of the chamber. Another observation is that the raw scattering data exhibits the same pattern of semi-regular, repeating peaks as the sodium chloride droplet. This would also indicate a steady change in droplet size.

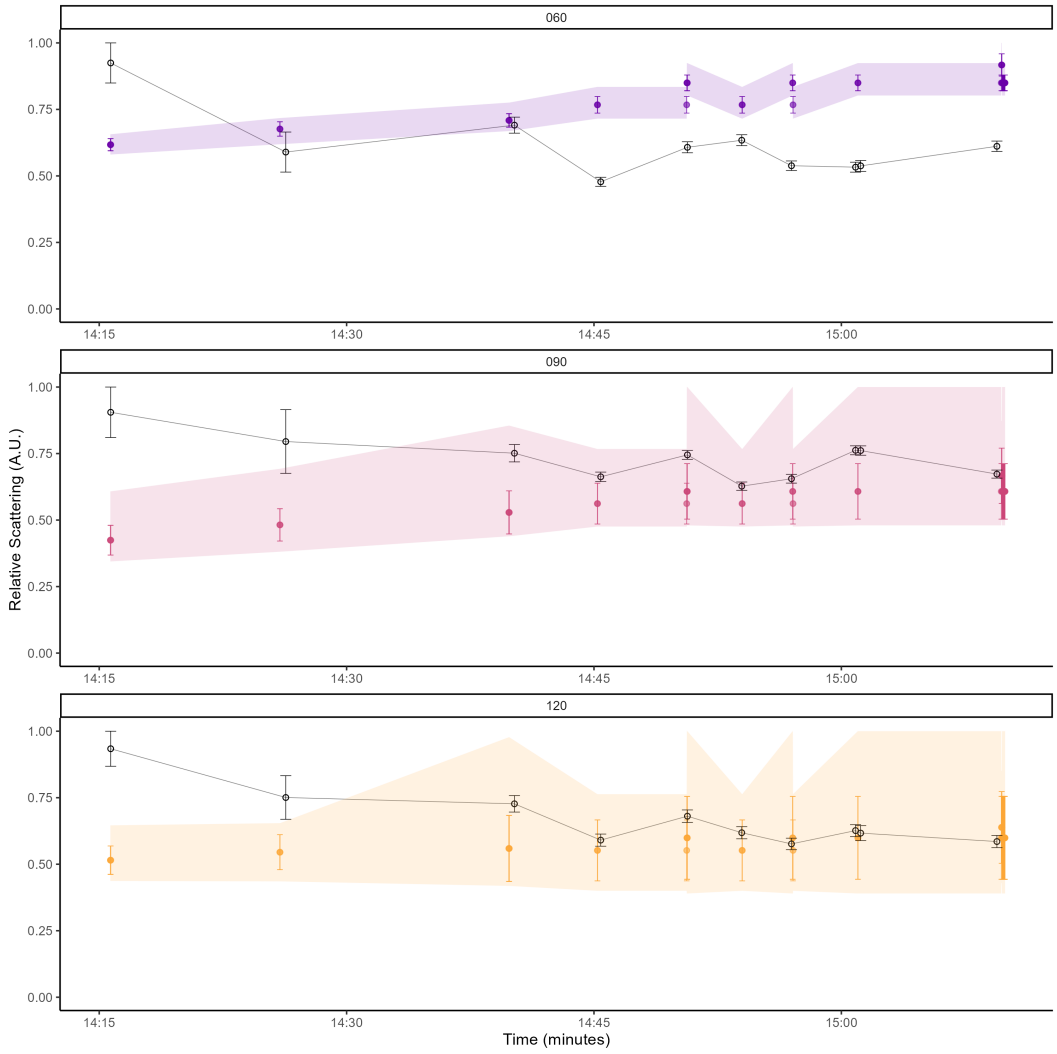

Figure 4.18: MPS scattering data (black) from the three PMTs, calculated from the raw data (figure 4.16) for each imaging window where the ammonium nitrate droplet was briefly deluminated. This data has been superimposed over the simulated scattering based on the image data (figure 4.8), the mean and full range of scattering based on that size range are shown. Scattering is presented relative to the maximum signal recorded.

4.5.2 Green laser Scattering

The relative scattering recorded by each PMT showed much more significant shifts than with the plane-aligned blue lasers, as can be seen in figure 4.19. The simulated phase function in figure 4.20 shows that the scattering intensity of particles like those analysed depends strongly on polarisation. Unfortunately, due to the need to position the MPS (17 $^{\circ}$ offset from the rest of the instrumentation), no single PMT was aligned solely parallel or perpendicular to the laser's polarisation. This complicates theoretical calculations of expected scattering to each PMT.

Another phenomenon which was observed across many of the trapping events, and best exemplified by the data shown in figure 4.19, was that of sudden changes in scattering. These were distinct from the gradual changes, or the general noise, as they were instantaneous changes in scattering that either returned to the initial scattering level, or established a new steady scattering level. The proposed cause of these digital changes is that it is due to collisions between the trapped droplet and the free floating droplets still within the cell. These collisions could result in combination of the droplets, resulting in a sudden increase in the particles diameter, or an elastic collision wherein the droplets do not combine and the droplet is ultimately unchanged. In addition to the difficulties imposed by the relative position of the laser beam and PMTs, these changes occur over a much shorter timescale than is possible to analyse by comparison with the available imaging data. However, the scattering behaviour detected by the MPS using the green laser is a strong indicator as to the potential benefits of using multiple detectors and the possibility of gaining more information about particles' optical properties.

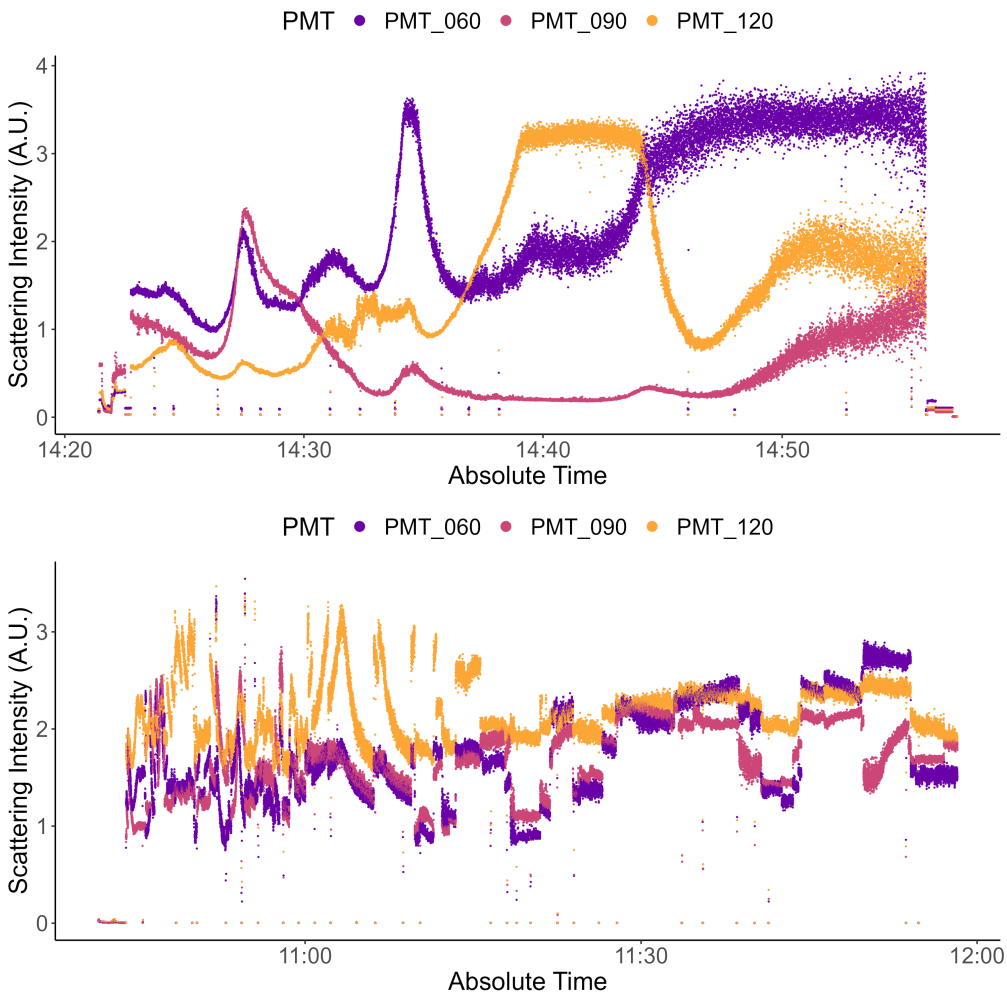

Figure 4.19: PMT intensity data recorded using the MPS, for the trapping of a sodium chloride droplet (top), and a trans-5-decene droplet (bottom). These demonstrate the large variations in scattering intensity between the PMTs.

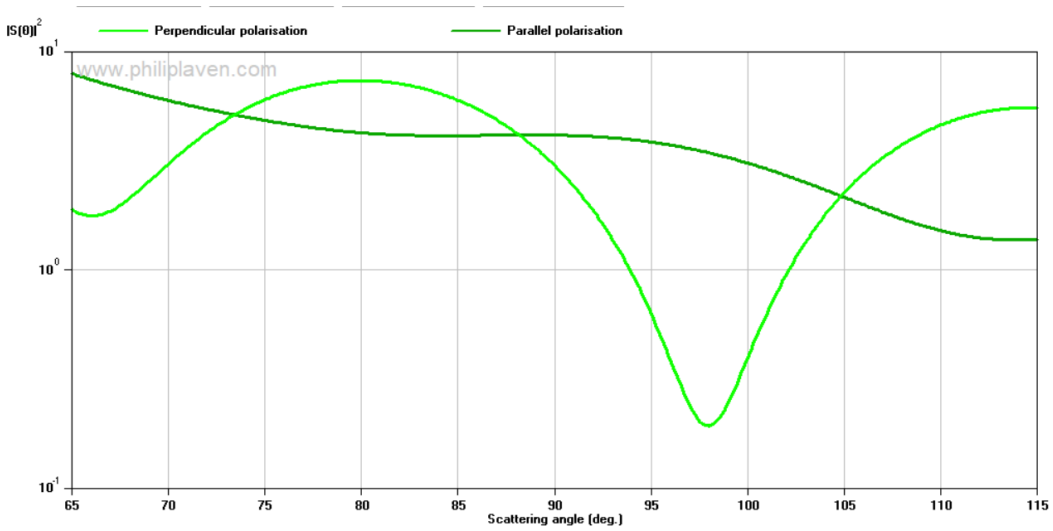

Figure 4.20: Plot created using MiePlot software, of parallel and perpendicular scattering intensity by angle of 514 nm light for a simulated 1 µm sphere with a complex refractive index of 1.33 + 0i.

4.6 Conclusions

Integration of the MPS with the optical tweezers provided the perfect opportunity for testing the limits of how the instrument could be modified to a different purpose, as well as for analysing the effect of particles' changing properties on resultant scattering. Aerosol droplets of different composition were successfully optically trapped in a novel trapping cell over long periods, under different conditions. Their properties were simultaneously analysed using the MPS' optical array and the in-built observation camera, allowing comparison and cross-verification of results. Agreement between experimental scattering data and simulation-derived theoretical data based on captured droplet images was only partial, although these comparisons were held back by low camera resolution and infrequent image collection. Scattering behaviour consistent with expected results was also observed, though not for every trapping event.

Replacing the central chamber allowed for relatively straightforward integration with the optical tweezers instrument. Minor parameter changes within the software also allowed for effective collection and processing of the resulting data. There were significant challenges in integration, since the new components were manufactured before having physical access to the optical tweezers, meaning much of the limited lab time was expended finalising calibration and procedure.

The short amount of lab time available for this experiment imposed limitations on what could be investigated. With more time, many more avenues of investigation could have been fruitfully explored. For example, trapping more particle types, trapping smaller particles and

aligning the polarisation of the green laser with the MPS' detectors.

Significant pre-planning was performed in order to maximise the potential of the limited time with the optical tweezers. Given these restrictions, the work presented here represents both a solid foundation for future investigation, as well as a validation for the usefulness of the MPS' modular design.

Chapter 5

Conclusions and Future Work

5.1 Conclusions

This project has demonstrated the potential of a multi-angle particle sizer as a viable technique to more accurately size particles and potentially extract further information on their optical properties. A prototype instrument was designed and built, and following iterative improvements, compared well with theoretical scattering patterns. The use of such an instrument for the laboratory study of single particle size changes was also demonstrated, by use of the MPS with an optical tweezers instrument.

Starting from little more than a conceptual layout, the MPS has become an instrument which can provide real-time aerosol scattering data. This includes creation of totally bespoke operational software, which is capable of supporting a range of operational modes, as well as a complex optical array and aerosol delivery system. Even with the long development stages before the data from the MPS could be meaningfully analysed, the data that has been pro-

duced by the MPS shows definitively that its novel element (multiple photodetection angles), provides significantly more particle information compared to a standard OPS instrument.

During comparison between the mean intensity of the recorded particle signals for each PMT, and the mean intensity of the simulated theoretical data, a general agreement was observed. This validates both the effectiveness of the model and the experimental data. However, large uncertainties in both datasets limit the current potential for precise estimation of particle size based purely off recorded scattering and predicted particle morphology.

Due to the form of the data produced, exploratory experimentation was performed to evaluate and present this data in a form which was informative and intuitive. A balance was found between being visually engaging and quantitatively informative, for plots of MPS data. The solutions found allow for easy evaluation of the data, as well as comparison between different datasets. These include PCA which provides a method for presenting the maximum possible proportion of the variance in a single two-dimensional scatter plot. There are further refinements which could be made to improve and streamline data presentation.

The MPS' operating software is likely the single element of the development process which underwent the most discrete iterations. The (current) final version of the software bares very little resemblance to the initial version, as virtually every element was replaced or significantly improved. From the initial goal of in-taking and recording PMT data, the scope of the software expanded to perform many new functions. These include peak detection and recording, live data display of both current data and a history of total collected data for that run, the ability to export data snapshots, histograms of peak height, and the control of mass

flow controllers. This increase in scope caused commensurate increase in complexity and processing demands, so many measures to improve efficiency and maintain performance were implemented. The software is also an element that is fit for current purposes, with no significant shortcomings. This does not preclude the possibility that other elements of the instrument and its functions would change and require a corresponding adjustment to the software, or that the software would benefit from being compiled into a discrete application, but for current functionality the software performs as required.

Overall, the structural components performed well, fulfilling their purpose in maintaining the positioning of optics and aerosol systems, as well as the structural integrity of the chamber. The chamber was also capable of maintaining a low-pressure internal environment of 200 mBar. Much like the software, the structural components would not require any adjustments in any immediate future experimentation. This would only be required if it was desired that the physical arrangement of the other components be changed to improve or modify instrument functionality. A drawback of the structural components as they currently exist is the difficultly in assembly and disassembly, which added significant time to any experimental work where any adjustment, reconfiguration or cleaning of the MPS was required. However, this is an element which would become less important further down the development pipeline.

The aerosol assembly, specifically the nozzle, was not significantly changed over the duration of the project. Part of the reason for this is that determining the performance of the nozzle directly was not possible. Instead, this was assessed indirectly through successful capturing of aerosol scattering signals. It can be inferred that since scattering signals were collected, the nozzle was effective in most cases. The poor detection of larger particles does suggest

that the nozzle may not be suitable for some particles, and it would benefit from direct verification and characterisation of the aerosol jet.

The closed and fixed-position nature of the optics did result in difficulties with diagnosing issues such as misalignment of the laser, lenses or PMTs. Construction of an open version of the optical array before beginning development may have been beneficial to verify the function of otherwise internal optics, but this would have required different equipment which was unavailable during the project. Ultimately the lenses worked well to direct scattering to the PMTs, and functioned to maintain an airtight seal.

The PMTs also functioned well, and were able to provide fast and real-time measurements. There were no issues with sensitivity, as the smallest particle class tested (200 nm diameter) was easily detected.

The lasers' small size and ease of operation was suitable for the demands of experimentation, but the 445 nm laser in particular presented issues including diminishing beam power output and an uneven beam profile. It is possible that this uneven beam profile led to the larger than expected deviation in scattering signals of the PSL particles. The wavelength stability of either laser was not determined in the course of laboratory work, which may have caused discrepancy between theoretical an experimental data. Future work on the MPS should include more rigorous evaluation of the scattering laser itself, and potentially a replacement that can be more fully and robustly integrated into the instrument.

The optical cage system improved the alignment of the beam, and convenience of tun-

ing the optics by a tremendous amount, with the drawback of increasing the overall bench footprint considerably. This is an aspect which, with further development time would be refined to reduce the MPS' size to the maximum degree practical to adhere to the design goal of making a compact instrument. The scattering simulation model was built early in the project and was able to provide information on what to expect from the experimental data. Expansion of the model to simulate a full three-dimensional environment improved the model, although data comparisons of the two- and three-dimensional simulations showed only minor discrepancies. The simulation model currently exists as an R function, able to be quickly modified to fulfil the needs of the current experiment, which was convenient during preliminary experimentation, but would likely need to be refined into a compiled form which accepted set inputs and returned data in all the required states.

The peak fitting algorithm functioned to calculate peak area for the data required, yet it was slow and cumbersome to use. It may prove prudent to streamline the process by performing these calculations all within the LabView program, to avoid unnecessary loading and post-processing of data. In most potential use cases of the MPS, the only required data will be peak properties such as maximum, width and area, so loading the full peak data into another program is redundant.

As is typical with instrument development, experimental data was not successfully produced by the MPS until well into the total project time. More time to examine more particle types would have helpful to verify its analytical capacity. In spite of this limitation, the analysis that was performed on the PSL particles built a solid foundation of evidence to support the guiding principle of the MPS and to validate its novelty. It was found that the

MPS could collect real-time aerosol scattering data over a large range of particle sizes, as well as use its multiple detection ranges to collect more detailed scattering information and relate this to particle properties. The different particle classes produced distinct scattering patterns, made more distinct once compared using data from all PMTs.

The smaller diameter PSL particles (200, 350 and 500 nm) produced scattering signals with a unimodal distribution and positive correlation between average scattering intensity and diameter, as predicted by Mie theory. The larger particles (750 and 1000 nm) continue this positive correlation, but begin to express a bimodal scattering distribution. It is unknown whether this was due to particle clumping during storage, glancing contact with the laser beam, or another factor. The 2000 and 3000 nm particle samples tested produced vastly decreased frequency of scattering signals, which did not show the expected increase in intensity with diameter. This led to the conclusion that the particles were likely either not being aerosolised successfully, or were lost in the delivery system and not passed though the chamber. The multiple detection angles made it possible to distinguish to distinct types of aerosol (350 and 500 nm PSL particles) in a mixed sample. DBSCAN provided a method for identifying clusters of signals that were likely produced by the same aerosol type, which allowed quantification of what percentage of signals belong to a given particle type within a mixture.

There is also general agreement between theoretical and experimental scattering data, although more investigation would help verify this conclusion. This indicates that the creation of lookup tables, using known particle properties of common and globally important aerosol pollutants, would allow for faster and more definitive identification of the presence of these

particles when deploying the MPS in a fieldwork setting.

The modification of the MPS central chamber, allowing integration into an existing system (The optical tweezers), demonstrates the versatility of the instrument design. This integration was successful, although more work could certainly be done to improve the integration in terms of convenience and ease-of-use. Moving components and adjusting optics was cumbersome, which was not ideal given the short time for which the optical tweezers were available. In spite of these obstacles, the MPS performed well, capturing the scattering from many droplets trapped within the custom trapping cell. Scattering data showed agreement with simulated data in many cases, and many instances of interesting scattering behaviour were observed. The behaviour of the scattering at different angles from the 514 nm laser, aligned with the trapping beams, showed extraordinary variation over time. Unfortunately the MPS and its integration with the optical tweezers was not set up with scattering from this beam in mind, so simulation of the instrument data under equivalent circumstances, and thus full analysis of this data, was not possible during the project. In spite of this, the integration showed great promise and produced interesting data and observations.

5.2 Future Work

The primary considerations when planning future work would be to expand the range of particle types analysed, and to make the MPS ready for potential fieldwork. Determining the resolution of the MPS by testing smaller PSL particles, and PSL particles which are closer in diameter to each other, would be a useful metric in assessing performance. It would also be beneficial to obtain (either through purchasing these particles or via filtration) a particle sample with a more uniform distribution of individual diameters, to see

if this diminishes the spread of scattering signals observed during previous instrument testing.

Particle types other than PSL beads should also be tested, with spherical particles with known CRI being a priority, as the agreement between simulated and actual scattering needs to be more thoroughly verified before testing unknown samples. Non-spherical particles would also be prominent candidates for future analysis, as this would allow use of the other scattering theories discussed in chapter 1.

Further testing of the current 445 and 405 nm lasers, as well as experimenting with another laser would help to test the MPS' functionality and associated simulations; to observe the effect of wavelength on scattering under otherwise identical circumstances. The wavelength stability of the lasers was not verified, which could be responsible for some the high variation of scattering signals. This could be done directly using a spectrometer, or could be attempted by determining if there is a drift in the spread of particle scattering signals over a period of time. It may also be beneficial to modify the laser control software to record the laser temperature and current over time, and potentially link this to deviations observed via the previously-mentioned methods.

Another component which functions but would benefit from testing, would be the aerosol nozzle, specifically the effect of the sheath flow on the spread of the aerosol jet over the first two centimetres of travel beyond the nozzle tip. This could be achieved via use of an aerosolised tracer particle directed though the nozzle, which could be illuminated and the spread of particles captured using a camera. By repeating this with varying flow rate, particle size and optional sheath flow, the effectiveness of the nozzle and optimal operating

parameters could be determined. This would require additional equipment, but was shown to be effective when a similar technique was used in the original report of the nozzle design.[68]

The manually tunable gains on each PMT were effective for varying the signal intensity during laboratory work, but would likely need improvements when bringing the instrument to a truly finished state. A method of quantitatively measuring and recording the applied gain, and a way to set and lock each gain would make it easier and more streamlined to perform measurements and correct for gain during later data analysis.

Further experimentation would also provide an opportunity to re-examine the arrangement of components and the scattering collection angles. In addition to potentially gaining more information from particles by collecting at an even lower angle, it would also be possible to alter the angle ranges themselves (with a commensurate change to the scattering simulations), in an attempt to isolate and examine a smaller portion of the scattered light. Having all three scattering ranges be the same was beneficial for streamlining the design and simulation processes, but using varied collection angles in a motivated way may illuminate more scattering information. Unequal collection ranges have been shown to work in the development of another instrument (the Light Optical Aerosol Counter (LOAC)), as discussed in chapter 1.[62]

For improved analysis of mixed sample data collection, an automated computational method for identifying and sorting individual signals by likely source would help with improving the MPS' capabilities. It would also act as a useful development tool for comparison between the ratio of particle types intended to be nebulised, and their presence within the set of observed particles, to evaluate the effectiveness of nebulisation and delivery for different particle types.

Integration with the CLF optical tweezers was not originally part of the initial project outline, but became a key component of the project, providing important insights into the potential of the MPS as a versatile instrument, as well as helping to improve software and hardware for MPS in general. During any future work, opportunities to integrate the MPS with other instruments and modify its function should be pursued whenever possible.

Bibliography

[1] M. Shiraiwa, K. Selzle, and U. P. Hazardous components and health effects of atmospheric aerosol particles: reactive oxygen species, soot, polycyclic aromatic compounds and allergenic proteins. *Free Radical Research*, 46(8):927–939, 2012.

[2] J. H. Seinfeld and S. N. Pandis. *Atmospheric Chemistry and Physics: From Air Pollution to Climate Change*. Wiley, 2016.

[3] V. F. McNeill. Atmospheric aerosols: Clouds, chemistry, and climate. *Annual Review of Chemical and Biomolecular Engineering*, 8(1):427–444, 2017.

[4] J. Nirmalkar, D. K. Deshmukh, M. K. Deb, S. Chandrawanshi, and S. Tiwari. Seasonal size distribution and possible health implications of atmospheric aerosols collected from a rural site of eastern central india. *Atmospheric Pollution Research*, 7(2):278–287, 2016.

[5] S. Zhang, J. Wu, W. Fan, Q. Yang, and D. Zhao. Review of aerosol optical depth retrieval using visibility data. *Earth-Science Reviews*, 200:102986, 2020.

[6] P. H. McMurry. A review of atmospheric aerosol measurements. *Atmospheric Environment*, 34(12):1959–1999, 2000.

[7] C. Bohren and D. Huffman. *A Miscellany of Applications*, chapter 14, pages 429–474. John Wiley and Sons, Ltd, 1998.

[8] T. Grigoratos and G. Martini. Brake wear particle emissions: a review. *Environ. Sci. Pollut. Res. 2014 224*, 22(4):2491–2504, 2014.

[9] U. P. Atmospheric aerosols: Composition, transformation, climate and health effects. *Angewandte Chemie International Edition*, 44(46):7520–7540, 2005.

[10] T. V. Vu, S. Zauli-Sajani, V. Poluzzi, and R. M. Harrison. Factors controlling the lung dose of road traffic-generated sub-micrometre aerosols from outdoor to indoor environments. *Air Qual. Atmos. Heal.*, 11(6):615–625, 2018.

[11] C. M. Sorensen. Q-space analysis of scattering by particles: A review. *Journal of Quantitative Spectroscopy and Radiative Transfer*, 131:3–12, 2013. Concepts in electromagnetic scattering for particulate-systems characterization.

[12] S. E. Bauer, D. Koch, N. Unger, S. M. Metzger, D. T. Shindell, and D. G. Streets. Nitrate aerosols today and in 2030: a global simulation including aerosols and tropospheric ozone. *Atmospheric Chemistry and Physics*, 7(19):5043–5059, 2007.

[13] J. Yin, R. Harrison, Q. Chen, A. Rutter, and J. Schauer. Source apportionment of fine particles at urban background and rural sites in the uk atmosphere. *Atmospheric Environment*, 44(6):841–851, February 2010.

[14] V. F. McNeill. Atmospheric aerosols: Clouds, chemistry, and climate. *Annual Review of Chemical and Biomolecular Engineering*, 8(1):427–444, 2017. PMID: 28415861.

[15] T. Arfin, A. M. Pillai, N. Mathew, A. Tirpude, R. Bang, and P. Mondal. An overview of atmospheric aerosol and their effects on human health. *Environ. Sci. Pollut. Res.*, 30(60):125347–125369, 2023.

[16] A. Laskin, J. Laskin, and S. A. Nizkorodov. Chemistry of atmospheric brown carbon. *Chemical Reviews*, 115(10):4335–4382, 2015. PMID: 25716026.

[17] P. Saxena and S. Sonwani. *Criteria Air Pollutants and their Impact on Environmental Health*. Springer, 01 2019.

[18] A. Piscitello, C. Bianco, A. Casasso, and R. Sethi. Non-exhaust traffic emissions: Sources, characterization, and mitigation measures. *Science of The Total Environment*, 766:144440, 2021.

[19] F. Amato, F. R. Cassee, H. A. C. D. van der Gon, R. Gehrig, M. Gustafsson, W. Hafner, R. M. Harrison, M. Jozwicka, F. J. Kelly, T. Moreno, A. S. H. Prevot, M. Schaap, J. Sunyer, and X. Querol. Urban air quality: The challenge of traffic non-exhaust emissions. *Journal of Hazardous Materials*, 275:31–36, 2014.

[20] F. dos Santos, W. Andreao, G. Miranda, A. de Carvalho, J. Pinto, R. Pedruzzi, V. Carvalho, and T. de Almeida Albuquerque. Vehicular air pollutant emissions in a developing economy with the widespread use of biofuels. *Urban Climate*, 38, 2021.

[21] M. Ketzel, G. Omstedt, C. Johnasson, I. During, M. Pohjola, D. Oettl, L. Gidhagen, P. Wahin, A. Lohmeyer, M. Haakana, and R. Berkowicz. Estimation and validation of pm2.5/pm10 exhaust and non-exhaust emission factors for practical street pollution modelling. *Atmospheric Environment*, 41(40):9370–9385, 2007.

[22] G. Kim and S. Lee. Characteristics of tire wear particles generated by a tire simulator under various driving conditions. *Environmental Science & Technology*, 52(21):12153–12161, 2018.

[23] J. Kwak, H. Kim, J. Lee, and S. Lee. Characterization of non-exhaust coarse and fine particles from on-road driving and laboratory measurements. *Science of The Total Environment*, 458-460:273–282, 2013.

[24] J. Kukutschová, P. Moravec, V. Tomášek, V. Matějka, J. Smolík, J. Schwarz, J. Seidlerová, K. Šafářová, and P. Filip. On airborne nano/micro-sized wear particles released from low-metallic automotive brakes. *Environmental Pollution*, 159(4):998–1006, 2011.

[25] NoAA. State of the science fact sheet august 2022. `https://https://sciencecouncil.noaa.gov/council-products/science-facts-sheets/`, 2022. Accessed: 12/01/24.

[26] F. Gozzi, G. Della Ventura, and A. Marcelli. Mobile monitoring of particulate matter: State of art and perspectives. *Atmospheric Pollution Research*, 7(2):228–234, 2016.

[27] E. J. Abba, S. Unnikrishnan, R. Kumar, B. Yeole, and Z. Chowdhury. Fine aerosol and pah carcinogenicity estimation in outdoor environment of mumbai city, india. *International Journal of Environmental Health Research*, 22(2):134–149, 2012.

[28] W. J. Gauderman, E. Avol, F. Gilliland, H. Vora, D. Thomas, K. Berhane, R. McConnell, N. Kuenzli, F. Lurmann, E. Rappaport, H. Margolis, D. Bates, and J. Peters. The effect of air pollution on lung development from 10 to 18 years of age. *New England Journal of Medicine*, 351(11):1057–1067, 2004.

[29] M. Brauer, G. Freedman, J. Frostad, A. van Donkelaar, R. V. Martin, F. Dentener, R. v. Dingenen, K. Estep, H. Amini, J. S. Apte, K. Balakrishnan, L. Barregard, D. Broday, V. Feigin, S. Ghosh, P. K. Hopke, L. D. Knibbs, Y. Kokubo, Y. Liu, S. Ma, L. Morawska, J. L. T. Sangrador, G. Shaddick, H. R. Anderson, T. Vos, M. H. Forouzanfar, R. T. Burnett, and A. Cohen. Ambient air pollution exposure estimation for the global burden of disease 2013. *Environmental Science & Technology*, 50(1):79–88, 2016. PMID: 26595236.

[30] J. Lelieveld, A. Haines, R. Burnett, C. Tonne, K. Klingmüller, T. Münzel, and A. Pozzer. Air pollution deaths attributable to fossil fuels: observational and modelling study. *BMJ*, 383, 2023.

[31] WHO. Who global air quality guidelines: particulate matter (pm2.5 and pm10), ozone, nitrogen dioxide, sulfur dioxide and carbon monoxide. `https://www.who.int/publications/i/item/9789240034228`, 2021. Accessed: 12/01/24.

[32] B. Cohen and A. Bronzaft. Air transportation and human health. In J. Nriagu, editor, *Encyclopedia of Environmental Health*, pages 53–63. Elsevier, Burlington, 2011.

[33] Z. Samaras and I. Vouitsis. 3.13 - transportation and energy. In R. A. Pielke, editor, *Climate Vulnerability*, pages 183–205. Academic Press, Oxford, 2013.

[34] G. Pizzino, N. Irrera, M. Cucinotta, G. Pallio, F. Mannino, V. Arcoraci, F. Squadrito, D. Altavilla, and A. Bitto. Oxidative Stress: Harms and Benefits for Human Health. *Oxid. Med. Cell. Longev.*, 2017:8416763, 2017.

[35] S. S. Amaral, J. A. De Carvalho, M. A. M. Costa, and C. P. An overview of particulate matter measurement instruments. *Atmosphere*, 6(9):1327–1345, 2015.

[36] M. Mazurenka, A. J. Orr-Ewing, R. Peverall, and G. A. D. Ritchie. 4 cavity ring-down and cavity enhanced spectroscopy using diode lasers. *Annu. Rep. Prog. Chem., Sect. C: Phys. Chem.*, 101:100–142, 2005.

[37] J. M. Langridge, M. S. Richardson, D. Lack, D. Law, and D. M. Murphy. Aircraft instrument for comprehensive characterization of aerosol optical properties, part i: Wavelength-dependent optical extinction and its relative humidity dependence measured using cavity ringdown spectroscopy. *Aerosol Science and Technology*, 45(11):1305–1318, 2011.

[38] D. A. Lack, M. S. Richardson, D. Law, J. M. Langridge, C. D. Cappa, R. J. McLaughlin, and D. M. Murphy. Aircraft instrument for comprehensive characterization of aerosol optical properties, part 2: Black and brown carbon absorption and absorption enhancement measured with photo acoustic spectroscopy. *Aerosol Science and Technology*, 46(5):555–568, 2012.

[39] F. Mei, G. McMeeking, M. Pekour, R. Gao, G. Kulkarni, S. China, H. Telg, D. Dexheimer, J. Tomlinson, and B. Schmid. Performance assessment of portable optical particle spectrometer (pops). *Sensors*, 20(21), 2020.

[40] F. Mei and M. Pekour. *Portable Optical Particle Spectrometer (POPS) Instrument Handbook*. Handix Scientific Inc., 2020.

[41] A. Kupc, C. Williamson, N. L. Wagner, M. Richardson, and C. A. Brock. Modification, calibration, and performance of the ultra-high sensitivity aerosol spectrometer for particle size distribution and volatility measurements during the atmospheric tomography mission (atom) airborne campaign. *Atmospheric Measurement Techniques*, 11(1):369–383, 2018.

[42] Y. Cai, D. C. Montague, W. Mooiweer-Bryan, and T. Deshler. Performance characteristics of the ultra high sensitivity aerosol spectrometer for particles between 55 and 800nm: Laboratory and field studies. *Journal of Aerosol Science*, 39(9):759–769, 2008.

[43] A. Nagy, W. Szymanski, P. Gal, A. Golczewski, and A. Czitrovszky. Numerical and experimental study of the performance of the dual wavelength optical particle spectrometer (dwops). *Journal of Aerosol Science*, 38(4):467–478, 2007.

[44] E. Asher, T. Thornberry, D. W. Fahey, A. McComiskey, K. Carslaw, S. Grunau, K.-L. Chang, H. Telg, P. Chen, and R.-S. Gao. A novel network-based approach to determining measurement representation error for model evaluation of aerosol microphysical properties. *Journal of Geophysical Research: Atmospheres*, 127(3):e2021JD035485, 2022. e2021JD035485 2021JD035485.

[45] C. Bohren and D. Huffman. *Appendix B: Coated Sphere*, pages 483–489. John Wiley and Sons, Ltd, 1998.

[46] NASA. Firex-aq – fire influence on regional to global environments and air quality. https://www-air.larc.nasa.gov/missions/firex-aq/, 2021. Accessed: 18/08/2021.

[47] NoAA. Firex-aq investigating smoke from wildfires and biomass burning. https://csl.noaa.gov/projects/firex-aq/, 2021. Accessed: 18/08/2021.

[48] NASA. Dc-8 - afrc. https://espo.nasa.gov/firex-aq/aircraft/DC-8_-_AFRC, 2021. Accessed: 18/08/2021.

[49] NASA. In-situ measurements of aerosol optical properties (aop). https://espo.nasa.gov/firex-aq/instrument/AOP, 2019. Accessed: 18/08/2021.

[50] DMT. *Manual, Ultra High Sensitivity Aerosol Spectrometer (UHSAS)*. Droplet Measurement Technologies, Longmont, Colorado, 2017.

[51] A. Abo Riziq, C. Erlick, E. Dinar, and Y. Rudich. Optical properties of absorbing and non-absorbing aerosols retrieved by cavity ring down (crd) spectroscopy. *Atmospheric Chemistry and Physics*, 7(6):1523–1536, 2007.

[52] NASA. Airborne science data for atmospheric composition: Firex-aq 2019. https://www-air.larc.nasa.gov/cgi-bin/ArcView/firexaq, 2019. Accessed: 18/08/2021.

[53] H. Marsh and F. Rodríguez-Reinoso. Chapter 2 - activated carbon (origins). In H. Marsh and F. Rodríguez-Reinoso, editors, *Activated Carbon*, pages 13–86. Elsevier Science Ltd, Oxford, 2006.

[54] W. Somerville, B. Auguie, and E. L. Ru. Smarties: User-friendly codes for fast and accurate calculations of light scattering by spheroids. *Journal of Quantitative Spectroscopy and Radiative Transfer*, 174:39–55, 2016.

[55] F. Liu, C. Wong, D. R. Snelling, and G. J. Smallwood. Investigation of absorption and scattering properties of soot aggregates of different fractal dimension at 532 nm using rdg and gmm. *Aerosol Science and Technology*, 47(12):1393–1405, 2013.

[56] P. Gwaze, O. Schmid, H. J. Annegarn, M. O. Andreae, J. Huth, and G. Helas. Comparison of three methods of fractal analysis applied to soot aggregates from wood combustion. *Journal of Aerosol Science*, 37(7):820–838, 2006.

[57] A. Filippov, M. Zurita, and D. Rosner. Fractal-like aggregates: Relation between morphology and physical properties. *Journal of Colloid and Interface Science*, 229(1):261–273, 2000.

[58] A. Brasil, T. Farias, and M. Carvalho. A recipe for image characterization of fractal-like aggregates. *Journal of Aerosol Science*, 30(10):1379–1389, 1999.

[59] H. Volten, O. Muñoz, E. Rol, J. F. de Haan, W. Vassen, J. W. Hovenier, K. Muinonen, and T. Nousiainen. Scattering matrices of mineral aerosol particles at 441.6 nm and 632.8 nm. *Journal of Geophysical Research: Atmospheres*, 106(D15):17375–17401, 2001.

[60] J. W. Hovenier, H. Volten, O. Muñoz, W. J. van der Zande, and L. B. F. M. Waters. Laboratory studies of scattering matrices for randomly oriented particles: potentials, problems, and perspectives. *Journal of Quantitative Spectroscopy and Radiative Transfer*, 79-80:741–755, 2003.

[61] T. Eidhammer, D. C. Montague, and T. Deshler. Determination of index of refraction and size of supermicrometer particles from light scattering measurements at two angles. *Journal of Geophysical Research: Atmospheres*, 113(D16), 2008.

[62] J.-B. Renard, F. Dulac, G. Berthet, T. Lurton, D. Vignelles, F. Jégou, T. Tonnelier, M. Jeannot, B. Couté, R. Akiki, N. Verdier, M. Mallet, F. Gensdarmes, P. Charpentier, S. Mesmin, V. Duverger, J.-C. Dupont, T. Elias, V. Crenn, J. Sciare, P. Zieger, M. Salter, T. Roberts, J. Giacomoni, M. Gobbi, E. Hamonou, H. Olafsson, P. Dagsson-Waldhauserova, C. Camy-Peyret, C. Mazel, T. Décamps, M. Piringer, J. Surcin, and D. Daugeron. Loac: a small aerosol optical counter/sizer for ground-based and balloon measurements of the size distribution and nature of atmospheric particles – part 1: Principle of measurements and instrument evaluation. *Atmospheric Measurement Techniques*, 9(4):1721–1742, 2016.

[63] D. Li, F. Chen, N. Zeng, Z. Qiu, H. He, Y. He, and H. Ma. Study on polarization scattering applied in aerosol recognition in the air. *Opt. Express*, 27(12):A581–A595, Jun 2019.

[64] P. Kheirkhah, A. Baldelli, P. Kirchen, and S. Rogak. Development and validation of a multi-angle light scattering method for fast engine soot mass and size measurements. *Aerosol Science and Technology*, 54(9):1083–1101, sep 2020.

[65] W. Shao, H. Zhang, and H. Zhou. Fine particle sensor based on multi-angle light scattering and data fusion. *Sensors*, 17(5), 2017.

[66] M. Nakagawa, T. Nakayama, H. Sasago, S. Ueda, D. S. Venables, and Y. Matsumi. Design and characterization of a novel single-particle polar nephelometer. *Aerosol Science and Technology*, 50(4):392–404, apr 2016.

[67] P. Kheirkhah, P. Kirchen, and S. Rogak. Fast exhaust nephelometer (fen): A new instrument for measuring cycle-resolved engine particulate emission. Technical Report 2016-01-2329, SAE International, 2016.

[68] Y. Pan, J. Bowersett, S. C. Hill, R. G. Pinnick, and R. K. Chang. Nozzles for focusing aerosol particles. Technical report, ARMY RESEARCH LAB ADELPHI MD COMPUTATIONAL AND INFORMATION SCIENCES DIRECTORATE, 2009.

[69] M. Roesch, C. Roesch, and D. J. Cziczo. Dry particle generation with a 3-d printed fluidized bed generator. *Atmospheric Measurement Techniques*, 10(6):1999–2007, 2017.

[70] DMT. Dmt quartz dust up to 5 my. `https://www.web-shop-hosting.net/test-dust/dmt-quartz-dust-up-to-5-my`, 2022. Accessed: 09/02/2022.

[71] E. Components. Iron oxide test dust. `https://www.ellis-components.co.uk/test-dust-contaminants/`, 2022. Accessed: 09/02/2022.

[72] S. P. Lee, W. Tscharnuter, and B. Chu. Calibration of an optical self-beating spectrometer by polystyrene latex spheres and confirmation of the stokes-einstein formula. *Journal of Polymer Science: Polymer Physics Edition*, 10(12):2453–2459, 1972.

[73] N. Y. John E. Brockmann and D. Lucero. Calibration of the aerodynamic particle sizer 3310 (aps-3310) with polystyrene latex monodisperse spheres and oleic acid monodisperse particles. *Aerosol Science and Technology*, 8(3):279–281, 1988.

[74] M. Heim, B. J. Mullins, H. Umhauer, and G. Kasper. Performance evaluation of three optical particle counters with an efficient "multimodal" calibration method. *Journal of Aerosol Science*, 39(12):1019–1031, 2008.

[75] C. Kidd, V. Perraud, and B. J. Finlayson-Pitts. Surfactant-free latex spheres for size calibration of mobility particle sizers in atmospheric aerosol applications. *Atmospheric Environment*, 82:56–59, 2014.

[76] T. Könemann, N. J. Savage, J. A. Huffman, and C. Pöhlker. Characterization of steady-state fluorescence properties of polystyrene latex spheres using off- and online spectroscopic methods. *Atmospheric Measurement Techniques*, 11(7):3987–4003, 2018.

[77] D. V. Averkin. Synthesis of Particle Size Standards Based on Aqueous Suspensions of Polystyrene Latex Spheres. *Meas. Tech.*, 65(12):936–941, 2023.

[78] T. Njalsson and I. Novosselov. Design and optimization of a compact low-cost optical particle sizer. *Journal of Aerosol Science*, 119:1–12, 2018.

[79] J. van Mameren, G. J. L. Wuite, and I. Heller. Introduction to optical tweezers: Background, system designs, and commercial solutions. In *Methods in molecular biology (Clifton, N.J.)*, volume 783 of *Methods in Molecular Biology*, pages 1–20. Humana Press, Totowa, NJ, 2011.

[80] S. H. Jones, M. D. King, and A. D. Ward. Determining the unique refractive index properties of solid polystyrene aerosol using broadband mie scattering from optically trapped beads. *Phys. Chem. Chem. Phys.*, 15:20735–20741, 2013.

[81] M. R. McGrory, M. D. King, and A. D. Ward. Using mie scattering to determine the wavelength-dependent refractive index of polystyrene beads with changing temperature. *The Journal of Physical Chemistry A*, 124(46):9617–9625, 2020. PMID: 33164512.

[82] L. Xu, L. Luo, H. Wu, Z. Luo, T. Chang, P. Wu, C. Du, and H. Cui. Ultrasensitive Optical Refractive Index Detection of NaCl and Alcohol Solutions Based on Weak Value Amplification. *Plasmonics*, 15(3):671–678, 2020.

[83] K. Lal, N. Tripathi, and G. P. Dubey. Densities, viscosities, and refractive indices of binary liquid mixtures of hexane, decane, hexadecane, and squalane with benzene at 298.15 k. *Journal of Chemical & Engineering Data*, 45(5):961–964, 2000.

[84] Fisher Scientific. trans-5-decene, 97%, thermo scientific chemicals. https://www.fishersci.com/shop/products/trans-5-decene-97-thermo-scientific/AAL1068903, 2023. Accessed: 14/04/2023.

[85] M. Jarzembski, M. Norman, K. Fuller, V. Srivastava, and D. Cutten. Complex refractive index of ammonium nitrate in the 2-20-micrometer spectral range. *Applied optics*, 42:922–30, 03 2003.